IMPROVING MECHANICAL PROPERTIES OF ORDINARY PORTLAND CEMENT PASTES UTILISING CARBON NANOTUBES: FABRICATION, CHARACTERIZATION AND MODELLING

BY

SHU-JIAN CHEN

A Thesis

Submitted in Fulfilment of the Requirements for the

Degree of Doctor of Philosophy

Department of Civil Engineering,

Monash University,

Melbourne, Australia

February, 2015

_____

Shu-Jian Chen

August 2015

ABSTRACT

Carbon nanotubes (CNTs) are the strongest fibres that have been made, and have been used as reinforcing additives in ordinary Portland cement (OPC) since 2005. One major aim of incorporating CNTs in OPC paste has been to improve the mechanical properties of cement, thereby reducing the consumption of cement in construction and limiting its environmental impact. However, the reported reinforcing effect of CNTs has so far shown large discrepancies due to the limited understanding of the dispersion of CNTs and reinforcing mechanism in OPC paste.

This PhD study aims to improve theoretical understanding of the composite and to develop applicable fabrication methods that can produce stable and significant increases in the mechanical properties of CNT-OPC paste. To achieve this aim, three main tasks are defined as: (1) investigating the dispersion and agglomeration of CNTs in water and alkaline environment; (2) studying the reinforcing mechanism of CNTs; (3) optimizing the fabrication of CNT-OPC paste composite.

Experimental, theoretical and numerical approaches are adopted to accomplish these tasks. Experimental techniques such as the use of scanning electron, transmission electron and optical microscopy, UV-vis spectrometry, centrifugation and compressive, flexural and fractural tests are employed to investigate the dispersion and reinforcing effects of CNTs as well as to optimize the fabrication protocol. In the theoretical part of this study, molecular mechanics/dynamics (MM/MD) simulation and theoretical development are conducted to develop models to study CNT dispersion and predict the reinforcing effect of CNTs.

Regarding task (1), MM simulation suggests that variation in the molecular characteristics of surfactants generates different interaction energies with the CNT surface, thereby altering their packing morphologies on the CNT surface. Surfactants with long chain-like and planar like structures interact more effectively with CNTs compared with short and linear molecules. Surfactant-dispersed CNTs are found to be in a semi-stable state in a calcium based alkaline environment. A theoretical model is developed to simulate the agglomeration of the CNTs in such an environment. This model suggests that CNTs prefer first to form parallel bundles with a few tubes, before growth into large 3D agglomerates occurs.

In terms of task (2), the reinforcing mechanism of CNTs is investigated by developing a micro-mechanical crack bridging model. This model is based on length distribution of the CNTs, which is found to follow a log-normal distribution. The length distribution of the CNTs is heavily affected by the ultrasonication process used in the fabrication of the CNT-OPC paste which promotes the dispersion of CNTs while scissoring them into shorter ones. This crack bridging model is used to predict the optimum ultrasonication energy for reinforcing purposes.

In task (3), the prediction is further verified by mechanical testing results, where the optimum ultrasonication energy, 75 J/ml, observed in the tests matches the prediction of the model. By using this optimal energy, the increment in fracture energy and flexural strength (notched beam) is doubled compared with low (25J/ml) or very high (400J/ml) ultrasonication energy. The mechanical test results also show that the reinforcing effect is almost proportional to the concentration of the dispersed CNTs, which again matches the model's assumption. Further experimental investigation of the maximum concentration of dispersed CNTs suggests a limit of 0.264 wt % (in water with cement-compatible surfactants), above which significant

agglomeration will occur. After incorporation into fresh OPC paste, ~60 wt % of the CNTs stays dispersed for 4-16 hours and ~35 % is adsorbed by cement grains within 5 minutes.

This PhD thesis enhances understanding of CNT-OPC paste and addresses some future research direction of nanoscale particle reinforced cementitious materials.

ABBREVIATIONS

716LR	Rheobuild®716LR
a	spacing of bars
A	ABS at a specific wavelength
a_0	initial notch depth
ABS	light absorbance
AG	Arabic gum
A_o	total area under load-deflection curve
ARC	Australian Research Council
b	width of beam
C	mass of CNTs
c	mass of dry cement powder
c/w	cement to water ratio
C3S	tricalcium silicate
C_d	dispersed CNT concentration
CMOD	crack mouth opening displacement
C_N	normalised concentration of dispersed CNTs
CNF	carbon nanofibres
CNT(s)	carbon nanotube(s) A
COMPASS	Condensed-phased Optimized Molecular Potential for Atomistic Simulation Studies
C-S-H	calcium silicate hydrate
CTAB	cetyltrimethyl ammonium bromide
d	Kolmogorov-Smirnov statistic
d'	depth of beam

d''	dimension of OPC grains
DBSA	dodecyl-benzene sulfonic acid
d_f	diameter of fibre
e	natural constant
E	Young's modulus,
EDX	energy-dispersive X-ray
E_f	Young's modulus of fibre
F	an empirical constant taking into account the shape of particles
g	a constant factor describing snubbing effect due to inclined fibres
G_F	fracture energy
HD	average hydrodynamic size
I	mechanical improvement factor
I'_t	angle dependent variants of I_t
I_s	interaction energy between an individually dispersed CNT and surrounding surfactants and solution
ISO	International Organization Standardization
I_t	interaction energy between two CNTs
k	a coefficient describing how many pairs of tube-tube interaction are introduced at bar-bar intersecting point
K	index of a tube in a shell layer
$\overline{L_t}$	expectation of CNT length
L	length of tube
l	path length of light through CNT suspension.
L_f	length of fibre

L_t	tube length
M	index of the layer of shell in a CNT bundle
MA	Micro Air® 905
MD	molecular dynamics
mg	self-weight of beam
MM	molecular mechanics
M_t	mass of a single CNT
MWCNT(s)	multi-walled CNT(s)
n	number of intersecting bars
N	number of tubes in a parallel bundle
N'	sample size
NaDC	sodium deoxycholate
NaDDBS	sodium dodecyl-benzene sulfonate
NC	naphthalene-sulfonic acid/formaldehyde calcium salt
NVT	canonical ensemble
OPC	ordinary Portland cement
p	mass of PC
$p(L_t)$	distribution of probability of occurrence
PC	polycarboxylate-based cement superplasticizer
PDF	probability distribution function
PVA	polyvinyl alcohol fibre
R	mass fraction of the grains with diameter greater than *d''*
RI	reinforcing index
RI_G	fracture energy G_F

RI_σ	reinforcing indices for flexural strength σ_f
RVE	representative volume element
s	mass of suspensions
S	sum of self-energy of all the tubes in a parallel bundle
S'	surface area of particles with diameter equal to d'',
SBBS	butyl-benzene sulfonate
ΔS	change in S
SEM	scanning electron microscopy
SL	modified sodium lignosulfonate
SOBS	sodium octyl-benzene sulfonate
$S_t(x)$	average self-energy due to tangling
SWCNT(s)	single-walled CNT(s)
TEM	Transmission electron microscopy
TGA	thermogravimetry analysis
TX100	triton X-100, an ethoxylated alkyl
UE	utrasonication energy
$\overline{UE}$	normalized UE
V	volume of suspensions
$v(L_t)$	proportion of CNT volume with a specific length L_t within the total volume of dispersed CNTs
vdW	van der Waals
V_f	fibre volume content in matrix
V_t	CNTs to matrix volume ratio

$V_{t\max}$	maximum volume of dispersed CNTs obtained after dispersion plateau is reached
w	mass of distilled water
w/c	water to cement ratio
W_c	weight of added OPC grains
W_f / W_m	weight percentage of fibres in matrix
WRDA	WRDA® GWA
x	number of CNTs in an agglomerate
δ	crack opening
δ_0	deflection at final failure of beam
ε	specific extinction coefficient
θ	intersecting angle between bars
μ and σ	mean and standard deviation of the natural logarithm
μ_N	average self-energy of individual tubes in a parallel bundle
μ_x	average self-energy for each CNT in a CNT agglomerate containing x tubes
ρ	specific gravity of OPC grains
ρ_f	density of fibres
ρ_m	density of matrix material
σ_B	crack bridging stress
σ_f	flexural strength
τ	frictional bond strength

DECLARATION

This thesis describes my research carried out in the Department of Civil Engineering at Monash University in Australia during the candidature period from March 2011 to February 2015. The thesis is submitted to Monash University in total fulfilment of the requirements for the degree of Doctor of Philosophy.

The thesis contains no material which has been accepted for the award of any other degree or diploma in any university or institution and no material which has been previously written or published by another person except where due reference is made in the text of the thesis.

_____

Shu-Jian Chen

August 2015

ACKNOWLEGEMENTS

The sequence of acknowledgements is not based on importance of acknowledgees.

First of all, I have to thank God for giving me this opportunity to complete both my undergraduate and PhD study in Monash University. I have this excellent chance to join a 2+2 program in 2006 back in Central South University, China, which allows me to study overseas in Australia. I worked very hard during my undergraduate study, especially in the last two semesters when I only slept 4 to 5 hours everyday. In return, I have earned the legibility to continue my study has a postgraduate student with a fantastic, cutting edge research topic that I am really interested in. Working on such topics means very limit past works to learn from so I work extra to establish laboratory setup and experiment protocols all from scratch. There are times when things are not going as expected and I felt depressed. However, I am grateful that God put me through all this, from which I learn to not be defeated by difficulties but to conquer and resolve them. I also need to thank him for keeping me healthy and energetic so I can march the course of this 4-year research.

My parents will be the next to say thanks. Without their support, I would not be able to afford the tuition and living allowance for my undergraduate studies. But more importantly, their love makes me feel safe even when I am far away from home. I also need to thank my girlfriend, Sarah, for accompanying and caring about me when I am writing this thesis.

Further, I must acknowledge Australian Government through Monash University for providing me the Australian postgraduate award (APA) which covers my living allowance. I deeply appreciate the encouragement, guidance and support from my main supervisor, Associate Professor Wenhui Duan who gave me this exciting PhD

topic. I would also like to acknowledge the support and guidance of my co-supervisors, Associate Professor Frank Collins, Dr Mainak Majumder and Professor Xiao-Ling Zhao. I would not be able to accomplished this cross-disciplinary research project without their encouragement and constructive suggestions

Moreover, I appreciate the assistances and collaboration offered by my colleagues, Dr Zhu Pan, Dr Asghar Habibnejad Korayem, Dr Mohammad Barati, Mr Bo Zou, Mr Alastair McLeod and the two final year students Mr Li Liu and Mr Jiatian Xu.

Furthermore, I would like to take the opportunity to express my sincere gratitude to the hard-working Monash laboratory staff for their assistance and efforts in my experiments, especially to Mr Long Kim Goh, Mr Kevin Nievart, Mr Alan Taylor and Mr Michael Leach at the Civil Engineering Laboratory. I am grateful to Mrs Jenny Mason and Mrs Irene Sgouras from the Civil Engineering Department office for their much appreciated assistance during my research in Monash University.

Finally, I acknowledge the financial from Australian Research Council and the use of facilities in the Monash Centre for Electron Microscopy.

LIST OF PUBLICATIONS

1. REFEREED JOURNAL PAPERS

Chen, S. J., F. Collins, A. Macleod, Z. Pan, W. Duan and C. Wang (2011). "Carbon nanotube–cement composites: A retrospect." The IES Journal Part A: Civil & Structural Engineering **4**(4): 254-265.

Chen, S. J., W. H. Duan, Q. Wang, F. Collins, M. Majumder and X. L. Zhao (Under Review). "Effects of molecular characteristics of surfactants on dispersion of carbon nanotubes."

Chen, S. J., M. Barati, F. Collins, X. L. Zhao, M. Majumder, C. M. Wang and W. H. Duan (Under Review). "Stability and bundling of surfactant-dispersed multi-walled carbon nanotubes in alkaline environment: Experimental and a Molecular Dynamics simulations based bundle growth model ".

Chen, S. J., B. Zou, F. Collins, X. L. Zhao, M. Majumber and W. H. Duan (2014). "Predicting the influence of ultrasonication energy on the reinforcing efficiency of carbon nanotubes." Carbon **77**(0): 1-10.

Zou, B., **S. J. Chen**, A. H. Korayem, F. Collins, C. Wang and W. H. Duan (2015). "Effect of ultrasonication energy on engineering properties of carbon nanotube reinforced cement pastes." Carbon **85**: 212-220.

Chen, S. J., K. Sagoe-Crentsil, F. Collins, X. L. Zhao, M. Majumder and W. H. Duan (Under Review). "Dispersion and adsorption of carbon nanotubes in fresh ordinary Portland cement pastes.

Zou, B., **S. J. Chen**, F. Collins, G. Cusatis and W. H. Duan (Under Review). "“Linear softening behaviour of carbon nanotube reinforced ordinary Portland cement paste and associated interfacial bond strength between carbon nanotubes and cement matrix”.

2. REFEREED CONFERENCE PAPERS

Chen, S. J., W. H. Duan, F. Collins, X. L. Zhao and M. Majumder (2012). Effects of packing geometry upon the aggregation morphology of sodium cholate on the surface of carbon nanotubes. The 6th International Composites Conference (ACUN-6) Composite and Nanocomposites in Civil, Offshore and Mining Infrastructure. 14-16 November 2012, Melbourne, Australia, Monash University.

Duan, W. H., **S. J. Chen** and M. Hubler (2013). Water Sorption Hysteresis in Cement Nano Slits. Mechanics and Physics of Creep, Shrinkage, and Durability of Concrete: A Tribute to Zdenek P. Bazant: Proceedings of the Ninth International Conference on Creep, Shrinkage, and Durability Mechanics (CONCREEP-9), September 22-25, 2013 Cambridge, Massachusetts, ASCE Publications.

Tarulli, A., A. H. Korayem, **S. J. Chen** and W. H. Duan (2012). Finite element modelling of high strain rate effects in epoxy. The 6th International Composites Conference (ACUN-6) Composite and Nanocomposites in Civil, Offshore and Mining Infrastructure. 14-16 November 2012, Melbourne, Australia, Monash University.

CONTENTS

LIST OF FIGURES

LIST OF TABLES

CHAPTER 1. INTRODUCTION

1.1. Background

The purpose of this study is to enhance the properties of ordinary Portland cement (OPC) paste, which is the key binder to from concrete, with the strongest manufactured nanofibre, carbon nanotubes (CNTs). OPC paste has relatively weak mechanical properties (especially in tension) compared with steel. The huge amount of OPC consumed every year results in massive release of greenhouse gas. CNT reinforced OPC paste would be stronger than plain OPC paste and could therefore reduce the amount of OPC paste used in concrete and the greenhouse gas emission.

Investigation of the CNT-OPC paste pastes composites dates back to 2005 and has shown a promising enhancement effect. Also CNTs have been able to ameliorate the electrical and thermal properties of OPC paste. However, a large variation has been seen in the reported enhancing effect of CNTs, which suggests that stable improvement of mechanical properties cannot be readily achieved and, in some instances, CNTs could even have detrimental effects (Chen, Collins et al. 2011). Therefore, there is a need to refine the fabrication of CNT-OPC paste composite by understanding the reinforcing mechanism of CNTs.

One of the main difficulties in fabricating CNT-OPC paste is the uniform dispersion of individual CNTs in the matrix. CNTs tend to agglomerate due to the strong van der Waals (vdW) attraction between them. Ultrasonication treatment is commonly required to separate CNTs in water and surfactants need to be added into the suspension to prevent CNTs from reagglomerating. Before this study, there has

been no quantitative and direct investigation of CNT dispersion in cement and the effect of ultrasonication.

Once the dispersed CNTs are mixed into cement paste, it has been proposed that CNTs would bridge cracks and would also improve cement hydration and microstructure by acting as nucleation sites (Chen, Collins et al. 2011). Understanding of these effects is limited, however, with insufficient proof or quantification.

In this study, the dispersion of CNTs is investigated comprehensively by molecular mechanics/dynamics (MM/MD) simulation, theoretical development and experiments. The dispersion of CNTs in cement environment is found to be in a semi-stable state, which means that the dispersion can only be considered stable for a limited amount of time. A theoretical bundle growth model is developed to explain the agglomeration process of carbon nanotubes in alkaline environment. In terms of the reinforcing effect, a theoretical crack bridging model, with analytical solution, is developed to quantify the reinforcing effect of CNTs. This model shows good agreement with the mechanical test results of CNT-OPC paste composites and can be used to predict the optimum ultrasonication energy (UE) used in the fabrication process.

1.2. **Research objectives**

This PhD study is funded by an ARC project entitled Tensile Enhancement of Cements Utilising Carbon Nanotubes to Create Stronger, Lighter, More Ductile, and Easier-to-Build Structures. This ARC project covers a wide range of research topics related to CNT-OPC paste composite. These topics include both theoretical modelling and experimental characterization of the dispersion of CNTs in the composite, hydration, mechanical properties and porosity of the composite.

In this PhD thesis, the candidate focuses mainly on the dispersion of CNTs in OPC paste matrix and the mechanical properties of the composite. The goal of the study is to produce better dispersion of CNTs and improved mechanical properties of the composite, as well as resolving the dispersing and reinforcing mechanisms.

This goal can be divided into three objectives: (1) understanding the dispersion of CNTs in water and in aqueous alkaline environment; (2) developing model(s) of the reinforcing effect of CNTs to improve understanding of the reinforcing mechanism of CNTs; (3) based on the model developed in (2), optimizing the reinforcing effect of CNTs.

(1) Understanding the dispersion of CNTs in water and in aqueous alkaline environment.

The dispersion of CNTs in water often requires ultrasonication and the addition of surfactants to break down the CNTs from agglomerates into individual suspended CNTs (Strano, Moore et al. 2003). The surfactant-CNT interaction is one of the main research foci for this objective. Common aqueous based surfactant molecules contain both hydrophobic groups (e.g. –CH3,-CH2-) and hydrophilic groups (e.g. $–COO^-$, $-SO^-_3$). Their dispersion efficiency varies according to their molecular characteristics such as their hydrophobic chain length and the type and position of the hydrophilic groups. In this project, the effect of these molecular characteristics on the surfactant-CNT interaction is investigated via simulations. The surfactant-CNT interaction also influences the stability of the CNTs dispersion in the Ca^{2+} based alkaline environment in OPC paste. Therefore, the stability and agglomerating process of the CNTs in Ca^{2+} solution is also investigated.

(2) Developing model(s) of the reinforcing effect of CNTs to improve understanding of the reinforcing mechanism of CNTs.

CNTs can enhance the mechanical properties of OPC paste via three different effects, namely the filler effect, the modification effect of OPC paste microstructure and the reinforcing effect (Chen, Collins et al. 2011). The reinforcing effect is the major advantage of CNTs compared to traditional nano-sized cement additives such as nanosilica, and is decribed as restraining the cracks from opening by bridging. By virtue of their ultra-high strength and stiffness and the large aspect ratio, CNTs are able to reinforce OPC paste matrix in a manner similar to microfibres and steel re-bars. By developing models to simulate and quantify the reinforcing effect of CNTs, understanding of the mechanism and potential of the CNT reinforcements will be improved.

(3) Based on the model developed in (2), optimizing the reinforcing effect of CNTs.

The model for the reinforcing effect provides guidance for optimization of the CNT-OPC paste composite for superior mechanical properties. The model suggests that to obtain a repeatable and controllable reinforcing effect, two key parameterss must be properly chosen and monitored. The first parameter is ultrasonication energy, which affects both the dispersion and the length distribution of the CNTs. The second parameter is concentration of the dispersed CNTs. Investigation is conducted to quantify and optimise these two factors, after which new models and concepts for future modelling are proposed for durability, microstructure and hydration of CNT-OPC paste.

1.3. **Thesis Structure**

This thesis is organised into eight chapters, five of which are the main chapters with major contributions, as shown in Figure 1.1. Chapters 1, 2 and 8 present the

introduction, literature review and the conclusions and recommendations, respectively. This chapter introduces the background, objectives and structure of the thesis; the contents of Chapters 2-8 are listed below.

Chapter 2 is organised based on the published review paper (Chen, Collins et al. 2011). This review covers the following fields:

- Fabrication of CNT–OPC paste composites
- Hydration behaviour of CNT–OPC paste composites
- Mechanical properties of hardened CNT–OPC paste composites
- Theoretical modelling of CNT and OPC paste

The review provides a broad picture of the advances in research into CNT-OPC composites. Specific attention is given to the mechanical properties and fabrication of the composite. Research gaps are identified based on the review.

In Chapter 3, the interaction energy between ionic surfactants and CNT is calculated using MM simulation to investigate the effects of molecular characteristics of surfactants on the dispersion of CNTs. The results indicate that the preferred aggregation morphology for surfactants with high linearity shifts from parallel to hemi-cylindrical and then to cylindrical when the number of surfactants in the aggregation increases. Also, the results suggest that for surfactants with linear alkyl chains, the longer the chains and the closer the hydrophilic group to ends of the chain, the higher generally is the interaction energy. The study in this chapter provides guidance for selecting suitable surfactants for dispersing CNTs.

Chapter 4 focuses on the effect of a calcium based alkaline environment on the dispersion and reagglomeration of CNTs. Three cement additives are used as surfactants to disperse multi-walled CNTs in saturated $Ca(OH)_2$ solution. The dispersion efficacies of the surfactants are characterized using visual observation, UV-

vis spectrum and scanning electron microscopy (SEM) imaging. The results suggest that the alkaline environment reduces the stability of dispersion of CNTs. CNTs cannot stay dispersed for long, and observable reagglomeration occurs within a few hours. To better understand the reagglomeration process of CNTs in alkaline environment, a MD simulation based aggolomeration growth model is developed. The model can be used to estimate the bundle sizes of CNTs when agglomeration occurs.

Chapter 5 presents a theoretical framework with supporting experiments which is used to develop a model to simulate the bridging effect of CNTs in matrix. The distribution of CNT lengths and the concentration of dispersed CNTs are characterized using SEM images and UV-vis spectrometry. The distribution of CNT lengths and the concentration of dispersed CNTs are incorporated into a micromechanics-based model to simulate the crack bridging behaviour of CNTs. On the basis of the proposed model the optimal UE for reinforcing can be predicted.

Chapter 6 follows the theoretical development in Chapter 5 and presents experimental results which validate and extend the understandings obtained from the crack bridging model. Flexural and fracture properties of the CNT-OPC paste are obtained by three-point-bending tests, which show that the experimental optimum UE matches the theoretical prediction. Moreover, by combining the crack bridging model and the test results, quantitative understanding of the reinforcing mechanism of CNTs is obtained. This is the first time that the crack bridging effect and the micro-structure modifying effect of CNTs have been quantified separately, which helps to improve understanding of nanoparticle-OPC paste interactions.

Chapter 7 deals with the optimization of dispersed CNT concentration in order to maximize the reinforcing effect of CNTs. On the basis of the crack bridging model, the higher the dispersed CNT concentration the better the reinforcing effect. However,

considering thermal dynamics principles (Israelachvili 2011), CNTs cannot remain dispersed if the mass concentration of CNTs is too high. Therefore, experiments are conducted to identify the maximum obtainable concentration of dispersed CNTs. Further, the study investigates the interaction between CNTs and OPC grains, the so-called adsorption of CNTs, in fresh OPC paste.

Chapter 8 provides a summary of the studies presented in the thesis. It also provides a recommended protocol for fabricating CNT-OPC paste which is scalable and applicable in industry. Possible topics for future study are also suggested.

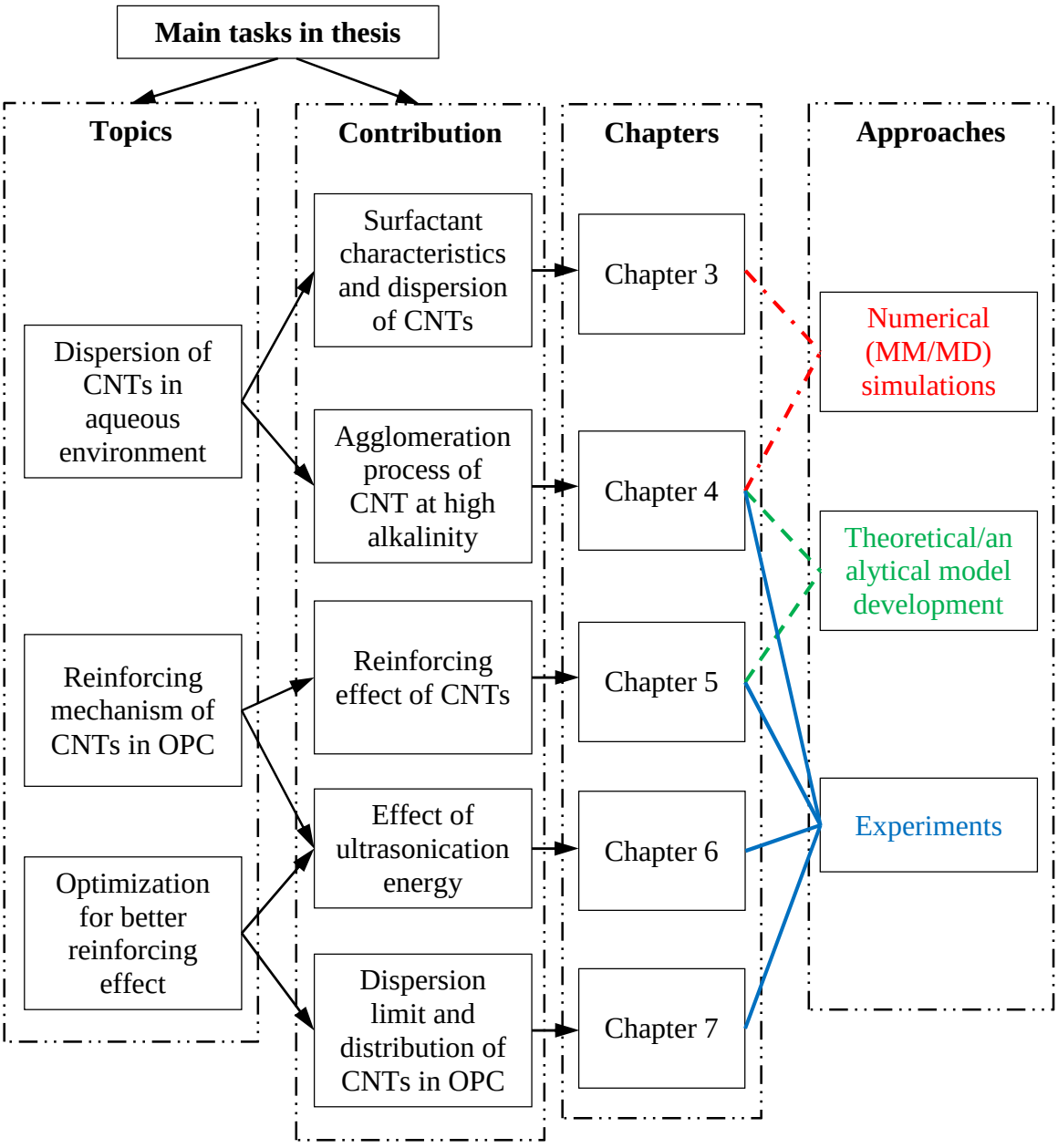

Figure 1.1. Structure and contribution of the thesis.

CHAPTER 2. LITERATURE REVIEW

2.1. Fabrication of CNT-OPC paste composites

After many decades of development, the fabrication method of traditional OPC paste based material, for example, reinforced concrete, has been well established. However, since the incorporation of CNTs leads to more complex interactions in the material, new factors need to be considered in the production of CNT-OPC paste composites. These factors may include: (a) type of CNTs used, (b) technique adopted to disperse CNT in the cement matrix and (c) workability of the fresh composite mix.

Few researchers have investigated single-walled CNT(SWCNT)-OPC paste composites (Makar, Margeson et al. 2005, Sáez de Ibarra, Gaitero et al. 2006, Makar and Chan 2009, Mohamed 2009, Makar 2011); most studies have treated multi-walled CNTs (MWCNTs) with diameters ranging between 10-80 nm, lengths varying from 10-100 µm, and purity above 90 % (Li, Wang et al. 2005, Sáez de Ibarra, Gaitero et al. 2006, Wansom, Kidner et al. 2006, Li, Wang et al. 2007, Cwirzen, Habermehl-Cwirzen et al. 2008, Baoguo, Xun et al. 2009, Cwirzen, Habermehl-Cwirzen et al. 2009, Musso, Tulliani et al. 2009, Xun and Eil 2009, Han, Yu et al. 2010, Konsta-Gdoutos, Metaxa et al. 2010, Konsta-Gdoutos, Metaxa et al. 2010, Manzur and Yazdani 2010, Morsy, Alsayed et al. 2010, Wille and Loh 2010, Luo, Duan et al. 2011, Luo, Duan et al. 2011, Nochaiya and Chaipanich 2011). The two main reasons for using MWCNTs are that (i) production costs of MWCNTs are currently essentially lower than those of SWCNTs, making MWCNTs a more affordable choice for both research and practical applications; and (ii) the larger diameters of MWCNTs allow them to be more easily dispersed due to lower surface areas.

Dispersion of CNTs is difficult within most aqueous media because of the highly attractive vdW forces between the CNT particles (Ko, Gogotsi et al. 2003, Makar and Beaudoin 2004) that tend to cause agglomeration (Thauvin, Rickling et al. 2008, Li, Li et al. 2009). The insufficient dispersion of CNTs has been cited as a key diminishing factor in the performance (Bai and Allaoui 2003, Odegard, Gates et al. 2003) of CNT-OPC paste composites, since poor dispersion of CNTs leads to the formation of many defects in the nanocomposite and limits its mechanical properties (Thostenson, Li et al. 2005, Vaisman, Wagner et al. 2006). On the other hand, better dispersion of CNTs should result in higher interfacial contact area between CNTs and the matrix as well as more evenly distributed stresses in the composites. Therefore, it is essential to consider dispersion techniques in the fabrication of the CNT-cement composites for more effective use of CNTs as reinforcement.

In recognition of this problem, extensive research has been reported in the literature on the development of dispersion technologies, based on both mechanical agitation and chemical treatment approaches. Mechanical agitation by ultrasonication produces temporary dispersion of CNTs, but is often followed by reagglomeration of the dispersed CNTs (Hilding, Grulke et al. 2003). In many cases, therefore, mechanical methods such as ultrasonication (Hunashyal, Lohitha et al. 2011) and magnetic stirring have been used, together with chemical treatment techniques. Chemical approaches have been designed as either a physical (non-covalent) treatment or a chemical (covalent) treatment. In covalent treatment, aggressive chemicals such as neat acids (H_2SO_4 & HNO_3) (Li, Wang et al. 2005, Li, Wang et al. 2007) are often employed to functionalize the CNT surfaces. After the attachment of functional groups on CNT surfaces the functionalized CNTs are less likely to agglomerate. However, functionalization can introduce structural defects, resulting in inferior

properties of the treated CNTs (Coleman, Khan et al. 2006). In contrast, non-covalent treatment is particularly attractive because the dispersing chemical groups are physically attached onto the CNT surface (Duan, Wang et al. 2011) without disturbing the strong covalent bonds of the tube lattice, thereby preserving the desired properties of the CNTs. For this reason, the combination of non-covalent surface treatment, using surfactants or polymers, and mechanical agitation has been widely advocated recently in the preparation of both aqueous and organic solutions containing a high weight fraction of individually dispersed CNTs (Vaisman, Wagner et al. 2006, Wang 2009).

Despite extensive investigation of the dispersion of CNTs in aqueous media, few publications have focused on dispersion efficacy of CNTs within aqueous solutions mixed with OPC paste. Moreover, most of these studies have used surfactant dispersion with the assistance of ultrasonication. Shah et al. (2009) used both silica fume and MWCNTs as micro- and nano-modifiers to the cement paste. Prior to adding to the cement, MWCNTs were dispersed in water using a surfactant and mechanical agitation performed via ultrasonic horn. The morphology and the microstructure of the fracture surface of the MWCNT composites were investigated using an ultra-high resolution field emission SEM and the treated samples showed no significant agglomeration. Luo et al. (2009) assessed the stabilization of dispersed MWCNTs in cement paste by five different types of surfactant:

1. sodium dodecyl benzene sulfonate (NaDDBS, a water reducer and air entrainer),
2. sodium deoxycholate (NaDC, a water reducer and air entrainer),
3. Triton X-100 (TX100, an ethoxylated alkyl phenol that can disperse as well as coat particles, thereby maintaining dispersion),

4. Arabic gum (AG, derived from acacia resin but having retarding effects on cement hydration),
5. cetyltrimethyl ammonium bromide (CTAB, a cationic surfactant, although not commonly used in concrete)

The results of that study showed that the capability of surfactants in dispersing MWNTs roughly decreased in the order NaDDBS+TX100, NaDDBS, NaDC+TX10, NaDC, AG, TX100, CTAB. In addition to surfactants, polymer-based dispersants, such as polyacrylic acid (Jiang, Kowald et al. 2006, Cwirzen, Habermehl-Cwirzen et al. 2008, Cwirzen, Habermehl-Cwirzen et al. 2009) and polyelectrolyte (Wille and Loh 2010), have also been adopted to disperse MWCNTs within OPC paste matrix. These polymer-based dispersants have shown different levels of dispersion capability. Although dispersion can be assisted by surfactants or polymers, it is necessary to draw attention to the compatibility of dispersants with OPC paste. For example, since NaDDBS and NaDC entrain air into the OPC paste, the maximum dosage applied in a CNT-OPC paste must be limited; otherwise excessive air voids tend to compromise mechanical properties. The performance of TX100 in highly alkaline media such as OPC paste is still unclear (Luo, Duan et al. 2009). Moreover, bromine has a documented record of reducing the long-term strength of OPC paste mixtures as well as initiating corrosion of steel in concrete (by a similar mechanism to chlorides). Therefore, the potential detrimental effects of CTAB on OPC pastes must be considered (Luo, Duan et al. 2009). To address these detrimental effects, the use of cement-compatible dispersants has been suggested as a significant consideration in future investigations.

Cement admixtures are attractive candidates as CNT dispersants due to their good compatibility with OPC paste. In the work of Makar (2011), the dispersion of

SWCNTs in different cement admixtures was investigated and poly-naphthalene sulfonate sodium salt (a type of superplasticiser) was found to yield stable dispersion of SWCNTs. However, the fluid mixed with SWCNTs showed a significant increase in viscosity. Moreover, Makar discussed approaches to disperse SWCNTs with anhydrous cement particles and a fabrication method specific for SEM observation of early age samples.

This stiffening effect of the fluid leads to another key aspect of fabrication of CNT-OPC paste composites: the ease with which the fluid mixture can be placed into a mould. The fluidity of the mix tends to decrease because of the large surface areas of CNTs that introduce a significant amount of surface interaction within the mix. When water is added, SWCNT-OPC paste mixtures can become highly viscous and difficult to place, even when prepared with a 0.8 water-cement (w/c) ratio (Makar, Margeson et al. 2005). Such workability problems were first reported by Kowald and Trettin (2004) who incorporated 0.5 wt % MWCNTs and found a 12 % increase in compressive strength. However, the workability of the paste was substantially reduced, and a pressure of up to 125 MPa had to be applied for more than 45 minutes for compaction. Such compaction settings can be impractical for most applications in the construction industry. This indicates the significance of future research into maintaining the workability of CNT-OPC paste composites, especially those with a high weight fraction of CNTs.

In a recent response to the issue of workability and dispersant compatibility, Collins et al. (2012) investigated the dispersion of CNT and the workability of CNT-OPC paste composites using several types of cement-compatible dispersant. In their mini-slump test results, many of the additives (such as alkylbenzene sulfonic acid based air entrainer and lignosulfonate) produced decreased workability after mixture

with MWCNTs. However, unlike the case of SWCNTs (Makar 2011), polycarboxylate, a common superplasticizer, was able to produce good dispersion of the MWCNTs and increased plasticity (around 20 % increase in the mini-slump test results) of the fresh mix. Subsequently, the dispersion effect was characterized by SEM as shown in Figure 2.1. The air entrainer dispersed smaller agglomerates of MWCNTs rather than individual tubes (Figure 2.1-ii) while the polycarboxylate provided reasonably uniform dispersion of CNTs within the paste (Figure 2.1-iii). Showing no conflict between dispersion of MWCNTs and workability of the fluid mixture, these results are encouraging and further investigation into improving fabrication techniques is needed. However, the fabrication methods currently used in CNT-OPC paste mixtures in the research community are still at laboratory scale and future investigations are required to move the production of CNT-OPC paste composites towards practical civil engineering implementations.

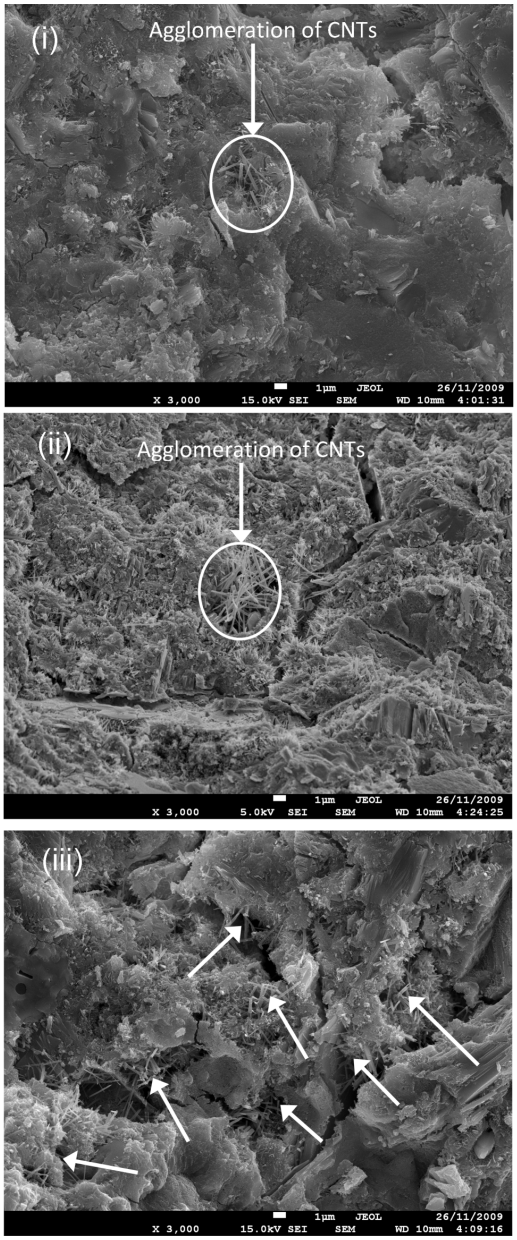

Figure 2.1 SEM Images showing the effect of admixtures on dispersion of CNTs: ((i)-(iii) represent no admixture, air entrainer, and polycarboxylate, respectively. White arrows indicate the locations of CNTs dispersed within the sample) (Collins, Lambert et al. 2012)

2.2. **Hydration behaviour of CNT-OPC paste composites**

Only limited studies have hitherto been conducted on the effect of CNTs on the hydration of OPC. Nevertheless, there is evidence that CNT inclusion, even in a bundled form, accelerates the hydration progress in the cement paste. This effect was

first shown by Makar et al. (2005), who found that the addition of SWCNT bundles to OPC paste resulted in more comprehensive hydration of the OPC paste, as evidenced by an increase in Vicker's hardness (about 6 times higher than companion OPC paste samples prepared with the same water-to-cement ratio). However, this enhancement effect was observed only during the early ages of the composite and disappeared after 14 days. The researchers suggested that the SWCNT bundles stimulated the hydration reaction by acting as nucleating sites for the growth of the hydration products (see Figure 2.2). Also, the hydration morphology was found to be altered to reticular structures, with SWCNTs coated by calcium silicate hydrate (C-S-H) (Makar and Chan 2009). These structures could lead to a more refined hardened paste and their potential effects on the aggregate-paste transition zone would be worthy of further study.

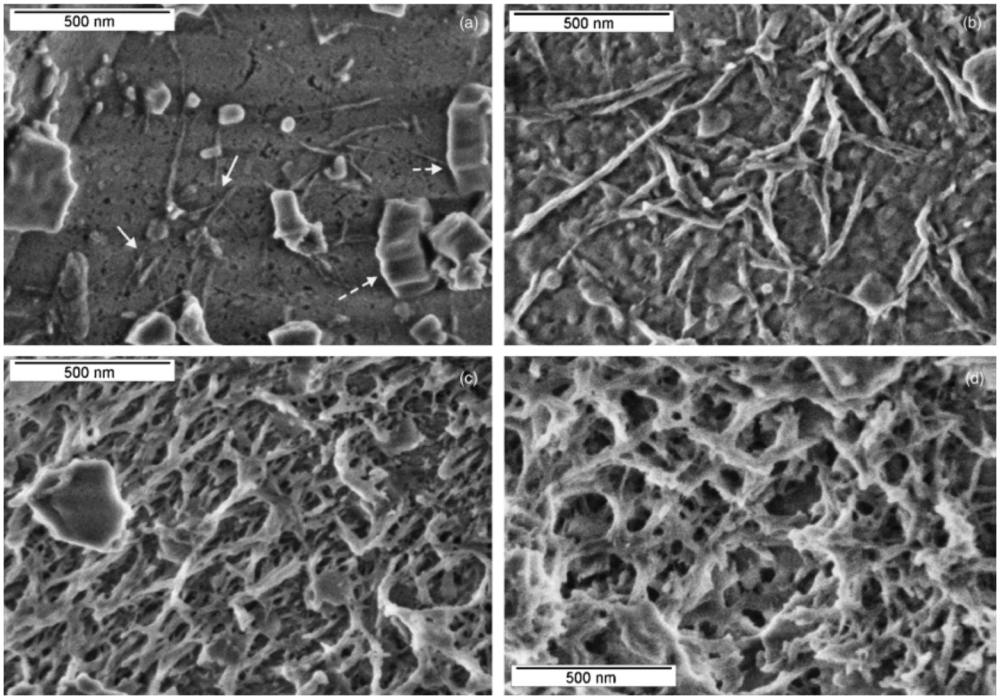

Figure 2.2 Growth of C-S-H on CNT network during hydration. From (a) to (d), the hydration time are 60 minutes, 135 minutes, 180 minutes and 240 minutes respectively (Makar and Chan 2009).

Well-dispersed CNTs in the mix enhance the hydration progress of cement. In the study of Luo et al. (2009), MWCNTs were dispersed by surfactants within the OPC paste, resulting in hydrated cement products with a dense and homogeneous texture. It was found that the dispersed MWCNTs were coated with hydrated products forming a net-like distribution that bridged the microcracks within the cement matrix. Kowald and Trettin (2009) investigated a mixture of pure tricalcium silicate (C3S) and MWCNTs. The dispersion of the MWCNTs was achieved by ultrasonication of the mixture for 28 minutes. Next, a polycarboxylate-based superplasticizer was added and sonicated for 2 minutes. The amount of $Ca(OH)_2$ in the hardened paste was subsequently analysed using thermogravimetry analysis (TGA), the results showing that the MWCNTs had a small effect on the total amount of $Ca(OH)_2$ generated during hydration. Instead, the proportion of crystalline $Ca(OH)_2$ was reduced. Since the accumulation of crystalline Ca(OH)2 contributes to both reduced strength and permeability at the interfacial transition zone formed between aggregate and cement paste, the presence of MWCNTs may lead to improved durability and strength.

2.3. Mechanical properties of hardened CNT-OPC paste composites

Because the use of CNTs as nanoscale tensile reinforcement to achieve higher mechanical performance is one of the main purposes for developing CNT-OPC paste composites, more studies have reported on this area than on other properties of the composite. Besides improvements in Vicker's hardness as mentioned in section 2.2, the enhancing effects of CNTs have also been observed in Young's modulus, compressive strength, flexural strength and modulus of rupture (see Table 2.1).

In an early attempt to incorporate CNT into cement, Campillo et al. (2003) used both MWCNTs and SWCNTs to study their enhancement effect on the compressive

strength of cement pastes. Results showed that the composite paste containing MWCNTs had a significantly higher compressive strength than counterparts containing SWCNTs (see Table 2.1). This observation may be due to the superior dispersion of MWCNTs because of their lower surface area and better MWCNTs-CNT bonding introduced by the functional groups on MWCNT surfaces.

Table 2.1 Increments in mechanical properties of cement-based material after incorporation of CNTs

Researchers	Type of CNTs	Dispersion method	Age of testing	*Increase in Mechanical properties*			
				Young's Modulus	Compressive strength	Flexural strength	Modulus of rupture
Campillo et al. (2003)	MWCNT	mechanical	14 days	-	30 %	-	-
	SWCNT	mechanical		-	6 %	-	-
Li et al. (2005)	MWCNT	covalent	28 days	-	19 %	25 %	-
Li et al. (2007)	MWCNT	covalent	28 days	-	29 %	-	-
	MWCNT	mechanical		-	22 %	-	-
Cwirzen et al. (2008)	MWCNT	non-covalent	-	-	50 %	-	-
Cwirzen et al. (2009)	MWCNT	non-covalent +covalent	28 days	-	-	20 %	-
Konsta-Gdoutos et al. (2010)	MWCNT	non-covalent	28 days*	45 %	-	25 %	-
Konsta-Gdoutos et al. (2010)	MWCNT	non-covalent	28 days*	35 %	-	40 %	-
Musso et al. (2009)	MWCNT	covalent	28 days	-	-	-	35 %
	MWCNT	non-covalent		-	-	-	- 60 %
Nasibulin et al. (2009)	MWCNT	direct grow	28 days	-	>100 %	-	-

**: similar increase is also reported for testing age of 3 and 7 days.*

After the study by Campillo et al, experiments reported in the literature mainly focused on incorporating MWCNTs using a wide range of dispersion techniques. Initially, dispersing MWCNTs by functionalization (the covalent method) was more frequently used in preparing specimens for mechanical tests. In the study of Li et al. (2007), as shown in Table 2.1, the increment in compressive strength of the specimens with acid treated MWCNTs was shown to be 7 % greater than those with

mechanically dispersed MWCNTs. This increase could be attributed to the chemical bonds formed between the functionalized MWCNTs and the C-S-H phase which strengthened the interaction between MWCNTs and the matrix. Although the 29 % improvement reported by Li et al. (2007) using covalent dispersion was close to the results reported by Campillo et al. (2003) using mechanical excitation only, it is noted that the tests represented composites at different ages. The improvement in strength at 28 days might be less than that at 14 days, considering the hydration effects discussed in section 2.2. Still, the highest increment of compressive strength and flexural strength obtained by covalent dispersion was below 30 %, making it unattractive for practical applications.

Dispersion using surfactants (non-covalent method) has been found especially effective in improving flexural strength. While the combination of the non-covalent and covalent methods produced 20 % higher compression strength than using functionalized MWCNTs alone (Cwirzen, Habermehl-Cwirzen et al. 2008), all reported increases (from 20 % to 40 %) in flexural strength were the result of non-covalent dispersion (Cwirzen, Habermehl-Cwirzen et al. 2009, Konsta-Gdoutos, Metaxa et al. 2010). A 45 % increase in the Young's modulus was also reported by Konsta-Gdoutos et al. (2010), who suggested that the surfactant/MWCNT ratio might affect the mechanical properties of the composites. Moreover, when the non-covalent method was used, the stress-intensity factor (a factor that describes the stress state near the tip of a crack) of the composites was shown to improve by nearly 80 % (Luo, Duan et al. 2011), thereby indicating superior performance in crack resistance. While chemical-bonds and superior interlock may be contributory factors offered by the covalent dispersion, the non-covalent dispersion maintains the superior properties of CNTs. The aforementioned studies provide insights into the different performance of

the two major dispersion methods. However, more effort is needed to develop better dispersion methods.

MWCNTs have also been used together with other micro- or macro-particles/fibres to improve the mechanical properties of cement-based composites. For instance, studies based on cement mixes containing sand and other cement additives have shown that the modulus of rupture could be improved by about 35 % when non-functionalized MWCNTs were added in the composite but the modulus of rupture decreased to around 40 % of the original value when functionalized MWCNTs were used (Musso, Tulliani et al. 2009). This decrease was shown to be a result of poor hydration caused by the functionalized MWCNTs. Moreover, a considerable improvement in the bonding between steel bars and concrete matrixes (Wille and Loh 2010) has also been reported. Also, Chaipanich et al. (2010) introduced carbon nanotubes to a fly ash-OPC paste blended cement to produce CNT-fly ash composites and achieved an increase of nearly 10 % in the compressive strength of the composite material. At the same time, inspection related to the enhancement effect of CNTs on mixtures of OPC paste and nano-metalkaolin revealed increases of up to 29 % in the compressive strength of the material (Morsy, Alsayed et al. 2010). These studies appear to indicate feasible future implementations of CNTs to enhance the mechanical properties of concrete or reinforced concrete structures.

In addition to the use of surfactants or functionalization, another fabrication method is to grow CNT or carbon nanofibres (CNFs) directly on the cement particles by a chemical vapour deposition method (Cwirzen, Habermehl-Cwirzen et al. 2009, Nasibulin, Shandakov et al. 2009). Although particular cases have shown more than double increase in compressive strength, there were problems with reduced workability, variation in the amount of CNTs/CNFs grown on the cement particles,

reduced hydration of cement and variable setting times (Nasibulin, Shandakov et al. 2009).

Although the currently demonstrated enhancement effects are still a far cry from satisfactory practical use, the mechanical properties of CNT-cement composites may be further improved when a more efficient dispersion method is developed in future. Furthermore, the bonding, anchorage, and interlocking between CNTs and the cement matrix also play significant roles in the enhancement effect (Makar 2011). Since these CNT-matrix interactions are still poorly understood, a considerable amount of future research work, especially theoretical and numerical studies, is still required to explore the true potential of CNTs as cement reinforcement. A superior reinforcement effect will be achieved if the dispersion of CNTs in the OPC paste matrix is improved. The improvement may differ from static loading to dynamic loading.

2.4. **Theoretical modelling**

Although a considerable amount of experimentation has been conducted with respect to CNT-OPC paste composites, theoretical modelling of the composites is rarely seen in the literature. This glaring gap in theoretical modelling of CNT-OPC paste composite must be addressed. Various modelling techniques have been established that can be applicable to CNT-cement composites. Thus, this section reviews the implementation of these modelling methods on either cement without CNTs or CNTs in non-cement matrix. Although these studies may be not directly relevant to CNT-OPC paste composite, they can assist in building the foundation or show potential paths for developing models of CNT-OPC paste composites in the near future.

Continually increasing computing power has allowed computational materials science to predict the microstructure and atomistic interactions by MD simulation. MD simulations have been widely applied in studying calcium silicate hydrate (C–S–

H) structures and other hydrated products by constructing atomistic models for these materials (see Figure 2.3). Early simulations involved only around 2500 atoms in a unit cell, using pair and three-body potentials (force fields) (Stillinger and Rahman 1978, Soules 1979, Feuston and Garofalini 1989) to simulate the partially covalent properties of the hydrogen and silicon bonds (Faucon, Delaye et al. 1997). Besides using pre-defined potentials, more recently, *ab initio* MD simulations have been implemented to study the structure of the hydrogen bonds formed by H_2O molecules and OH groups in cement (Churakov 2009) and the hydrogen bond connectivity in the structure of Jennite (Churakov 2008). In *ab initio* MD modelling, the forces acting on the nuclei are recalculated for each new MD trajectory (Marx and Hutter), where in a way some computation speed is sacrificed for a higher accuracy. *Ab initio* MD simulations have also helped to address the origin of the strength in cement-based materials (Gmira, Zabat et al. 2004, Pellenq and Van Damme 2004), suggesting that short- and medium-range attractive electrostatic forces are the major source of C-S-H cohesion whereas capillary forces and vdW force have considerable and marginal contributions, respectively (Gmira, Zabat et al. 2004).

With respect to problems related to aqueous interface, the chloride bonding at the aqueous interface of cement materials has been modelled using MD simulations, and the modelling results are in agreement with experimental observations (Terzis, Filippakis et al. 1987) on the abundance of chloride bonding on C-S-H in cement materials (Kalinichev and Kirkpatrick 2002). Moreover, MD simulations have provided detailed information about the behaviour of water at cement surfaces, and therefore theoretical modelling can be used to estimate the diffusion coefficient of surface-related water (Kalinichev, Wang et al. 2007).

Some recent studies have employed MD simulations to seek approaches to enhancing or reinforcing hardened cement. With the assistance of MD simulation, methods to enhance the performance of cement based material can be developed or assessed. For instance, atomic scale forces can be calculated after modifying the bonding scheme in C–S–H, facilitating the development of more strongly bonded cement structures that can be controlled to improve the properties of the cement such as early age and long-term strength (Pellenq, Lequeux et al. 2008). In terms of modelling related to graphitic reinforcements in cement, MD simulations have been used to study the interfacial interaction between functionalized graphite sheet and C-S-H, revealing methods to influence graphitic structure/cement interaction by changing the number of polar oxygen containing groups (Sanchez and Zhang 2008). The ability to obtain predictive results as shown above is a significant merit of MD simulations as there are very few experimental approaches at such small scale. Thus MD simulations can be an essential method for studying the micro-scaled bonding between CNT and cement matrix and helping to develop better fabrication schemes.

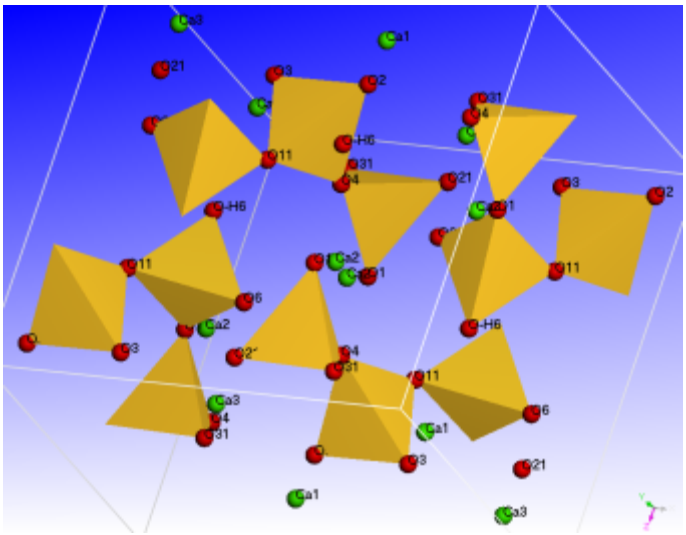

Figure 2.3 Atomistic model of Tobermorite9 for approximation of C-S-H structure plotted by the present author using the data reported by Merlino (1999).

However, atomic modelling techniques (such as MD alone) are limited to systems with a small number of molecules and atoms. Hence, attempts have been made to

apply continuum mechanics models to better accommodate the results from MD for investigating macro-level behaviour of CNT-composites. Among all the continuum mechanics approaches, the technique of representative volume element (RVE) modelling, as shown in Figure 2.4, has been commonly used by researchers studying the material properties of nanocomposites. RVE modelling is based on continuum mechanics for predicting the effective properties of random heterogeneous materials by considering a given microstructure volume. In early simulations studies, Liu and Chen (2003) proved the feasibility and accuracy of evaluating material constants by applying the RVE concept to simulate a single CNT and its surrounding matrix. Moreover, RVE studies to date have suggested that embedded CNTs have a contributory effect on the tensile strength (Tserpes, Papanikos et al. 2008), and modulus (Liu and Chen 2003, Zhang and He 2008) of CNT composites. When RVE is applied to modelling CNT-polymer composites, it has been able to produce predictions in agreement with experimental results (Li and Saigal 2007). Apart from mechanical properties, with the RVE model, the thermal behaviour of CNT composites can be analysed (Singh, Tanaka et al. 2007, Zhang and Tanaka 2007) and numerical formulas have been proposed to calculate the equivalent thermal conductivity of CNT composites (Singh, Tanaka et al. 2007).

In RVE modelling, the stiffness of CNT-composites has been found to be very sensitive to the property of the interphase or contact zone between CNT and the matrix material (Zhang and He 2008), but MD simulations are essential to determine these interfacial properties. Thus, the more preferred modelling method needs the integration of different scales (Liu and Chen 2003), balancing both available computation resources and accuracy. An example of such a method that has been developed is the quasi-continuum approach which maps individual atoms into a finite

element model (Gates, Odegard et al. 2005). Yet there is still a long way to go for such multi-scale simulation methods to have widespread applications. In summary, since few MD modelling practices have been seen in the literature that deals with the interaction between CNTs and C-S-H, there is certainly a need for a considerable amount of future study to develop satisfactory models for CNT-cement composites.

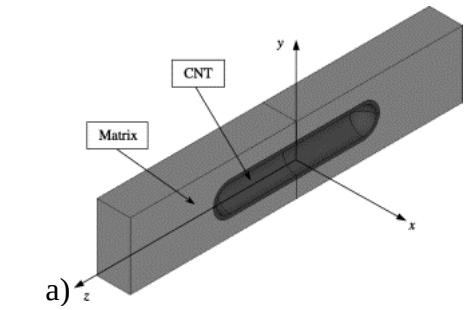

a)

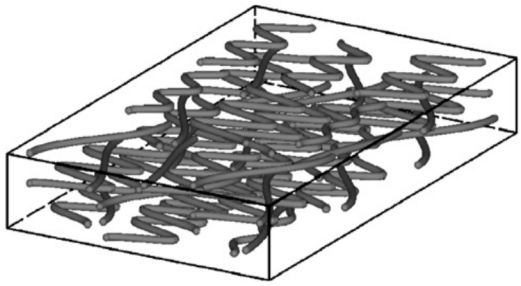

b)

Figure 2.4 RVE models of CNT-composite: a) a small-scale model with single straight CNT (Chen and Liu 2004), b) a large model with curved multiple CNTs (Zhang and Tanaka 2007).

2.5. Research gaps

From the literature review in this section, the following research gaps are identified:

1. Reported fabrication methods show large discrepancies in terms of the improvement in mechanical properties of OPC pastes by incorporating CNTs.
2. No quantitative investigation has been reported of the dispersion of CNTs using cement-compatible surfactant in water.

3. No investigation has been reported of the dispersion and distribution of CNTs in Ca+ based alkaline environment and fresh OPC paste.
4. Limited proof and understanding exist of the reinforcing effect of CNTs on OPC pastes.
5. Limited understanding exists of the effect of ultrasonication on the reinforcing effect.
6. Few experimental techniques have been reported to investigate the interaction between CNTs and the OPC grains in fresh CNT-OPC paste.

These research gaps are addressed in the following chapters.

CHAPTER 3. MOLECULAR MECHANICS SIMULATION OF CNT-SURFACTANT INTERACTION

3.1. Introduction

The self-aggregation phenomenon of pristine CNTs in an aqueous environment, which leads to difficulties in the uniform dispersion of CNTs, significantly hinders the application of CNTs in an aqueous based matrix such as OPC paste. To cope with this problem, two dispersion methods are commonly employed. The first is covalent functionalization of the CNT surface (Kahn, Banerjee et al. 2002, Pompeo and Resasco 2002) while the second method is the physical wrapping of CNTs using surfactants or polymer (Liu, Rinzler et al. 1998, Islam, Rojas et al. 2003, Dyke and Tour 2004, Vaisman, Wagner et al. 2006). Unbundling CNTs using surfactants combined with ultrasonication is preferred in many applications owing to the preservation of the original mechanical and electrical properties of the CNTs (Tan and Resasco 2005, Coleman, Khan et al. 2006). A considerable number of experimental studies have investigated dispersion of CNTs utilizing various surfactants (Bandyopadhyaya, Nativ-Roth et al. 2002, Islam, Rojas et al. 2003, Moore, Strano et al. 2003, Richard, Balavoine et al. 2003, Dyke and Tour 2004, Yurekli, Mitchell et al. 2004, Hertel, Hagen et al. 2005, Tan and Resasco 2005, Tan and Resasco 2005, Green, Duch et al. 2009, Ghosh, Bachilo et al. 2010) and obvious differences in terms of dispersion efficacy have been found between tested surfactants.

Although the surfactant facilitated dispersion of CNTs in water is influenced by a number of factors such as the concentrations of SWCNTs and surfactant (Richard, Balavoine et al. 2003, Paria and Khilar 2004, Shin, Premkumar et al. 2008),

ultrasonication intensity and duration (Islam, Rojas et al. 2003, Tan and Resasco 2005), size and surface curvature of CNTs (Tummala and Striolo 2009) and presence of counter ions (Paria and Khilar 2004), the molecular structure of the surfactant determines the maximum exfoliation and stabilization of CNTs that a particular type of surfactant can provide (Islam, Rojas et al. 2003, Tan and Resasco 2005, Blanch, Lenehan et al. 2010).

Understanding of the effects of molecular structure of surfactants on dispersion is still limited due to the lack of experimental techniques to revolve CNT-surfactant interaction at atomic scale. Therefore, MM and MD simulations play a significant role in understanding surfactant-facilitated CNT dispersion since they can provide atomic resolution.

In this chapter, MM simulation is employed to investigate (1) the interaction energy between different surfactants and a CNT and (2) the different surfactant aggregation morphologies on the CNT surface.

Interaction energy describes the intensity of interaction between individual CNTs and attached surfactants, which is different from the potential of mean force that is commonly used in MD studies to describe the interaction between two CNTs in solution (Lin and Blankschtein 2010, Tummala, Morrow et al. 2010, Xu, Yang et al. 2010, Uddin, Capaldi et al. 2011). This interaction energy is the main contributor to the self-energy (Israelachvili 2011) of an individual CNT in the dispersant. Higher self-energy of a dispersed CNT increases the fraction of dispersed CNTs in the solution, based on Boltzmann distribution (Israelachvili 2011).

Aggregation morphology has long been a debated topic. Four different types of aggregation have been suggested by different researchers: parallel aggregation (Tummala and Striolo 2009, Tummala and Striolo 2009, Lin and Blankschtein 2010),

random distribution (Yurekli, Mitchell et al. 2004, Patel and Egorov 2005, Qiao and Ke 2006, Tummala and Striolo 2009), hemi-cylindrical aggregation (Richard, Balavoine et al. 2003, Wu, Hudson et al. 2006, Mackiewicz, Surendran et al. 2008, Thauvin, Rickling et al. 2008, Calvaresi, Dallavalle et al. 2009, Tummala, Morrow et al. 2010) and cylindrical aggregation (O'Connell, Bachilo et al. 2002, Matarredona, Rhoads et al. 2003, Cardenas and Glerup 2006, Wallace and Sansom 2007, Calvaresi, Dallavalle et al. 2009, Xu, Yang et al. 2010). The diversity here certainly indicates that future study is indispensable for improving the understanding of surfactant-CNT dispersion.

As shown in Figure 3.1, typical ionic surfactants are chosen as representing different characteristics in their molecular structure, namely the (1) the presence of ring moieties and linearity of the surfactant structure (Islam, Rojas et al. 2003, Li, Reeve et al. 2005, Xu, Li et al. 2006), (2) the position of the hydrophilic head group branch (Stigter 1974, Conboy, Messmer et al. 1997, Islam, Rojas et al. 2003, Paria and Khilar 2004, Ma, Boyd et al. 2006, Jurasin, Habus et al. 2010) and (3) alkyl chain length (Somasundaran, Fuerstenau et al. 1964, Connor and Ottewill 1971, Fan, Somasundaran et al. 1997, Wang, Han et al. 1999, Wu and Pendleton 2001, Atkin, Craig et al. 2003, Islam, Rojas et al. 2003, Paria and Khilar 2004). These surfactants are sodium dodecyl sulfate (SDS) (Bandyopadhyaya, Nativ-Roth et al. 2002, Islam, Rojas et al. 2003, Moore, Strano et al. 2003, Richard, Balavoine et al. 2003, Dyke and Tour 2004, Yurekli, Mitchell et al. 2004, Hertel, Hagen et al. 2005, Tan and Resasco 2005), sodium dodecyl-benzene sulfonate (SDBS) isomers (Islam, Rojas et al. 2003, Moore, Strano et al. 2003, Hertel, Hagen et al. 2005, Tan and Resasco 2005, Tan and Resasco 2005), sodium octyl-benzene sulfonate (SOBS) (Islam, Rojas et al. 2003), sodium butylbenzene sulfonate (SBBS) (Islam, Rojas et al. 2003) and sodium cholate

(SC) (Hertel, Hagen et al. 2005, Tan and Resasco 2005, Green, Duch et al. 2009, Ghosh, Bachilo et al. 2010). In this chapter, SDBS-2, SDBS-3, SDBS-6, SOBS-2 and SBBS-2 refer to specific isomers with the branches attached to specified positions in the alkyl chain (as illustrated in Figure 3.1), and SDBS, SBBS and SOBS are collective names for all positional isomers. Interaction energy is also used to study the preference for different aggregation morphologies. The physical properties of the surfactants are shown in

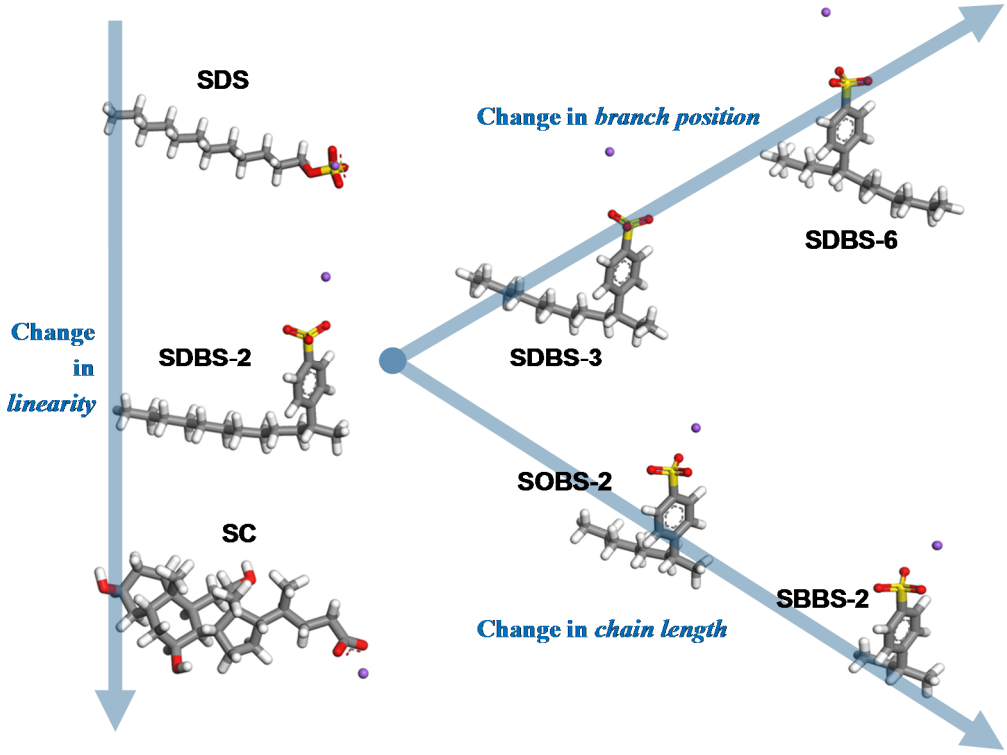

Figure 3.1 Surfactants used in this study with varied linearity, head group branch position and chain length. Grey: carbon; red: oxygen; yellow: sulphur; white: hydrogen; purple: sodium.

Table 3.1. Properties for the surfactants (Sigma-Aldrich 2014).

Surfactant	Density (g/cm^3)	Molar Mass (g/mol)	CAS No
SDS	1.01	288.37	151–21–3
SDBS-2, SDBS-3, SDBS-6	NA	340-352	25155-30-0
SOBS	NA	294.39	6149-03-7
SBBS	1.124	180.16	515-42-4
SC	NA	430.55*	206986-87-0*

*Data for hydrates.

3.2. MM Simulation

A (10, 10) SWCNT 49.19 angstrom in length was placed in free space with surfactant assemblies wrapped on the exterior surface of the tube. MM simulations use geometry optimization (by conjugate-gradient method) to find the equilibrium state of these surfactant aggregation structures. The atomic interaction was modelled by the COMPASS force field (Condensed-phased Optimized Molecular Potential for Atomistic Simulation Studies) (Rigby, Sun et al. 1997). This force field has been proven to be applicable in describing the mechanical properties of CNTs (Duan, Wang et al. 2007, Wang, Duan et al. 2007) and the interaction between SDS and CNT (Duan, Wang et al. 2011). The force field setting was identical to that used in a previous study (Duan, Wang et al. 2011) with a cut-off distance of 9.5 for both vdW and electrostatic forces. Water molecules were not included in the simulation since water molecules were excluded from the hydrophobic SDS-CNT interface as suggested by recent studies (O'Connell, Bachilo et al. 2002, Calvaresi, Dallavalle et al. 2009). The coordinates of the atoms in the SWCNT were fixed since only the related movement between surfactants and SWCNT was of interest. The equilibrium state was considered to be reached when the maximum force in the molecular structure was less than 0.001 kcal / mol per angstrom (Duan, Wang et al. 2011).

Three initial configurations, namely parallel aggregation, hemi-cylindrical aggregation and cylindrical aggregation, were adopted, based on the aggregation morphologies suggested in past studies. No random aggregation was included as one of the initial configurations since there was no deterministic structure for a random distribution. Examples of these three morphologies are shown in Figure 3.2. In the parallel configuration as shown in Figure 3.2-a and -c, two rows of surfactants were placed around the CNT surface. The centroids of these two rows were aligned approximately with the 1/4 length position and 3/4 length position along the tube. In the hemi-cylindrical configuration indicated in Figure 3.2-b and -e, the diameter of the hemi-cylinder was used as the length of the tube (49.19 Å) for SDBS-2 to fully cover the exterior surface of the tube. The diameter of the hemi-cylinder used there was consistent with the experimentally observed size for SDS (45 ±5 Å) (Richard, Balavoine et al. 2003). The same hemi-cylinder diameter was applied to SDS, SDBS isomers and SC because they had similar molecular size in the longitudinal direction (around 20.6 Å for SDS, 18.0 - 22.5 Å for SDBS isomers and 18.0 Å for SC). However, for SOBS-2 and SBBS-2, which were of significantly smaller size (around 13.1 -17.6 Å for SOBS-2 and 7.8-12.3 for SBBS-2), the diameters of the hemi-cylinder and tube were reduced to 39.35 Å and 27.05 Å for SOBS-2 and SBBS-2 respectively. The cylindrical configuration had surfactants with the hydrophilic head group facing opposite to the tube in the radial direction, as shown Figure 3.2-c and -f. In all three types of initial configuration, the gap between the surface of CNT and the surfactants was kept around 3.5 Å to ensure that the surfactants and CNT were interacting within the cut-off distances. The benzene rings and head groups were rotated to face outwards (as shown in Figure 3.2-b and e) in the initial configuration of SBDS isomers, SOBS and SBBS. In the hemi-cylindrical and cylindrical

configurations, all surfactant molecules were rotated by a random angle according to their longitudinal axis. These random rotations were applied to eliminate the un-balanced force that would be introduced by head groups all facing in one direction.

Configurations with different numbers of surfactants (surface density) were simulated. For each type of initial configuration, the simulation began with a very small surface density (< 1 molecule/nm^2) which then increased until the surface was too crowded to maintain the morphology. The interaction energy was calculated as described in a previous publication (Duan, Wang et al. 2011). Since only two rows of surfactant were placed in each parallel configuration and there were gaps between each row (Figure 3.2-d), the surface density and the interaction energy calculated had to be multiplied by a factor to give results corresponding to full coverage with no gaps between the rows. This factor was calculated as twice the surfactant length divided by the length of the tube. As an exception, the rhombus-like shape of SC molecules actually allowed rows of SC in the parallel aggregation to engage with each other as gears and then reduced the space occupied by each row of SC. It was estimated that this reduction was around 1/3, and that was considered in the calculation of the previously mentioned factor.

Further, to allow comparison between the simulation results obtained here and reported experimental results, the concentration values in experimental studies were converted to surface density based on a theoretical SWCNT surface, which was 1300 m^2/gram (Peigney, Laurent et al. 2001, Donaldson, Aitken et al. 2006, Sun, Nicolosi et al. 2008), with the assumption that all the surfactants were attached to the SWCNT surface (Tan and Resasco 2005).

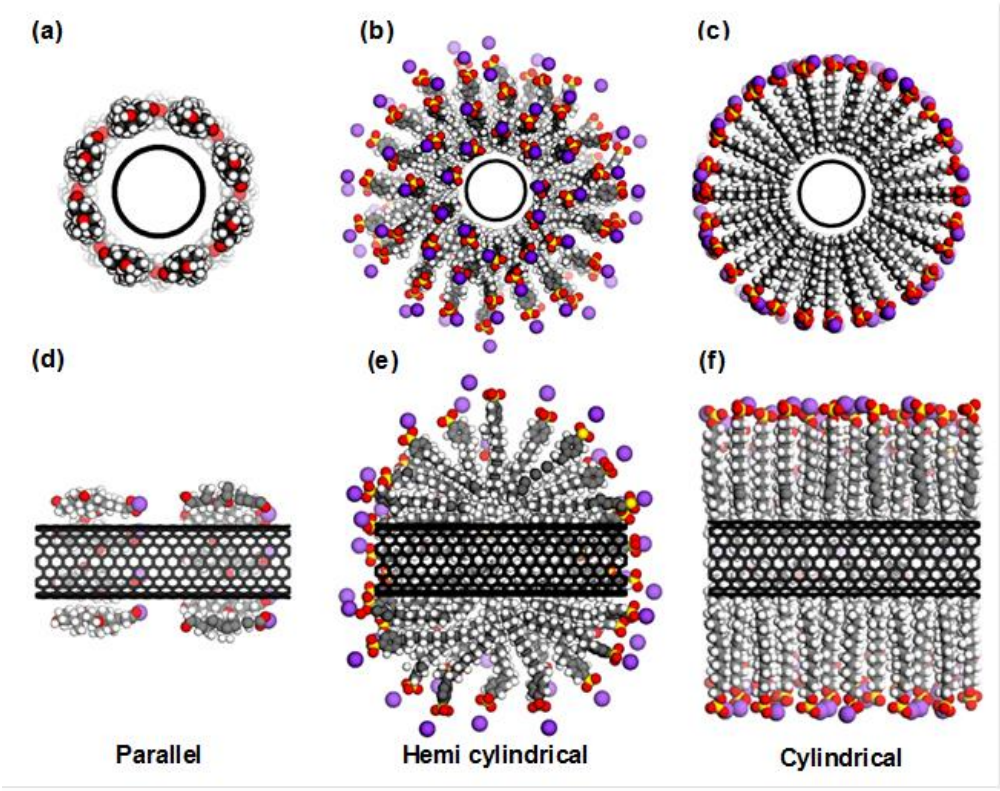

Figure 3.2 View across the CNT (a-d) and view of cross-sections (d-f) cut along the longitudinal central axis of the SWCNT for the initial configuration of a parallel attached SC, a hemi-cylindrically attached SDBS-2 and a cylindrically attached SDS. In a and d, the SCs are placed such that the sides with -CH_3 groups face the CNT (Lin and Blankschtein 2010).

3.3. Results and discussion

3.3.1. Effect of molecular linearity on interaction energy and morphology

Figure 3.3 shows the variation of interaction energy against change in surface density for SDS, SDBS-2 and SC under different morphologies. The results here indicate dependence of interaction energy on aggregation shape.

As indicated in Figure 3.3-a, at low surface density (around 0 – 2.0 molecules/nm^2), parallel aggregation of SDS produces more negative interaction energy than the other two types of morphology. Within this range, the interaction energy increases almost linearly before the surface density reaches a threshold where the number of surfactants per row is the optimum. The optimum surface density

allowed formation of the densest aggregation and yielded the peak values in Figure 3.3-a.

When the surface density of SDS further increases to around 3.5 molecules/nm^2, as shown in Figure 3.3-a, the interaction energy generated using a parallel configuration is approximately in line with that predicted using a hemi-cylindrical configuration; after that point the hemi-cylindrical aggregation become the optimum with highest interaction energy until it is overcome by the cylindrical morphology at a surface density around 7.4 molecules/nm^2.

It is suggested that the energetic preference for morphology regarding surface density for SDS is parallel aggregation (Figure 3.3-a-i) within the approximate range 0-2, hemi-cylindrical (Figure 3.3-a-ii) within around 3.4-7.4 molecules/nm^2 and cylindrical (Figure 3.3-a-iii) for more than 7.4 molecules/nm^2. The maximum (saturation) surface density of SDS on the SWCNT was around 9.3 molecules/nm^2, beyond which the SDSs near the end lost contact with the SWCNT (Figure 3.3-a-iv).

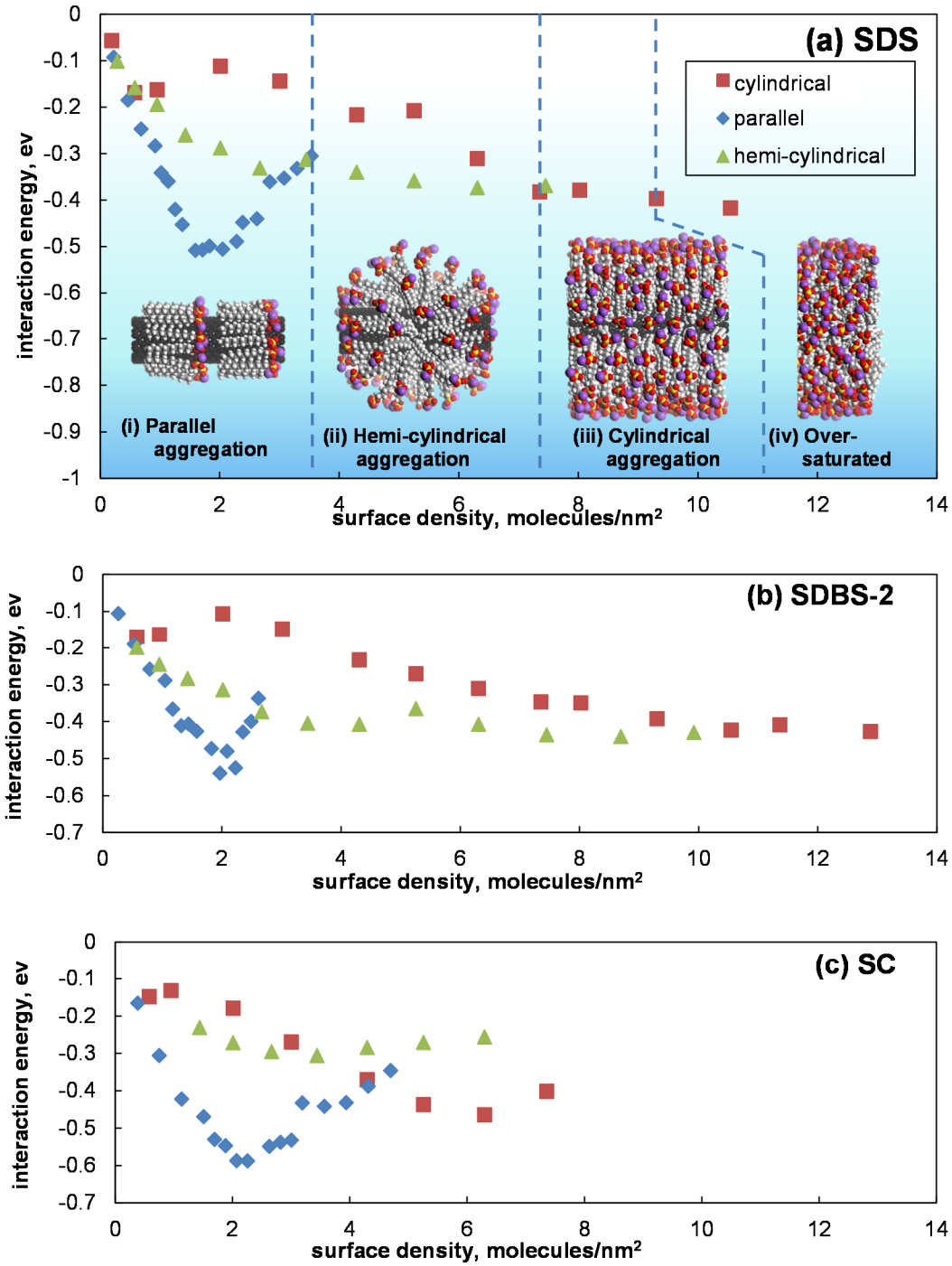

Figure 3.3 Interaction energy curves of three different morphologies for SDS (a), SDBS-2 (b) and SC (c). (i) - (iv): Typical SDS aggregation structure of different morphologies. The corresponding surface densities of (i) - (iv) are 1.59, 4.29, 7.35 and 10.55 molecules/nm^2, respectively.

Note that no morphological preference is suggested for the post-peak region of the parallel aggregation (surface density 2-3.4 molecules/nm^2), because the aggregation morphology can become highly unstable, with some surfactant molecules squeezed out from the single parallel layer. This region may be a transition zone from

parallel to hemi-cylindrical aggregation, where no clear preference for morphology may exist. This is in agreement with the findings of (Moore, Strano et al. 2003), where transitions were observed in the relation between the amount of dispersed CNT and surface density when the surface density isaround 1.9 molecules/nm^2. Also, a rapid change of surface tension of the CNT dispersion was reported at a surface density around 2.7-3.0 molecules/nm^2 (Grossiord, van der Schoot et al. 2007).

Interestingly, the preference for aggregation morphologies can be used to explain experimental observations of the surfactant aggregation morphology on the CNT surface as well as to predict the surface density of parallel aggregation. In the transmission electron microscopy (TEM) images obtained by Richard et al. (2003), periodic striations of SDSs covering MWCNTs and SWCNTs were found. The width of the striations attached on the MWCNT was around 4.5 nm (close to the diameter of a hemi-cylindrical micelle in the present study) while the size of the striations on the SWCNT was around 1.5 nm, which is a good approximation of the parallel aggregation. Richard et al. (2003) reported that the concentrations for SDS and CNT were the same for both SWCNT and MWCNT samples. The theoretical surface area of MWCNTs is about 3-6 times (calculated based on a (8, 8) double wall CNT and a (22, 22) four wall CNT) smaller than the same mass of SWCNTs. Therefore, if a stable hemi-cylindrical aggregation is dominant in a MWCNT-SDS dispersion, which means that the surfactant surface density is around 3.4-7.4 molecules/nm^2 based on the present simulation, under the same CNT/SDS concentration, the surfactant surface density of SWCNT-SDS dispersion is very likely lie between 0.8-1.6 molecules/nm^2, which is in good agreement with the proposed range for parallel aggregation.

Like SDS, SDBS-2 has a relatively linear molecular structure with the head group close to the end of the alkyl chain. Thus, the energy-preferred morphology for SDBS-

2 also shifts from parallel to hemi-cylindrical and then to cylindrical as the surface density of the SDBS-2 increases (Figure 3.3-b). However, the results show that SDBS-2 has higher saturation surface density (11.4 molecules/nm^2) which may be caused by the extra attraction induced by the additional atoms in the benzene ring. The saturation surface density of SDBS-2 given here is consistent with the optimum surface density that gave the best dispersion of SWCNT, reported by (Blanch, Lenehan et al. 2010) (7-12 molecules/nm^2 as converted from concentration). Also, experimental study has shown that the optimum SWCNT-surfactant ratio was between 1:5 to 1:10 (converted surface density: 7 to 13 molecules/nm^2) for a series of surfactants including SDS, SDBS, SOBS and SBBS (Islam, Rojas et al. 2003), which matches with the present predicted saturation surface density (11.4 molecules/nm^2).

In contrast, SC behaved quite differently (Figure 3.3-c) from SDS and SDBS. SDS and SDBS show smooth transitions between the hemi-cylindrical and cylindrical aggregation in terms of interaction energy, whereas the maximum interaction energy produced by the hemi-cylindrically aggregated SC is only around 60 % of that of the cylindrical aggregation. This indicates that the hemi-cylindrical aggregation is less energy-preferred for SC, due to the absence of the flexible hydrophobic chain that fitted surfactants more effectively in the space in the centre of the hemi-cylinder. The present results indicate that the energy-preferred morphology of SC assembly on SWCNT probably transited directly from parallel aggregation to cylindrical aggregation at a surface density around 4.3 and saturated at around 6.3.

3.3.2. INTERACTION ENERGY AND DISPERSION CAPABILITY

The calculated interaction energy can be a useful tool for comparing the dispersion efficacy of different surfactants. To find the correlation between this study and experimental data, the present result was compared with that of (Tan and Resasco

2005), where the dispersion efficacy of different surfactants including SC, SDS and SDBS was characterized by the resonance ratio under UV spectroscopy. In their experimental study, (Tan and Resasco 2005) proposed the resonance ratio, which is the ratio of the resonant band area to its nonresonant background in the UV spectrum, as a semi-quantitative criterion of dispersion efficacy of surfactants. Their results are appropriate for comparison because in their experiment they used a CNT sample containing a high weight fraction of (6, 5) SWCNTs (with a diameter equal to 0.7 nm) which had a comparable diameter to that of the (10, 10) SWCNTs (with a diameter equal to 1.3 nm) used in the present simulation.

The surface density (converted from concentration) of the SDBS, SDS and SC based dispersion samples in the Tan and Resasco (2005) experiment are shown in Table 3.2. According to this table, in all samples except for SDBS (1g/L), the surfactant aggregations are defined as saturated since the surface densities are higher than the saturation surface densities suggested by Figure 3.3 (around 9.3 molecules/nm^2 for SDS, 11.4 molecules/nm^2 for SDBS and 6.3 molecules/nm^2 for SC). The interaction energy for the saturated samples was taken as the value at these saturation surface densities. For SDBS (1g/L), the calculated surface density (6.57 molecules/nm^2) was within the range where hemi-cylindrical aggregation is the most stable morphology, as shown in Figure 3.3-b.

Table 3.2 Comparison between the resonance ratio (Tan and Resasco 2005) of (6,5) SWCNT dispersed using different surfactants and the interaction energy between (10,10) SWCNT and these surfactants. In the table, R is the surfactant-CNT mass ratio and S is the surface density calculated based on R. The brackets next to the value of S indicate the type of preferred morphology suggested in Figure 3.3. The resonance ratio of SDBS at different concentrations is compared with interaction energy of SDBS-2 in the present simulation.

Surfactant	R	S, molecules/nm^2
SDS	50	79.4(saturated)
SDBS (1g/L)	5	6.6(hemi-cylindrical)
SDBS (5g/L)	25	32.9 (saturated)
SDBS (10g/L)	50	65.7 (saturated)
SC	100	106.4 (saturated)

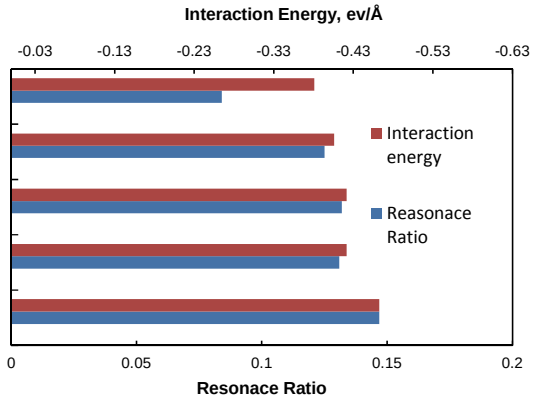

The resonance ratio reported by Tan and Resasco (2005) and the interaction energy are presented as bars next to each sample. As shown in Table 3.2, at saturation surface density, the resonance ratio decreased in the order SC, SDBS, SDS, and a similar trend was shown for the interaction energy in the present simulation. It is also clear that there is only negligible difference between the resonance ratio of SDBS (5g/L) and SDBS (10g/L). Calculation confirmed that at these two concentrations, the SDBS aggregation on the SWCNTs was saturated so that they had similar dispersion capability. Moreover, both the present simulation and the results of Tan and Resasco showed lower dispersion capability when the concentration of SDBS further decreased to 1g/L because the surface density dropped below the saturation level.

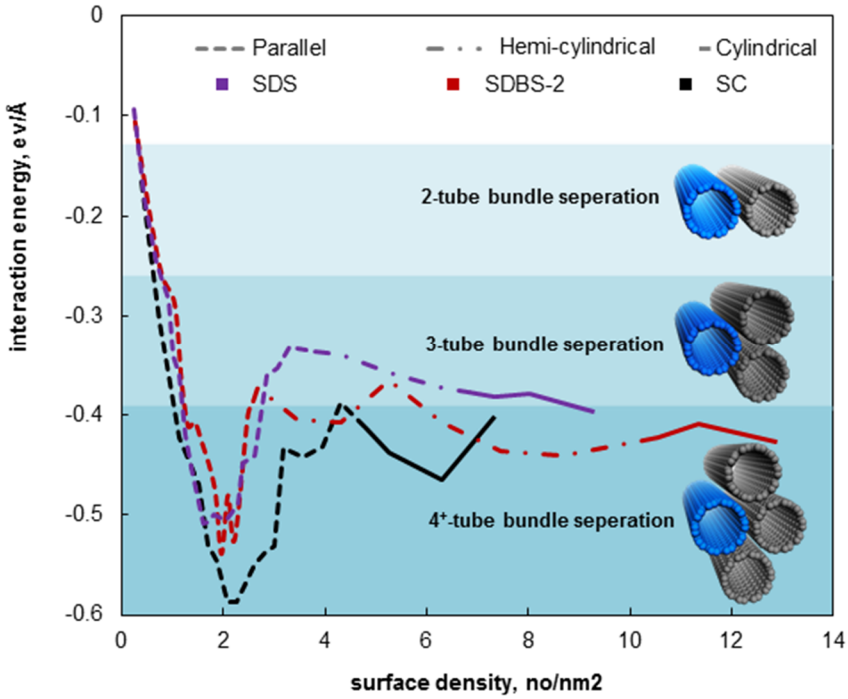

Figure 3.4 Interaction energy curves of SDS, SDBS-2 and SC compared with the interaction energy between a (10, 10) SWCNT and surrounding (10, 10) SWCNTs in a bundle. In the shaded zones, the separation of a particular type of bundle is energetically feasible. The tube-tube interaction increases no more when the number of tubes per bundle exceeds 4 (Duan, Wang et al. 2011). For clarity, curves are shown only for the optimum morphology at different surface density ranges.

Interaction energy curves can also be used to determine whether a surfactant has the potential to provide a stable dispersion of SWCNTs at a certain surface density. Figure 3.4 compares the surfactant-SWCNT interaction energy curves with the interaction energy between bundled SWCNTs (calculated based on the method given by (Duan, Wang et al. 2011)). According to Figure 3.4, energetic barriers can be provided by the surfactants for the 2-tube-bundle and 3-tube-bundle formations when the surface density of the three surfactants exceeds around 2.0 molecules/nm^2. However, a much higher surface density is required to prevent the formation of 4-tube bundles. In the saturated state, the interaction energy of SWCNT wrapped in a SDS aggregation (-0.38 eV/ Å) was similar to that in a 4-tube bundle (-0.39 eV/ Å). This explains the fact that the reaggregation of SWCNTs in SDS solution after ultrasonication (Eda, Fanchini et al. 2008). In contrast, SDBS and SC showed stable

dispersion for a relatively long period after ultrasonication (Blanch, Lenehan et al. 2010) as their saturated interaction energy was obviously higher (-0.41 eV/ Å for SDBS-2 and -0.46 eV/ Å for SC) than the 4-tube bundling interaction energy. As shown in Figure 3.3, both the peak interaction energy of the parallel aggregation and the saturation interaction energy decreased in the order SC, SDBS, SDS.

It is notable that the parallel aggregated surfactants could produce adequate interaction energy to overcome 4-tube bundling within only a very short surface density range (only around 1.7 surfactants / nm^2). In a more realistic aqueous condition, it can be extremely difficult to ensure that surfactant coverage is within this range for every individual tube, due to thermal oscillation (Duque, Densmore et al. 2010), solvent effect (Backes, Englert et al. 2010), and the optimization of surfactant-surfactant interaction (Tummala and Striolo 2009). It is also difficult to obtain full coverage of parallel aggregation (Arnold, Suntivich et al. 2008, Calvaresi, Dallavalle et al. 2009, Lin and Blankschtein 2010) under these conditions. Therefore, much of the experimental success in dispersion of CNTs has been based on the use of surfactants at a surface density beyond saturation (Islam, Rojas et al. 2003, Tan and Resasco 2005, Blanch, Lenehan et al. 2010). However, if the surfactant is designed in such a way that parallel aggregation is the saturation state, higher dispersion power can be obtained.

3.3.3. THE EFFECT OF ALKYL CHAIN LENGTH

The present study suggests that interaction energy is significantly affected by the hydrocarbon chain length, as shown in Figure 3.5. In terms of parallel aggregation, the peak interaction energy decreases when the number of carbon in the chain is reduced from 12 to 8. This is probably because longer chains can improve surfactant energetics

(Islam, Rojas et al. 2003) by allowing more compact packing between the CH_3 ends of the surfactant and the SWCNT surface. The surface density corresponding to the peaks increases from 1.83 molecules/nm^2 for SDBS-2 to 4.50 molecules/nm^2 for SBBS-2 as a result of the reduced size of the surfactants, as shown in Figure 3.1. In contrast, the saturation density drops in the order SDBS-2 (11.4 molecules/nm^2), SOBS-2 (9.3 molecules/nm^2), SBBS-2 (8.0 molecules/nm^2) because the short chain corresponds to a smaller radius and less space between the head groups. Interestingly, for interaction energy at saturation and the peak of parallel aggregation, SDBS-2 showed higher interaction energy than SBOS-2 and SBBS-2, which is consistent with the dispersion ability demonstrated in the study of Islam et al. (2003). However, SBBS-2 showed similar interaction energy to that of SOBS-2 at the peak of the parallel aggregation (-0.450 ev/Å compared to -0.445 ev/Å) and similar saturation (-0.387 ev/Å compared to -0.381 ev/Å). These similar values of interaction energy may have the following causes. For the parallel aggregation, SBBS-2 attaches to the SWCNT surface less firmly than SOBS-2, due to the shorter chain, but has a higher proportion of benzene rings and therefore a higher number of carbon atoms per nm^2 SWCNT surface. For the cylindrical morphology, the atoms in the surfactants interact effectively with the SWCNT within only a very short range (within a cut-off distance of 9.5 Å) and the SBBS-2 has the benzene ring lying within this range whereas the SOBS-2 does not. Thus, although the saturation surface density for SBBS-2 is lower, one vertically attached SBBS-2 has more carbon atoms (around 10) within this range compared to SOBS-2 (around 6).

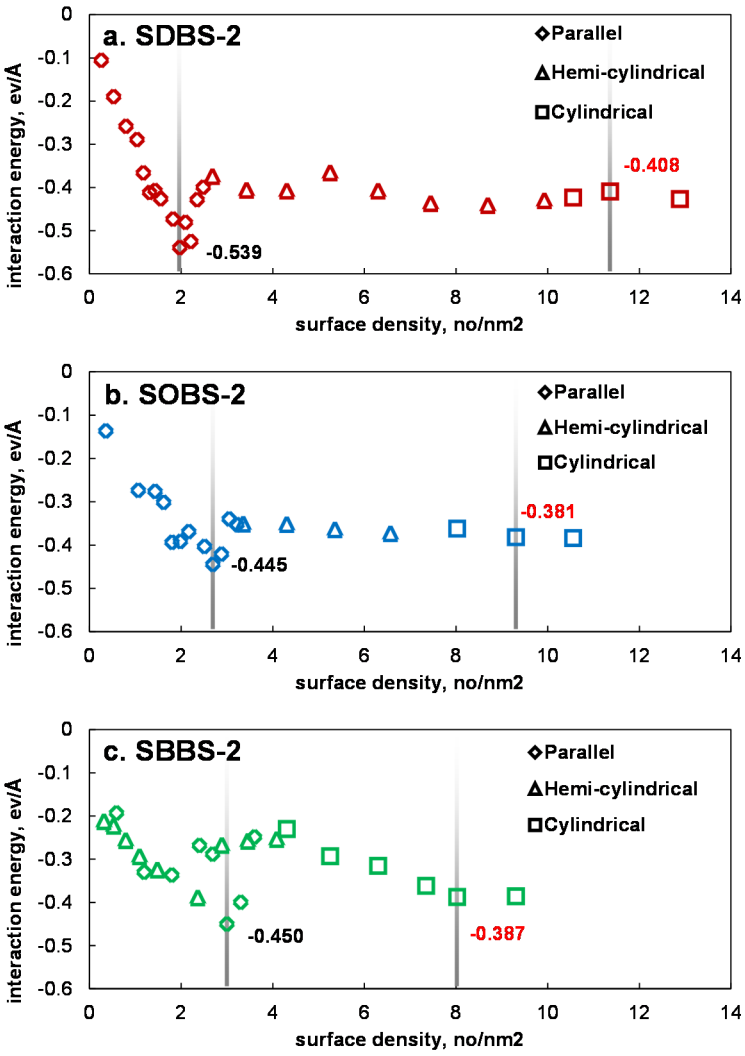

Figure 3.5 Interaction energy curves for SDBS-2, SOBS-2 and SBBS-2. Interaction energy is only plotted for the optimum morphology (the morphology that gives the most negative interaction energy) at a certain surface density. For SBBS-2, both parallel and hemi-cylindrical are plotted since there is no clear preference between the two. The positions and the interaction energy values are marked on the graphs at the peak of parallel aggregation (black numbers) and at the saturation surface density (red numbers).

Furthermore, a shortened hydrocarbon chain may also affect the energetic preference in morphologies. When the chain is shortened to a certain level its bending rigidity become compatible with the benzene ring, making the surfactant behave like

beads rather than structures with flexible tails. As a result, the preferred aggregation morphology between parallel and hemi-cylindrical morphologies for SBBS-2 at surface density lower than 5 molecules/nm^2 cannot be explicitly defined, which implies that maybe a random morphology (Yurekli, Mitchell et al. 2004) is more suitable for describing the aggregation of SBBS-2 in this surface density range. However, cylindrically aggregated SBBS-2 still show higher interaction energy and a stable morphology at surface density near saturation (around 6.3 molecules/nm^2). This finding is consistent with TEM observations of surfactant aggregation on graphite surface where surfactants with short chains were found incapable of forming hemi-cylindrical aggregation (Atkin, Craig et al. 2003).

3.3.4. THE EFFECT OF HYDROPHILIC GROUP POSITION

Figure 3.6 indicates that the position of the hydrophilic group on the hydrocarbon chain affects the interaction energy and preference for aggregation morphology. The interaction energy at saturation and the peak of parallel aggregation decrease in the order SDBS-2, SDBS-3, SDBS-6, suggesting that SDBS isomers with a hydrophilic group near the end can achieve stronger binding with SWCNTs. This is probably because the head groups closer to the middle of chain make it more difficult for the SDBSs to aggregate firmly. This trend is in accordance with a study of sodium alkyl benzene sulphonate (SABS) aggregating at an air/water interface where SABS with a benzene ring near the end of the alkyl chain formed denser aggregation (He, Guvench et al. 2010). Also, the increased solubility of SDBS as the hydrophilic group moves towards the middle (Ma, Boyd et al. 2006) implied decreased bonding strength between SDBSs in water. As shown in the present study, the SDBS-6 cylindrical

aggregation, with considerably lower saturation surface density (5.2 molecues/nm^2), required more space than the other two isomers.

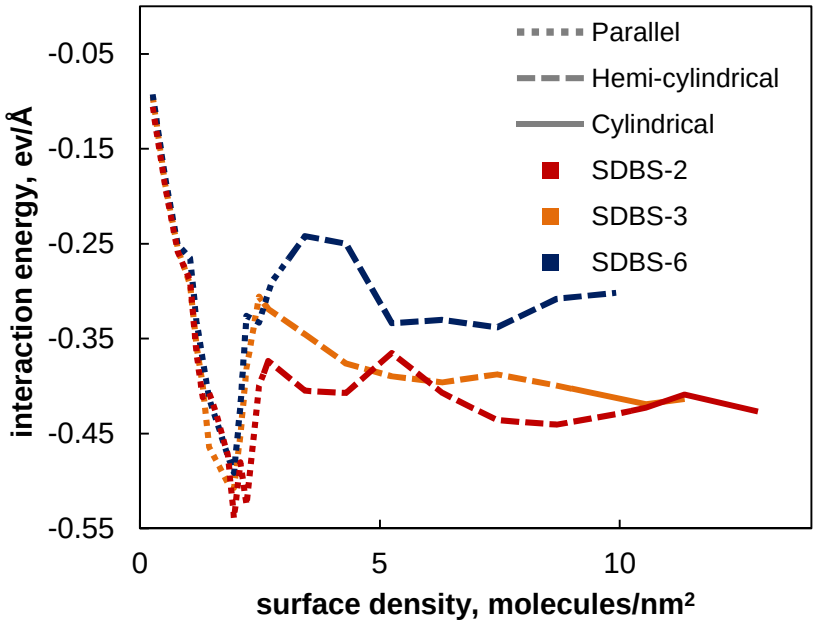

Figure 3.6 Interaction energy curves for SBDS-2, SDBS-3 and SBDS-6. For clarity, only the energy-preferred morphologies are presented.

SDBS-6 also showed less energetic preference for the cylindrical aggregation, as the interaction energy of cylindrical aggregation is constantly lower than that of the hemi-cylindrical aggregation (Figure 3.6). The reason for this phenomenon may be that with the hydrophilic group closer to the middle, the alkyl chains tend to orient at a greater tilt angle (the angle to the normal of the CNT surface), as they did on an air/water interface (He, Guvench et al. 2010). Since the average tilt angle is greater in hemi-cylindrical aggregation than in cylindrical aggregation, SDBS-6 showed a preference for hemi-cylindrical aggregation at saturation.

3.4. Conclusions

The interaction energy between surfactant and CNTs is proved able to reflect differences in aggregation morphology. The effect of molecular structures on interaction energy and the energy preference for morphologies at different surfactant surface densities were investigated via MM simulations.

The energy preference for aggregation morphologies against increasing surface density were found to follow a parallel/hemi-cylindrical/cylindrical pattern for surfactants with relative long linear hydrocarbon tails and hydrophilic groups at the two ends (SDS, SDBS-2, SDBS-3 and SOBS-2). Surfactants with short chains, mid-position head group and planar structure, on the other hand, showed direct transitions from parallel (SC, SDBS-6) or random (SBBS-2) to hemi-cylindrical (SDBS-6) or cylindrical (SC, SBBS-2) aggregation. Discrepancies in the molecular structure of surfactants, which influenced the dispersion efficacy of CNT in experimental studies, also had a consistent impact on the interaction energy.

The results in this section serve as guidance for selecting appropriate surfactants for dispersion of CNTs. It is suggested that surfactants with (1) long hydrocarbon chain, (2) non-linear structure (e.g. multiple chain branches or planar structure) and (3) hydrophilic groups near the end of flexible chains will perform the best for dispersion purposes.

Fortunately, some cement additives, such as polycarboxylate and lignosulfonate based superplasticizer, possess these molecular characteristics and therefore have potential for dispersing CNTs. In the next section, some cement additives are used to disperse CNTs in a Ca^{2+} based alkaline environment. The stability and agglomeration processes of the cement additive-CNT dispersion are investigated.

CHAPTER 4. STABILITY AND AGGLOMERATION PROCESS OF MWCNTS IN ALKALINE ENVIRONMENT

4.1. Introduction

An alkaline environment plays an important role in the fabrication of CNT-OPC pastes (Li and Sagues 2001, Moreno, Morris et al. 2004, Tang, Miao et al. 2012). Although a considerable number of studies have focused on the dispersion of SWCNTs (Islam, Rojas et al. 2003, Tan and Resasco 2005, Blanch, Lenehan et al. 2010) and MWCNTs (Yu, Grossiord et al. 2007, Bai, Park et al. 2011, Tiwari, Sagar et al. 2012) using various surfactants in an aqueous environment, the number of dispersion studies involving highly alkaline (pH > 12) environments is limited, especially for $CaOH_2$ introduced alkalinity. Past research has shown that the performance of some commonly used surfactants such as SDS and SDBS or deteriorates with elevated pH value (Sun, Gao et al. 2002, Matarredona, Rhoads et al. 2003, Moore, Strano et al. 2003, White, Banerjee et al. 2007).

Cement additives with surfactant-like molecular structures, which are designed for highly alkaline environments with Ca^{2+} and OH^- ions, have shown promising potential as CNT dispersions in alkaline environments. In the work of Makar (2011), the dispersion of SWCNTs in different cement admixtures was investigated, and poly-naphthalene sulphonate sodium salt (a type of superplasticizer) was found to achieve effective dispersion of SWCNTs. Collins and his group also studied the dispersion of MWCNTs in water using several cement compatible surfactants (Collins, Lambert et al. 2012). Although these studies demonstrated positive dispersion effects using

cement additives as cement compatible surfactants, no quantification of the CNT dispersion in alkaline environment was conducted.

This chapter focuses on the dispersion of MWCNTs using three commercially available cement additives (cement-compatible surfactants) in saturated $CaOH_2$ solution. Saturated $CaOH_2$ solution is commonly used as simulated cement pore solution and it is suitable for visual observation, UV-vis measurement and MD simulation of dispersion of CNTs.

Two main topics are investigated in this chapter, namely (1) the stability of the CNT dispersion and (2) the agglomeration process of CNTs. The stability of CNT dispersion is quantified using UV-vis spectrometry and Zeta-potential measurements, and the agglomeration process is studied via TEM imaging and hydrodynamic size analysis.

To achieve better understanding of the agglomeration process of CNTs, MD simulation is conducted for the $CaOH_2$-surfactant-MWCNT system. The self-energy (Israelachvili 2011) of CNT wrapped surfactants is calculated and it is proposed as a parameter that can be used to compare the dispersion efficacy of different surfactants.

With the calculated self-energy, a theoretical model is developed to simulate the agglomeration process of CNT bundle development. The model is used to study the agglomerating behaviour of CNTs.

4.2. Experimental program

4.2.1. MATERIALS

The MWCNTs used in this study were purchased from Shenzhen Nanotech Port Co. Ltd (Shenzhen, China). This non-functional MWCNTs are used here to study the fundamental thermaldynamics principles of CNTs agglomeration in aqueous environment. In the latter experiments, –COOH functionalised MWCNTs is used to

improve the dispersion and the reinforcing effect of CNTs. The properties of the MWCNTs are given in Table 4.1. Three types of commercial cement additive were used. The brands and properties of these surfactants are shown in Table 4.2. Since the alkyl chain in MA varies only slightly from 10-14, for simplicity, dodecyl-benzene sulfonic acid (DBSA) was used to represent the surfactant in MA.

Table 4.1. Properties of the multi-walled CNTs

Outer Diameter	Length	Purity	Specific Surface Area
10~20 nm	5~15 nm	>97 %	90~120 m^2/g

Table 4.2. Cement additives used and the surfactants contained (Grace 2007, Chemwatch 2008, Chemwatch 2009).

	Micro Air® 905 (MA)	Rheobuild®716LR (716LR)	WRDA® GWA (WRDA)
Surfactant contained	Alkyl-benzenesulfonic acid (C = 10-14) (DBSA)	Naphthalene-sulfonic acid/formaldehyde calcium salt, CAS: 37293-74-6 (NC)	Modified sodium lignosulfonate (SL)
Concentration of surfactant	10 %	60 %	50 %

4.2.2. DISPERSION OF CNTS IN ALKALINE SOLUTIONS

$CaOH_2$ was added into distilled water to produce an aqueous environment with stable pH ≈ 12.5. The amount added was 5 times the solvable amount to ensure that the solution was saturated. Saturated $CaOH_2$ solution is a commonly used simulated concrete pore solution (Li and Sagues 2001, Moreno, Morris et al. 2004, Tang, Miao et al. 2012). MWCNT and surfactants were added into the alkaline aqueous solution

and sonicated with a 100W ultrasonicator with a 5" tip operating at 25 % intensity. Research has shown that different CNT products may require different UE to reach the maximum dispersion, but generally input energy intensity around 690 J/ml solution or 9.6 MJ/g of CNT is sufficient (Krause, Mende et al. 2010). The total volume of each sample was 20 ml and the ultrasonication time was 10 minutes (the corresponding input UE is around 750J/ml). The concentration of the CNT adopted was 0.1 wt % and 0.5 wt % of surfactant was used. The surfactant to CNT mass ratio was 5 in this case. A study has shown that SDBS reaches the maximum dispersion of MWCNT when the surfactant to CNT ratio is greater than 1.5 to 4 (Yu, Grossiord et al. 2007). Dispersion study of Gemini imidazolium surfactants also showed that the dispersion of CNT reached a maximum level at the surfactant to MWCNT mass ratio of 1 to 4 and only minor decrease of dispersion efficacy was observed when this ratio was increased from 4 to 8 (Liu, Yu et al. 2010). Therefore, adoption of a surfactant to CNT ratio of 5 should give, if not the optimal, reasonably good dispersion for all the surfactants used in this case. The actual pH value of the solutions was tested by a pH meter after ultrasonication. The pH values of the solution were 12.83 for MA, 12.82 for 716LR and 12.69 for WRDA.

4.2.3. UV AND TEM CHARACTERIZATION

The settling of the agglomerated MWCNTs was captured using a digital camera and examined. Since some of the dispersants were yellow or brown in colour, $CaOH_2$ saturated solutions with the same concentration of surfactants were used as reference during comparisons. NC and SL absorb UV light very strongly in the range between 200 nm and 400 nm, which limited the concentration of MWCNTs that could be used in the UV-vis samples. The sampled MWCNT suspensions and reference solutions were therefore diluted by a factor of 100 and then analysed using a HACH® DR5000

UV-vis spectrometer. The ABS between 190-1100 nm was recorded. To observe the morphology of CNT bundles during CNT agglomeration, TEM was utilized. To prepare TEM samples, the CNT suspensions were diluted in distilled water 20 times, and then a droplet of the CNT-NC and CNT-SL suspension was pipetted onto a 400 mesh holey-carbon-coated copper grid. After water evaporation, the samples were examined using a JEOL 2100F FEG TEM electron microscope operated at an accelerating voltage of 200 kV. TEM images were randomly taken in an area near the centre of the TEM grid. For each sample, around 15 images were taken and more than 370 MWCNT bundles were measured using a grid-based method.

This grid-based measuring method is demonstrated in Figure 4.1. Horizontal lines and vertical lines with a spacing of 200 nm are drawn across the TEM images. CNT and CNT bundles intersecting each line with an angle greater than 45 degrees are identified (as demonstrated between the red lines in Figure 4.1) and the number of tubes in that bundle is measured and recorded (shown as numbers in Figure 4.1). Counting bundles with intersecting angle greater than 45 degrees avoids repeated measurement of bundles that intersect both horizontal and vertical grid lines. This intersecting angle is defined as 0 when a bundle is parallel to a grid line and 90 when a bundle is perpendicular to a grid line.

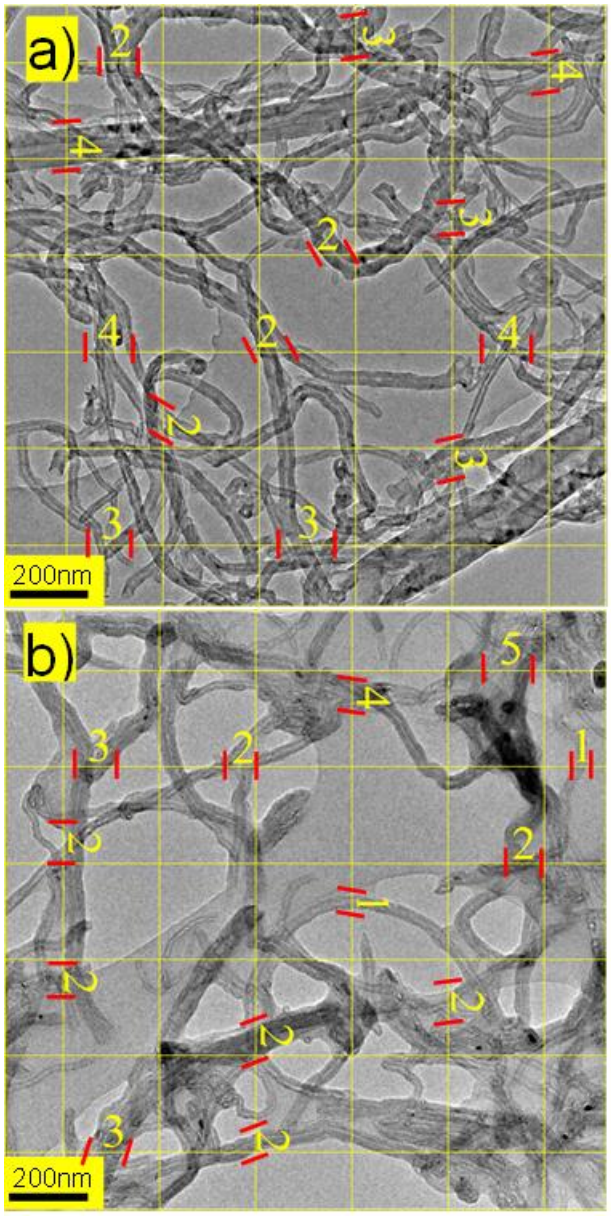

Figure 4.1. TEM images of CNT agglomerates in NC-based (a) and SL-based (b) suspension and examples of the measurement of the bundle size of CNTs intersecting the grid. The meauresments are shown as yellow numbers between two red lines which indicate the measuring boundary of the bundle. Several measurements are shown for clarity.

4.2.4. ZETA POTENTIAL AND HYDRO DYNAMIC SIZE

To determine the hydrodynamic size and the zeta potential of CNTs in suspensions, a ZetaSizer Nano ZS (Malvern Instrument Ltd., UK) instrument which used dynamic light scattering was used. All CNT suspensions were equilibrated at a temperature of

25°C for 2 mins before measurements. The size measurement range was adjusted from 3 nm to 6000 nm. To check the reproducibility of the hydrodynamic size and zeta potential values, three sets of measurements were taken for each sample and the mean of the three experiments and resultant standard deviation were then reported.

4.3. MD simulations

MD simulation was conducted using Materials Studio 5.5. COMPASS force field was used with an atom-based simulation method for vdW force (cut-off distance: 9.5 Å) and the Ewald summation method (Ewald accuracy: 0.1 Kcal / mol) for electrostatic forces. Since in this experiment, DBSA was proved to be incapable of forming dispersed MWCNTs suspensions in the alkaline environment provided, only NC- and SL-CNT suspensions were simulated and studied. Figure 4.2 shows the molecular structures of the surfactants used in the simulation. To maintain consistency within the experiments, where the adsorption of surfactants was near saturation at the MWCNT surface, in the MD simulation the surfactants were packed as densely as possible in the transverse direction of the CNT.

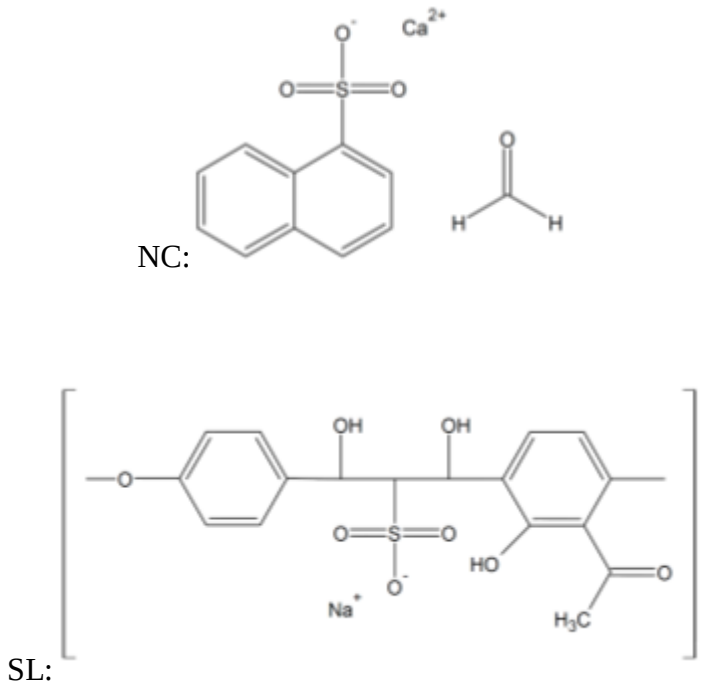

Figure 4.2. Molecular structures of the surfactants used in the simulation.
(Ramachandran 1995, ChemicalTradingGuide 2012)

To characterized this repulsive force with MD simulation, usually a pair of CNTs are simulated and the potential of mean force is calculated (Lin and Blankschtein 2010, Tummala, Morrow et al. 2010, Xu, Yang et al. 2010, Uddin, Capaldi et al. 2011). However, it is impractical to conduct atomic level MD simulation on the interaction between a pair of 10 nm MWCNTs, due to the large number of particles in the system. Therefore, two cases were simulated where NCs and a SL containing 5 repeat units were attached on (100, 100) triple-walled CNT surfaces (Figure 4.11). Since it was too expensive to simulate the whole perimeter of the (100, 100) CNT, only a section of the tube consisting of 10 aromatic rings in the circumferential direction was simulated.

The simulation comprised two steps. In the first step, which was conducted before the packing of the solution molecules, the initial configurations of the CNT-surfactant

complex were generated using the following procedures. First, a set of an infinite graphene network was built, spanning over a periodic simulation box. This graphene network contained 3 layers, each of which was a section (1/10) of a (100,100) SWCNT (Figure 4.11). The size of the simulation box was 21.2×200×24.6 Å box with centre symmetric configuration in the 200 Å direction. Then the surfactants were placed in a radially symmetric pattern around the CNTs with the hydrophilic groups facing outwards.

For NC and SL, parallel aggregation was used, allowing the hydrophilic groups to be in contact with the solution. The surface density, which was the number of surfactants attached per nm^2 of CNT surface, was gradually increased and the forces in the system were minimized. The interaction energy between the CNT and surfactants was calculated. This interaction energy increased with the surface density until it reached a threshold where adding more surfactants overcrowded the surface, resulting in decreased interaction energy. The surface density at that point was considered the starting point for the next step. This approximate saturation surface density could be slightly higher in the MD due to the thermal oscillation and the solvent effect. However, using such configurations allowed the system to reach saturation state easily in the MD simulation.

The second step began with packing the space with water, Ca^{2+} and OH^- to make the pH value approximately equal to 12.5 and the density around 1 g/ml. For NC, formaldehyde was also packed into the space. Geometry minimization was then conducted, followed by a 90 ps NVT within which the self-energy of the CNT was stabilized. Then the structures were saved every 0.5 ps in successive 10 ps NVT for analysis. The interaction energy between the CNT-surface and all surrounding molecules was calculated using the method from a previous publication (Duan, Wang

et al. 2011). The average interaction energy was calculated for the analysis period and is used for this discussion.

Simulation was also conducted to calculate the CNT-CNT interaction energy for the (100,100) triple-walled CNTs. Two (100,100) triple-walled CNTs were built in free space, intersecting at their mid-length with a minimum atom-to-atom distance of 0.34 nm. The interaction energy between these two tubes was calculated using the method from previous publication (Duan, Wang et al. 2011). The interaction energy for five different intersecting angles was computed, namely 0, 22.5, 45, 67.5 and 90 degrees, where 90 degrees corresponded to the case in which the two tubes were perpendicular.

4.4. Results and discussion

4.4.1. STABILITY OF DISPERSION

Figure 4.3 shows the settling of MWCNTs in different dispersant solutions after ultrasonication ceased. It can be clearly seen that MWCNTs in the DBSA-CNT suspension form visible agglomeration just 1 hour after ultrasonication. These agglomerated MWCNTs settl rapidly, resulting in a clear top solution within 24 hours. The NC- and SL-CNT suspensions at 1 hour and 2.5 hours both appear as uniformly black solution. After 24 hours, the SL solution shows no change in the uniformity of colour whereas the NC solution showed stratification. These visual observations qualitatively indicate that the suspended mass of the MWCNTs in the upper part of the solution decreases in the order SL, NC, DBSA. It was noted that the suspended mass of MWCNTs consisted of individual CNTs and CNTs bundles of various sizes (Islam, Rojas et al. 2003).

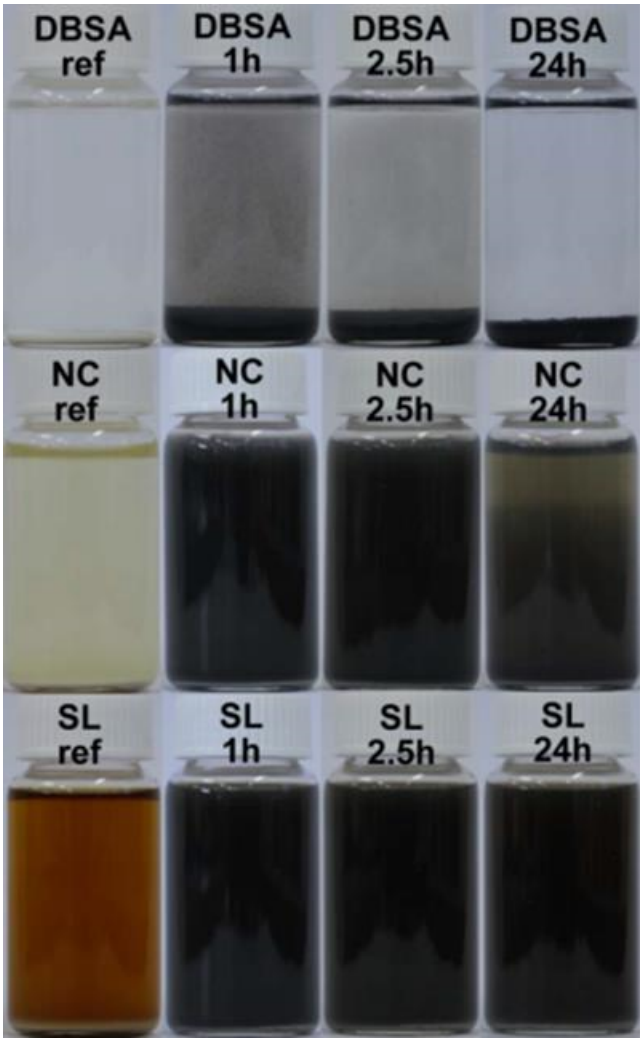

Figure 4.3. CNT-surfactant alkaline suspension taken at 1 hour, 2.5 hours and 24 hours after ultrasonication. For comparison, the reference solutions without CNTs are also presented (annotated “ref”).

The amount of highly dispersed MWCNTs in the form of individual or small bundles can usually be characterized using their UV-vis spectra. UV-vis spectra were recorded for the DBSA-, NC- and SL-MWCNT dispersions at the three different standing times, that is, 1 hour, 2.5 hours and 24 hours. As an example, Figure 4.4 (top) shows the absorbance (ABS) between 400 and 800 nm measured from samples taken from the DBSA-, NC- and SL-CNT solutions 1 hour after ultrasonication. NC and SL are found to have very strong ABS when the wavelength is less than 400 nm, therefore

the spectra with lower wavelength than 400nm were not used to characterize the amount of CNTs. The corresponding reference solutions (with surfactants and $CaOH_2$ only) were used as baselines for the curves presented in Figure 4.4.

As clearly indicated in Figure 4.4-a, the ABS of MWCNT is mostly undetectable in the DBSA sample. Although the MWCNTs in the DBSA (1h) suspension does not precipitate completely in Figure 4.4, the low ABS suggests that these suspended MWCNTs are in the form of large agglomerations which are not sensitive in terms of UV-vis ABS. Compared with the flocculation of SWCNTs observed in a sodium dodecylbenzenesulfonate (a surfactant with similar molecular structure to DBSA) assisted aqueous dispersion under basic conditions (Moore, Strano et al. 2003), the present results attest that the DBSA-MWCNT system is also unstable under high alkalinity while the sediment appears as a denser solid rather than flocculation (Moore, Strano et al. 2003).

Considering the scant dispersion efficacy of DBSA in a highly alkaline environment, the following discussion mainly compares SL with NC. After 1 hour of storage, NC and SL have similar ABS curves in Figure 4.4-a. Both surfactants are able to suspend small MWCNT bundles that are sensitive to UV-vis light, but the SL appeared more efficient with higher ABS. The ABS from NC and SL suspended MWCNTs at 600 nm (Liu, Yu et al. 2010, Vichchulada, Cauble et al. 2010) are plotted in Figure 4.4-b to show the stability of the dispersed MWCNTs over time. Generally, the results indicate that SL has a higher ABS which implies its superior dispersion efficacy under such condition. However, the ABS for both dispersions decreases almost constantly by more than 70 % within 24 hours. Compared with CNT dispersions at neutral pH, which was stable for weeks (Islam, Rojas et al. 2003), the dispersion in CaOH2 induced high alkalinity is far less stable.

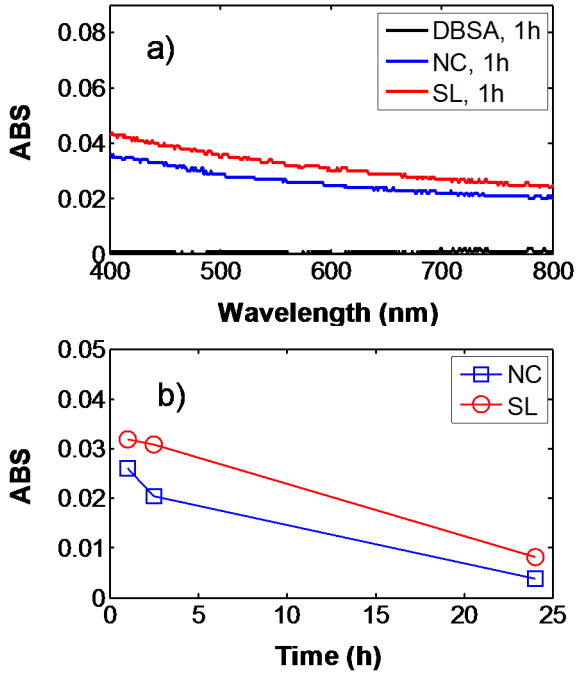

Figure 4.4. (a) UV-vis ABS for samples taken from the different MWCNT dispersions 1 hour after ultrasonication ceased. The reference-subtracted ABS is presented. (b) Average UV-vis ABS between 400 and 800 nm for SL and NC dispersed MWCNT solution at different settling times.

The visual and UV-vis characterization give indications as to the dispersion efficacy of the surfactants under high alkalinity in terms of small MWCNT bundles. SL performs reasonably well in this regard, closely followed by NC, but DBSA is considered incapable of dispersing MWCNTs under such conditions.

The zeta-potential measurements were also used to give an indication of the stability of the MWCNT suspensions. The zeta-potentials of SL-MWCNT and NC-MWCNT solutions as a function of storage time were measured and are presented in Figure 4.5. As shown in Figure 4.5, immediately after ultrasonication the zeta-potentials for both suspensions were nearly neutral, indicating negligible electrostatic

repulsion between suspended particles, which indicates instable dispersion. After 1 hour of storage, with zeta-potentials of 11.7 and 16.3 mv for SL and NC respectively, the suspensions reaches a semi-stable state where the suspended CNTs surrounded by negatively charged surfactants contributes to the negative zeta-potential (Israelachvili 2011). This stabilization of the suspension during the first hour could be a result of the bundling and precipitation of large CNT agglomerates which decreases the concentration of suspended CNTs. Still, the suspension is shown to be incipient instable after 1 hour, indicating that the dispersed CNTs in the solution begin to gradually bundle and form large precipitates. Accordingly, the magnitude of zeta potential decreases due to the detaching of surfactants from the CNTs surface, increasing the ionic strength in bulk solution (Atesok, Somasundaran et al. 1988, Jiang, Oberdörster et al. 2009) and contracting the electrical double layer (Cosgrove 2010).

It is noted that the magnitude of zeta potential for SL was lower than that of NC at 1 and 2.5 hours. The lower zeta potential in the SL-CNT system dose not imply lower dispersion efficiency, as the long chain-like structure of SL (Ramachandran 1995) may produce a stronger steric repulsion force than that of NC. However, as addressed above, the decrease in zeta potential does give an indication of the amount of detaching surfactants and the bundling of CNTs. It is shown in Figure 4.5 that, from 1 hr to 24 hours, the magnitude of zeta potential decreases by 56 % from -16.3 ± (1.7) to -7.1 ± (1.1) in the NC system, whereas the drop in the SL system is only 29 % from -11.7 ± (0.4) to -8.3 ± (1.2). This indicates that more bundling of CNTs occurs in the NC system, which is consistent with the visual observation in Figure 4.3.

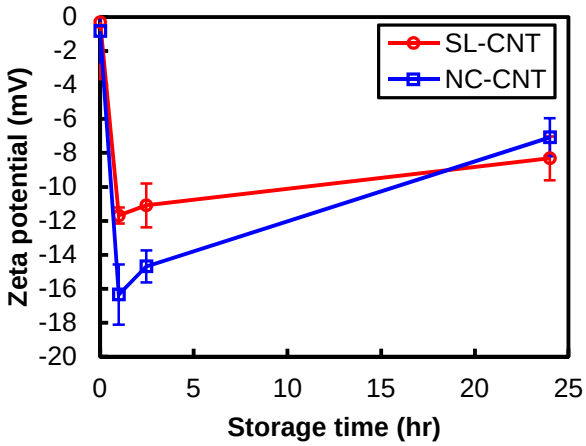

Figure 4.5. Zeta potential of SL-CNT and NC-CNT suspensions as a function of storage time.

The results presented herein corroborate that in strong Ca^{2+} based alkaline environment, the tested surfactant-CNT dispersions are in either an instable or semi-stable state. Understanding of the agglomeration process is important to guide better application of CNTs in highly alkaline environments such as in OPC paste (Cwirzen, Habermehl-Cwirzen et al. 2009, Musso, Tulliani et al. 2009, Konsta-Gdoutos, Metaxa et al. 2010). In sections 4.4.2 to 4.4.4 the bundling behaviour of CNTs in SL and NC systems is investigated.

4.4.2. BUNDLE SIZES OF SUSPENDED CNTS

Figure 4.6 shows the hydrodynamic size distribution of NC and SL-CNT suspensions after different storage times. Immediate after ultrasonication treatment, individual CNTs or small CNT bundles (containing a few CNTs) with uniform hydrodynamic sizes (with a single narrow peak) is observed for both surfactants. From 1 hour onwards, the distributions begin to show peak broadening as well as peak splitting, indicating the progressive bundling of CNTs.

As a result of the peak splitting, the distributions in Figure 4.6 usually contain three different peaks whose positions are presented in Table 4.3. Table 4.3

demonstrates that the positions of the three peaks are within similar ranges for the different surfactants: first peak at around 120 nm-200 nm, second peak at around 700 nm to 900 nm and third peak at size greater than 4000 nm. It can be identified that the third peak corresponds to the large CNT agglomerates and it often extends outside the measurable range of the equipment (5560 nm). It is suggested that the first two peaks correspond to surfactant-dispersed CNTs of hydrodynamic size between about 100nm and 1000nm (Krause, Mende et al. 2010). The first peak could be due to the individual CNTs, with the second peak corresponding to small CNT bundles containing a few CNTs.

The trends in the first two peaks over time were different for the different surfactants. In NC-CNT system, the intensity of the first peak decreased as the period of storage increases, whereas in the SL-CNT system the first peak dropped to very low intensity at 1 hour and then gradually increased. The second peak begin to become prominent after 1 hour as a result of the bundling of individual CNTs but starts to decrease from 2.5 hours to 24 hours, due to the further bundling of CNTs to form large agglomerates. The increase in the first peak in the SL-CNT system can be attributed to the longer chain-likes structure of the SL molecules (Ramachandran 1995) that may result in the trapping of individual CNTs during precipitation of the large agglomerates in the form of soft flocculation (Buffle and Leppard 1995). The trapped individual CNTs will then be released into the suspension due to Brownian motion. Also, the overall intensity of both the first and the second peak for SL is significantly higher than that of NC, which explains the higher UV-vis ABS of the CNTs in the SL system.

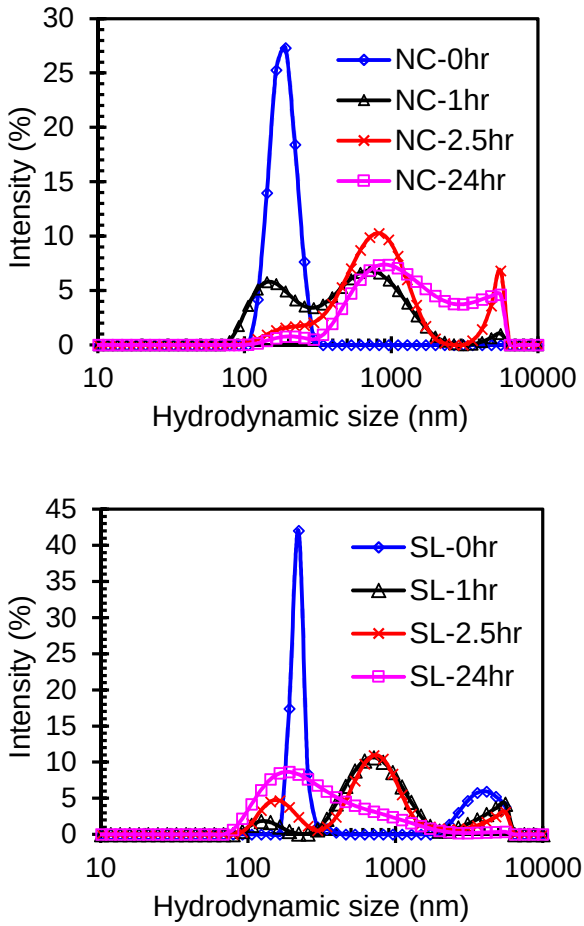

Figure 4.6. Average hydrodynamic size distribution of CNTs in (a) NC-CNT and (b) SL-CNT solutions as a function of storage time.

Table 4.3. Average hydrodynamic size (H_D) of CNTs in the NC-CNT and SL-CNT suspensions as a function of storage time.

NC-CNT	H_D (nm) at Peak 1	H_D (nm) at Peak 2	H_D (nm) at Peak 3
0hr	190.1 ± (12.3)*	-	-
1hr	141.7 ± (0.5)	712.3 ± (0.1)	5559.6 ± (0.3)
2.5hr	164.0 ± (0.5)	824.9 ± (2.9)	5559.6 ± (3.0)
24hr	220.1 ± (1.3)	955.4 ± (0.2)	5559.6 ± (0.7)
SL-CNT			
0hr	220.1 ± (36.4)	-	4145.4 ± (10.3)
1hr	122.42 ± (0.1)	712.3 ± (1.8)	5559.6 ± (1.0)
2.5hr	164.1 ± (3.3)	712.3 ± (4.2)	5559.6 ± (4.3)
24hr	190.1 ± (0.9)	-	-

*Numbers in brackets indicate standard deviation.

Figure 4.1 shows two examples of the TEM images used to quantify the bundle size of the MWCNTs in the NC and SL suspensions. Some examples of the measurement (red lines and numbers) are demonstrates as described in section 4.2.3. It can be seen from Figure 4.1 that the NC suspension contains MWCNTs with generally larger bundles than those in the SL suspension.

Quantitative measurements of bundle size for both suspensions are presented in Figure 4.7. The term 'bundle size' here refers to the number of CNTs that are bonded together in a near-parallel fashion. In terms of the proportion of MWCNTs in a bundle for different bundle sizes, it can be seen that the NC has a broader distribution than the SL, with more MWCNTs in bundles of more than 4 tubes. Indeed, 53 % of MWCNTs in the SL suspension had a bundle size smaller than 2, whereas only 30 % of MWCNTs in NC does. On the other hand, in the NC suspension, around 20 % of the bundles had size greater than 4 whereas a negligible amount of CNTs in the SL suspension are in such large bundles. One should also note that almost no bundles are observed in either suspension with more than 7 tubes.

The results here show that in the two different surfactant-MWCNT systems, different bundle sizes is preferred. In addition, there is an upper size limit for the near-parallel bundling of the MWCNTs. These are important phenomena to be considered when dispersing CNTs in an alkaline environment. In section 4.4.3, a CNT-agglomerating model is proposed and discussed. Combining MD simulations of the interaction between SL/NC and CNT surface with the proposed model, the mechanism behind these observations is explained in section 4.4.4.

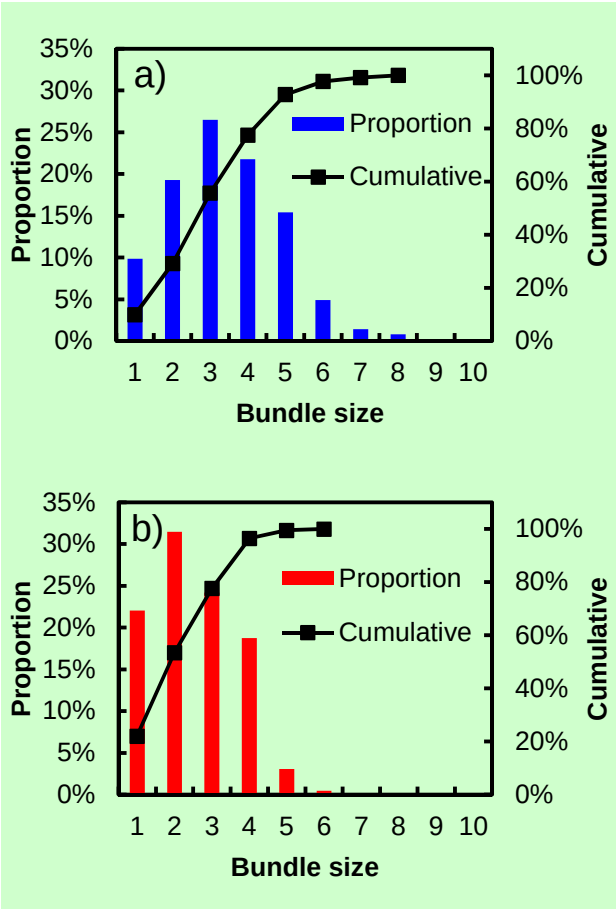

Figure 4.7. Proportion of MWCNTs in bundles of different sizes in NC (a) and SL (b) suspension as measured from TEM images.

4.4.3. PROPOSED AGGLOMERATING MODEL FOR CNTS

4.4.3.1. Parallel Bundling of CNTs

Figure 4.8-a illustrates an idealized model that presents one possible way for a CNT parallel bundle to grow bigger (Peigney, Laurent et al. 2001). In this idealized model, it is assumed that each time only one tube is added to the bundle and all tubes are parallel with an identical diameter. The central tube (tube 1 in Figure 4.8-a) will first attract another 6 tubes to form the first shell layer surrounding itself (tubes 2-7), then a second shell layer with 12 tubes (tubes 8-19), and so on. With this defined order of growth, the surface area of the bundle is kept to a minimum. The average self-energy of individual tubes in a parallel bundle μ_N equals to the sum of self-energy (of all the

tubes in the bundle) S divided by the number of tubes in that bundle N (Israelachvili 2011).

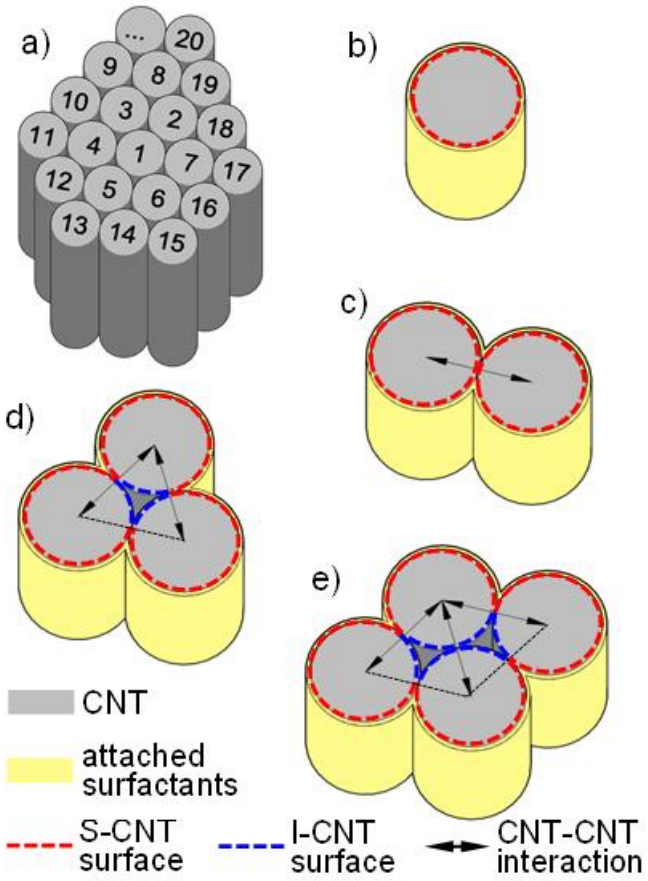

Figure 4.8. Schematics of an idealized CNT bundle growth model. a) A growing CNT bundle with a hexagonal shape and CNTs attaching to the bundle in the sequence indicated by the numbers (1-20...). b) A single tube in solution. c) Situation 1: a tube attaches to another tube. Arrows indicate the formation of tube-tube vdW interaction. d) Situation 2: a tube attaches to two bundled tubes. e) Situation 3: a tube attaches to three bundled tubes. S-CNT surface: CNT surfaces in contact with surfactants and solution. I-CNT surface: CNT surfaces that are isolated from surfactants and solution.

When a single CNT is attached to an existing CNT bundle, there are only three possible situations, as shown in Figure 4.8-c to e. The change in the sum of self-energy ΔS is different for these three situations and is given as

$$\Delta S = 2I_t + I_s, \text{ situation 1} \quad 4.1$$

$$\Delta S = 4I_t + \frac{1}{2}I_s, \text{ situation 2} \quad 4.2$$

$$\Delta S = 6I_t - I_s, \text{ situation 3} \quad 4.3$$

where I_t is the interaction energy between two CNTs, I_s is the interaction energy between an individually dispersed CNT and the surrounding surfactants and solution (Figure 8-b).

The simulations are illustrated in Figure 4.8-c to e. In situation 1, where one tube is attached to another, one pair of tube-tube interaction ($2I_t$) is introduced and the surface area of the bundle that is in contact with solution is increased by the surface area of a whole tube (I_s). Since the contact point size is relatively small for MWCNTs with a diameter beyond 10 nm, the tube-solution interaction energy loss at the tube-tube contact point is not considered here.

When a tube is attached to two tubes as in situation 2, two pairs of tube-tube interactions are introduced, resulting in a $4I_t$ increment in *S*. The attached tube leads to one sixth of the surface area of each tube being isolated from the solution (blue dashes in Figure 4.8-d). Thus, the net increment in contact area with solution is half of a whole tube and the corresponding ΔS is $\frac{1}{2}I_s - I_s$. Likewise, in the last situation where one tube attaches to three tubes, three pairs of tube-tube interactions ($6I_t$) are added while the net increment in contact with the solution is zero.

If a bundle grows in the order proposed in Figure 4.8-a, for the M layer of shells containing 6M tubes, K is an integer used to index a tube in a shell layer. The shell grows in the sequence of K = 1 to 6M. Then for $N=2\rightarrow\infty$ the corresponding situation for each added tube can be determined by the following rules:

$$\text{situation 1, } K=1,M=1 \tag{4.4}$$

$$\text{situation 2, } 2<K<M,M=1 \tag{4.5}$$

$$\text{situation 3, } K=M,M=1 \tag{4.6}$$

$$\text{situation 2, } K \bmod M=1\cap K\neq 1,M>1 \tag{4.7}$$

$$\text{Situation 2, } K=2,M>1 \tag{4.8}$$

$$\text{Situation 3, } K \bmod M\neq 1\cup K=1\cap K\neq 2,M>1 \tag{4.9}$$

4.4.3.2. Tangling of CNTs or CNT bundles

The previous section presented the bundling of CNTs with the assumption that they are parallel. Here, another possible agglomerating scheme of the CNTs is discussed where CNTs or CNT bundles attach to each other in a non-parallel fashion. This type of aggregation is also widely reported in the literature, and is often referred to as tangling of CNTs (Hone, Whitney et al. 1999). The real tangling morphology is very

complex, where the tubes are curved and intersect with each other in a range of angles.

To present the effect of tangling on the self-energy of CNTs, a 3D mesh model is proposed here as shown in Figure 4.9-a. In Figure 4.9-a, every bar can be regarded as a CNT or a bundle of parallel CNTs. The spacing of these bars (a) is used to represent the density of agglomeration and a constant intersecting angle (θ) is assumed. For more intuitive demonstration and the simplicity of calculation, this 3D mesh model can be equalized to a 2D mesh model (Figure 4.9-b), where the a is reduced to 0.5a. Every bar in this 2D mesh has the same number of intersecting bars as in the 3D mesh.

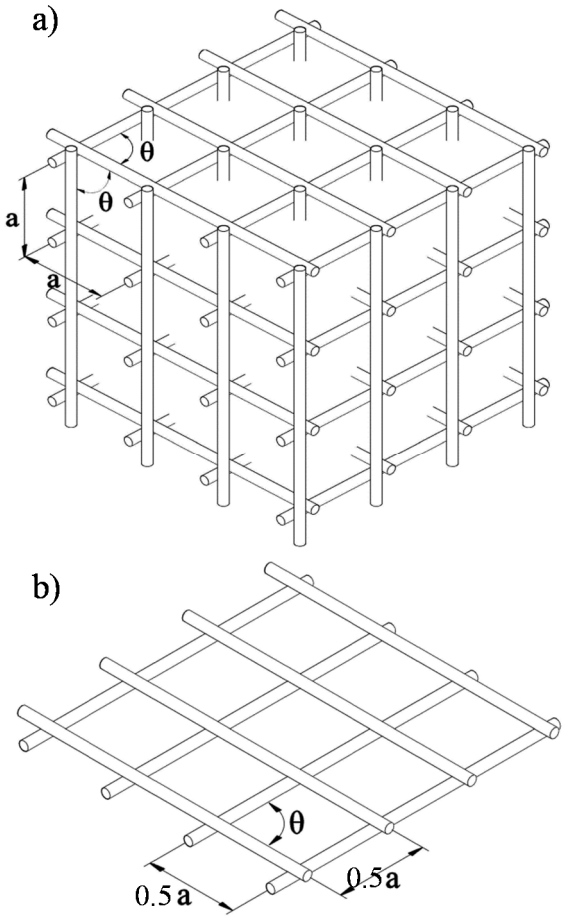

Figure 4.9. 3D (a) and 2D (b) mesh models for a tangled CNT network. Every bar in this figure indicates a CNT bundle which contains one or more parallel CNTs.

Using the 2D mesh model, if one bundle containing N tubes intersects with n $(n=2L/\alpha)$ other bundles, each of which also contains N tubes, the increase in S due to the intersection can be expressed as

$$S_t(x) = k\frac{nI'_t}{NL},\ 2 \le n < \frac{2L\sin\theta}{d_f};\ \ S_t(x) = 0, n < 2 \qquad 4.10$$

where $S_t(x)$ is the average self-energy due to tangling for a mesh containing x CNTs ($x = 2nN$ or $x = \frac{3}{4}n^2N$ in an equivalent 3D mesh), L is the length of each tube, d_f is the diameter of the tubes, k is a coefficient that describes how many pairs of tube-tube interactions are introduced at the bar-bar intersecting point (e.g. for a 19-tube hexagonal bundle k varies between 1 to 3 since there is a maximum of 3 tubes at one edge of the bundle), I'_t is the angle dependent variants of I_t. For the MWCNT used in this study, I'_t for different angles was computed using MD simulation and is plotted in Figure 4.10. It can be seen that the smaller the angle, the stronger is the CNT-CNT interaction (indicated by more negative I'_t).

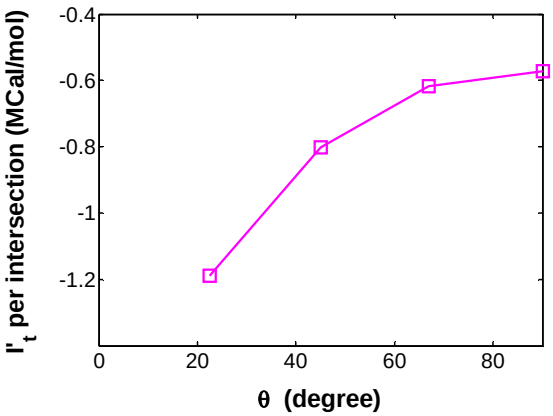

Figure 4.10. Tube-tube interaction energy for MWCNT at different intersecting angles.

In summary, the general expression for a CNT or CNT agglomerate containing x tubes (μ_x) is given as

$$\mu_x = \frac{\sum_{N=1\to x} \Delta S + S_t(x)}{x} \qquad 4.11$$

4.4.4. SIMULATION OF AGGLOMERATING PROCESS AND IMPLICATIONS FOR DISPERSION

In this section, the proposed CNT agglomeration is implemented on the NC and SL-CNT suspensions. I_t is calculated to be -107.Kcal/mol/nm based on the MD simulation on a pair of (100,100) CNTs. The input parameter I_s for the model is obtained by MD simulation where the SL and NC-MWCNTs systems are simulated at atomic level. The snapshots in Figure 4.11 provide views of typical assembling morphologies of the surfactants on the CNT surface. In both assemblies, the hydrophobic groups on the surfactants (e.g. methyl and phenyl groups) attach to the CNT surface whereas the hydrophilic groups (e.g. hydroxyl and sulfonic groups) face the solution. The repulsive force between the negatively charged hydrophilic groups resists the reagglomeration of the CNTs (Islam, Rojas et al. 2003, Richard, Balavoine et al. 2003).

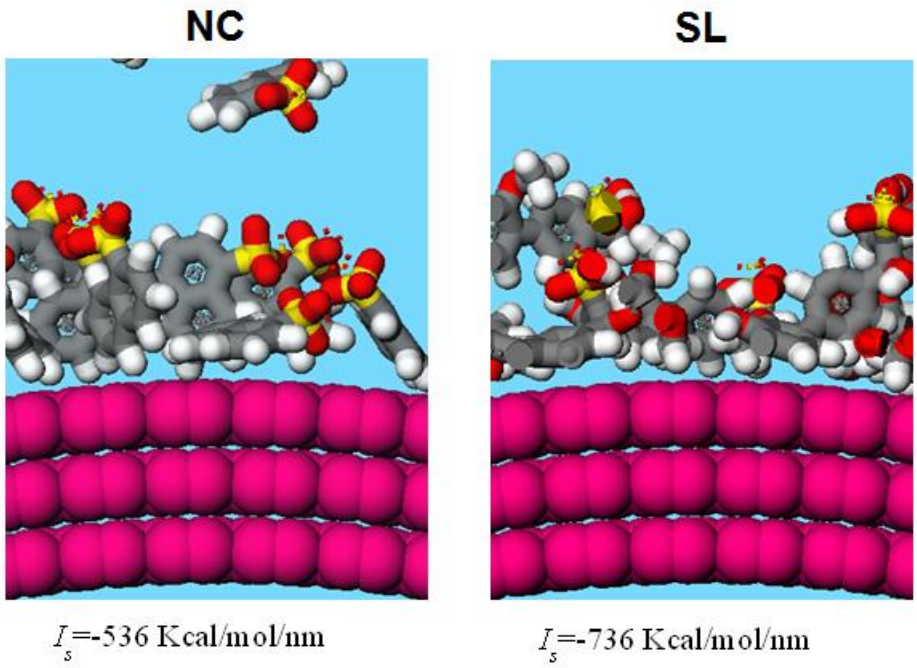

Figure 4.11. Interaction energy (IE) per unit length of CNT and snapshots of NC (left) and SL chain (right) aggregations on a simulated (100, 100) triple-walled CNT surface. Red: oxygen, Grey: carbon, White: hydrogen, Yellow: sulphur, Purple: CNT surface. Water and CaOH2 are made invisible for clarity.

As shown in Figure 4.11, I_s of the NC-MWCNT system is 24 % less negative than that of the SL-system. Qualitatively, the values of I_s indicate that the SL dispersed individual CNTs are more stable. Based on these values of interaction energy obtained from the MD simulations, it is possible to derive the average self-energy of tubes in different type of agglomeration (parallel bundled or tangled), as shown in Figure 4.12.

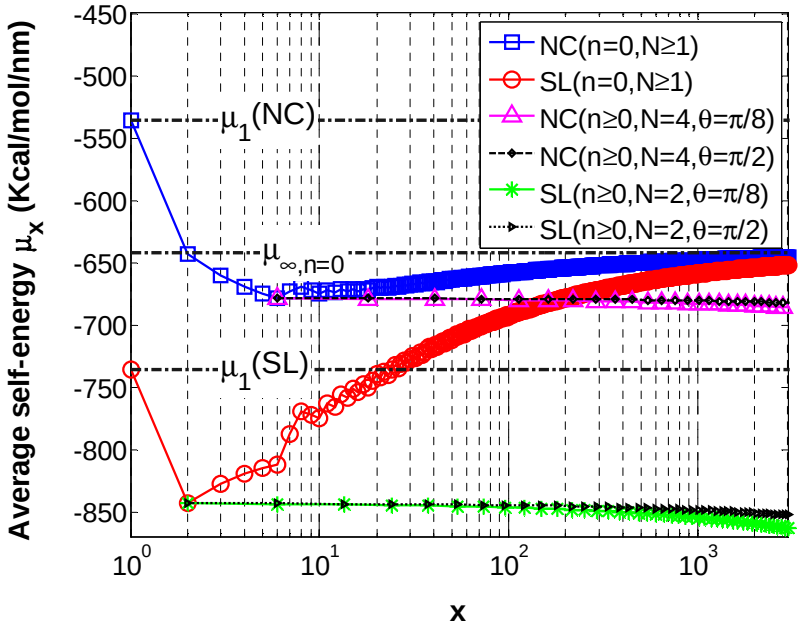

Figure 4.12. Average self-energy μ_x per nm for different cases. The dashed lines show the value of μ_x for indivually dispersed CNTs (μ_1) and parallel bundles of infinite size ($\mu_{\infty,n=0}$). k=3 and 2 for NC and SL respectively. The length and diameter of the CNTs are assumed to be 2 µm and 10 nm respectively.

Using Eq. 4.11, the average-self energy per tube for parallel bundled CNTs (n=0, $N \geq 1$) can be calculated. As indicated in Figure 4.12, for both suspensions when n=0 and N grows towards infinity, μ_x converges to the state of a CNT solid ($\mu_{\infty,n=0}$ in Figure 4.12) where each CNT interacts with only 6 other CNTs, as in its first shell layer. On the basis of the Boltzmann distribution, a more negative μ_x makes the formation of bundles of that particular size energetically preferable and raises concentration of CNTs with this bundle size (Israelachvili 2011). The optimal bundle size with the most negative μ_x is 6 (x=N=6) for NC and 2 (x=N=2) for SL, which implies that these bundle sizes should be a dominant fraction in the respective CNT suspension. This finding partially coincides with the experimental observation of bundle sizes in Figure 4.7, where a significant proportion (45 %) of NC-dispersed

CNT bundles have N greater than 3 whereas the majority (77 %) of SL-dispersed CNT have a bundle size below 3. It should be noted that the model used is an idealized model that does not consider the different diameters and lengths of the CNTs. However, with this model reasonably good agreement with experimental results is achieved.

When the tangling agglomeration is taken into consideration with $n>0$, first, the effect of the intersecting angle is investigated. As shown in Figure 4.12, the difference between the curves with θ = 22.5° (π/8) and 90° (π/2) is small for both NC and SL up to a bundle size of 2000. This indicates that as long as the tubes are not parallel bundled, the intersecting angle does not cause significant changes in μ_x.

The magnitude of μ_x decreases when the parallel bundle size grows beyond the preferred bundle sizes (6 and 2 for NC and SL respectively). If tangling of CNTs is considered, the magnitude of μ_x can keep increasing after reaching the preferred bundle sizes by forming 3D/2D meshes, as shown by the curves with n>0. In these cases, every bar in the mesh models (Figure 4.9) is a bundle of MWCNTs with the optimal bundle size and x is increased by increasing the number of bars within the meshes, which will cause the magnitude of μ_x to further increase because there are more bar-bar intersections.

The energy-preferred agglomeration process predicted by the proposed model for NC and SL is parallel bundling at first, before the optimum bundle sizes is reached, and then tangling to form larger 3D agglomerations. This is borne out by the results in Figure 4.7 which show that the maximum bundle size observed is around 7 and 6 for NC and SL respectively. Further increases in the agglomeration size as shown in Figure 4.6 are due to the tangling of CNT bundles.

An idealized bundle growth model was used in the above analysis of agglomerate development, and good consistency is found between the experimentally observed CNT bundle sizes and the energy preferences based on the model as shown in Figure 4.13. The difference between NC- and SL-MWCNT suspensions can be attributed to the higher I_s between SL and MWCNT. The higher interaction energy of SL may be caused by its longer chain which improves the stability of the SL aggregation because longer chains increase the energy required to detach one surfactant molecule. Furthermore, SL chains are more flexible, allowing them to pack more firmly on the MWCNT surface, as addressed in section 3.3.3.

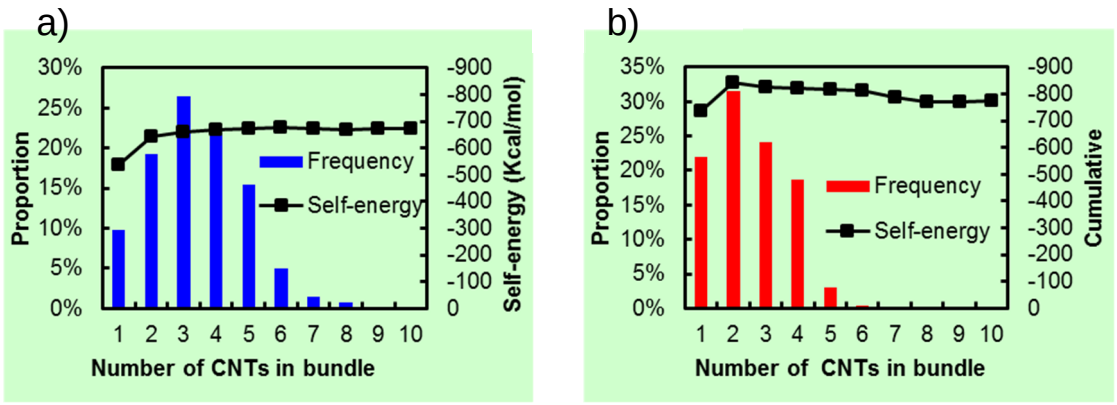

Figure 4.13. Comparison between the measured bundle size and the calculated self-energy for parallel bundles.

4.5. Conclusions

The findings of this chapter are summarized as follows:

• The experiments and simulations indicates that the dispersion efficacy of the three cement compatible additives/surfactants decreases in the order WRDA/SL, 716LR/NC, MA/DBSA.

• UV-vis spectrometry and zeta potential measurements indicates that the dispersion of CNTs using MA is instable whereas dispersions using SL and NC is semi-stable.

• Hydrodynamic size analysis and TEM observation indicates that SL can suspend smaller CNTs bundles than NC can. The bundle size of both SL and NC is found to be below 7.

• A theoretical CNT agglomerating model is developed to simulate the agglomeration process. Using the interaction energy obtained in the MD simulation, the agglomerating model predicts the bundle size of CNTs that matches experimental observations. The model also suggests that CNTs tend to form small parallel bundles (containing fewer than 6 tubes) before forming large 3D lump-like agglomerates.

This chapter demonstrated that although the CNT dispersion using cement compatible surfactants is in a semi-stable state in a Ca^{2+} based alkaline environment, the formation of significant agglomeration is hampered. The results here proof that CNTs can remain as individual tubes or small bundles for a number of hours in an alkaline environment.

The time-dependency of the CNT dispersion in an alkaline environment is critical for optimization of the fabrication process of CNT-OPC paste composite. Therefore more investigation of this time-dependency as well as the dispersion of CNTs in fresh OPC paste is undertaken in Chapter 7.

Before considering optimization of the fabrication process, the reinforcing mechanism of CNTs needs to be understood in the first place. Therefore, the reinforcing mechanism is the focus of the next chapter (Chapter 5).

CHAPTER 5. CRACK BRIDGING MODEL FOR CNTS AND ITS IMPLICATION FOR THE REINFORCING MECHANISM OF CNTS

5.1. Introduction

Like many other fibre-reinforced composites, individual CNTs should be distributed uniformly in the matrix to achieve the ideal isotropic reinforcing effect (Gao, Mai et al. 1988) of CNTs. Unfortunately, CNTs tend to adhere to each other to form large bundles or agglomerates due to the high vdW attraction between them (Girifalco, Hodak et al. 2000, Islam, Rojas et al. 2003).

Ultrasonication (Coleman, Khan et al. 2006, Chen, Collins et al. 2011) is the most commonly adopted technique used to disperse CNTs. Ultrasonication produces rapidly collapsing cavitation bubbles in CNT suspensions that generates high local solvent velocities which can act as both separating forces (Strano, Moore et al. 2003) and scissoring forces (Lucas, Zakri et al. 2009) on CNTs. Separating forces detach individual CNTs from agglomerates or bundles and increase the concentration of dispersed CNTs as a function of UE (Blanch, Lenehan et al. 2011). Simultaneously, scissoring forces tear individual CNTs into multiple shorter CNTs (Frømyr, Hansen et al. 2012) and reduce the average length of CNTs (Hilding, Grulke et al. 2003). As the lengths of CNTs after ultrasonication are usually spread across a wide range (around 50-5000 nm) (Tenent, Barnes et al. 2009, Vichchulada, Cauble et al. 2010, Shuba, Paddubskaya et al. 2012), the length distribution of CNTs is often adopted, rather than the average length (Tenent, Barnes et al. 2009, Streit, Bachilo et al. 2012), to comprehensively depict the shortening effect of ultrasonication.

The dispersing and shortening effects of ultrasonication need to be characterized and quantified experimentally in order to develop models for the reinforcing effect of CNTs. The crack bridging model is used here as a theoretical framework, with supporting experiments. Development of the model contains the following three objectives:

- To define the probability distribution function (PDF) for CNT length at different UEs.
- To characterize the corresponding dispersed CNT concentration at different UEs.
- To incorporate both the length distribution of CNTs and the concentration of dispersed CNTs into Li's micromechanics-based model (Li 1992) to evaluate the effect of UE on the reinforcing efficiency of CNTs.

In terms of the first two objectives, although a number of studies (Hilding, Grulke et al. 2003, Hwang, Ahn et al. 2006, Park, Park et al. 2008, Tenent, Barnes et al. 2009, Vichchulada, Cauble et al. 2010, Shuba, Paddubskaya et al. 2012, Streit, Bachilo et al. 2012) have measured length distribution of CNTs, only a few have catalogued and fitted the distribution with for example, Weibull (Hwang, Ahn et al. 2006) and log-normal (Tenent, Barnes et al. 2009, Streit, Bachilo et al. 2012) PDFs. There are very few published studies of both the fitted length PDFs of CNTs and the corresponding concentration of dispersed CNT as a function of the UE. In the present study, the length PDF of multi-walled carbon nanotubes and the concentration of dispersed CNTs in aqueous solution are characterized experimentally under five different UEs. These length PDFs and the relative concentrations of dispersed CNTs are used in extending Li's microfibre model (Li 1992) to simulate UE-affected CNT composites, meeting the third objective.

To quantify and represent the reinforcing effect of CNTs, Li's micromechanics-based crack bridging stress-crack opening model is chosen in addressing the third objective because crack bridging is one of the most important reinforcing mechanisms in CNT composites (Qian, Dickey et al. 2000), and can improve the tensile strength, ductility, fracture energy and fracture toughness of the composites (Coleman, Khan et al. 2006, Chen, Collins et al. 2011). In Li's model, fibres had 3D random distribution and orientation, the matrix crack plane was planar and matrix deformation was negligible. The interaction between microfibre and matrix was defined as a constant frictional bond τ . When crack opening increased, an individual fibre crossing a crack plane was subjected to a pull-out force and then underwent a debonding-slipping process. During debonding, the frictional stress along the fibre began to increase due to the pull-out force. When the frictional stress at a particular part of the fibre reached τ , that part of the fibre debonded with the matrix and began to slip without further increase of frictional stress. When the frictional stress along the entire fibre reached τ the whole fibre began to slip out from the matrix. Considering that the microfibres, such as CNTs, were infinitesimal with random distribution and orientation, the pull-out forces acting on individual CNTs coalesced to produce a crack bridging stress which is given as

$$\sigma_B = f\left(\delta \mid \tau, d_f, E_f, L_f, V_f\right) \qquad 5.1$$

where δ is crack opening, L_f is the length of fibre, E_f is Young's modulus of the fibre, d_f is diameter of the fibre, σ_B is crack bridging stress, and V_f is fibre volume content in the matrix.

In the present study, Li's model is extended to UE-affected CNT composites. The PDF of CNT length and the concentration of dispersed CNTs are both converted to volume-based measures so that they can be linked to L_f and V_f and used to extend the model to consider the effect of ultrasonication. These formulae, developed in this study, allow calculation of the bridging stress-crack opening relationship at any UE if the corresponding length distribution and concentration of dispersed CNT are given. Using this method, the optimal UE can be predicted. Moreover, the extended model can be used to estimate the interaction between the CNTs and matrix (τ) based on experimental results as in the studies of (Inam, Vo et al. 2012, Metaxa, Konsta-Gdoutos et al. 2013), a procedure that is essential in developing constitutive laws for CNT-reinforced composites.

Li's model and the extended model are analytical models that link the micro-scale fibre-matrix interaction with the macro-scale σ_B. One beauty of this type of model is that it comprehensively considers the distribution of position, orientation and length of micro-fibres by integration and therefore numerical stochastic simulation are not required. Another merit of using these analytical models is that the prediction of UE is not sensitive to τ and E_f, whose values are often difficult to obtain accurately.

5.2. Experimental program

5.2.1. Materials and instrumentation

Multi-walled CNTs were purchased from Nanocyl S.A., Sambreville, Belgium. According to the manufacturer's specifications (Nanocyl 2009), the CNTs had an average diameter of 9.5 nm and an average length of 1.5 μm. The product contains less than 5 % metal oxide impurities and less than 4 % of –COOH functional group. A commercial polyacrylate-based surfactant containing particular types of

polycarboxylate chains that could effectively disperse CNTs (Collins, Lambert et al. 2012) is used as the dispersing agent to improve dispersion of the CNTs in water. .

Ultrasonication was applied using a Vibra-cell VCX 500 ultrasonicator from Sonics & Materials Inc. with a net power output of 500 watt at 20 kHz. This ultrasonicator includes a wattmeter to measure the actual amount of power that has been delivered to the probe and it allows adjustment of energy set points to control the total energy output from the probe (Ø 19 mm). A Shimadzu UV 4800 UV-vis photospectrometer was used to characterize the degree of CNT dispersion. The dried CNTs suspension on silicon wafers was imaged using an FEI Nova NanoSEM™ 450 SEM to obtain tube length information and the diameters of tubes were characterized using a Veeco Dimension Icon AFM in tapping mode.

5.2.2. EXPERIMENTAL PROCESS

First, 6.8 g of dispersing agent was mixed with 0.3 g of CNTs in distilled water to form 320 g of CNT suspension which was then subjected to different UEs. The concentration of the surfactant and the CNTs were chosen according to the experimental study of workability of CNT-OPC pastes which is addressed in section 6.4.2. During the ultrasonication process, the ultrasonicator was run on its maximum amplitude and the depth of the probe in solution was adjusted to maintain the output power at 150±2 watt. The depth of probe must be adjusted since the wattmeter of the ultrasonicator showed large variation in power output (up to ±20 watt) with depth of probe. An ice bath was used to prevent the solution from overheating. The suspension was sampled for microscopy imaging and UV-vis spectra after 25 J/ml, 75 J/ml, 150 J/ml, 250 J/ml and 400 J/ml of ultrasonication.

5.2.3. SAMPLING AND CHARACTERIZATION

To reduce experimental error in the sampling process for UV-vis spectra, the dispersions were sampled three times for each UE. During each sampling process, 60 µL of suspension was pipetted into a cuvette and diluted 50 times using distilled water. This dilution was essential since the ABS of the original dispersion was too large and beyond the measurement limits. Wavelength scans were conducted for the diluted samples from 190 nm to 1100 nm.

For imaging of CNTs, 0.3 µL of the non-diluted dispersion (for each suspension) sampled at each UE was pressed between silicon clips to spread the CNTs. The two pieces of the silicon clips were then separated after drying under room condition. The sample was not coated to allow more accurate measurement of the tubes geometries since the coating adds thickness on the sample surface. Then, SEM and AFM images were randomly taken from the centre of these clips. The SEM was operating at 5 kV to reduce charging for better imaging of the uncoated sample. The AFM was operating with a RTESPA tip at tapping mode. In total, 96 SEM images were taken from samples with different UEs and 15 AFM images were taken on 25 J/ml and 400 J/ml samples. Examples of the SEM images are shown in Figure 5.1 and all the images are collected in the supplementary material.

From the SEM images, the lengths of CNTs were measured using the image analysis software ImageJ. A tube was measured only if it was distinguishable from other tubes or tube bundles and did not extend outside the image.

From the cross sectional profiles of CNTs in the AFM 3D images, their diameters were found to lie between about 5 nm and 15 nm from the samples subjected to different UEs. Thus, for simplicity, a constant diameter of 10 nm was assumed in the subsequent derivations and calculations.

5.2.4. DATA PROCESSING

The measured length data for each UE were fitted with log-normal and Weibull distribution using maximum likelihood estimation. To evaluate the goodness of fit, the Kolmogorov-Smirnov test was performed based on the Kolmogorov-Smirnov statistic (*d*) which is the maximum difference between the cumulative probability functions of the fitted distribution and measured one-dimensional data (Massey Jr 1951). *d* times the square root of the sample size (*N'*) has critical values for different levels of significance (from 0.2 to 0.01), above which fitting is rejected (Massey Jr 1951). The higher the level of significance at which the fitted distribution is not rejected, the better is the quality of fit.

5.3. Characterizing length distribution of CNTs and concentration of dispersed CNTs

5.3.1. ULTRASONICATION-INDUCED SHORTENING EFFECT ON LENGTH DISTRIBUTION OF CNTS

Figure 5.1 shows two typical SEM images of dispersed CNTs sonicated for 25 J/ml and 400 J/ml, respectively. As shown, eight tubes are longer than 1 µm in Figure 1 (a) (25 J/ml), whereas there are only two such tubes in Figure 1 (b) (400 J/ml), indicating the shortening effect of ultrasonication.

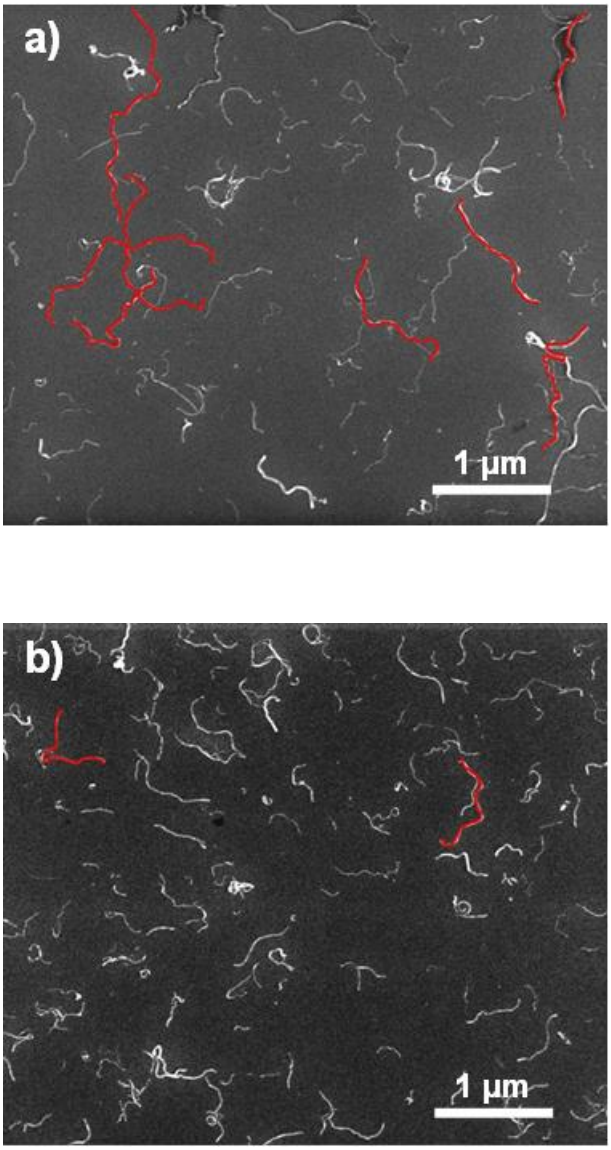

Figure 5.1. Effect of UE on the length of CNTs: (a) 25J/ml and (b) 400J/ml UE. CNTs with length greater than 1 µm are shown in red. These images were taken using the SEM operating under immersion mode with through-lens detector and 5 kV accelerating voltage.

The measured tube lengths for different UEs are plotted as histograms in Figure 5.2. The histograms appear as bell shapes under log scale and the spread of the bell shapes reduces significantly when the UE increases from 75 to 400J/ml.

The CNT length probability distributions were fitted with log-normal and Weibull probability density function (PDF) as suggested in the literature (Hilding, Grulke et al. 2003, Hwang, Ahn et al. 2006) using maximum likelihood estimation. The fitted PDFs are plotted in Figure 5.2 together with the Kolmogorov-Smirnov statistic (*d*) times the square root of the sample size (*N'*) as indicators of the goodness of fit.

It appears that under all five different UEs, $N'^{0.5}d$ for log-normal PDFs is smaller than 1.07 which is the critical value to reject the fitting at level of significance = 0.2 (Massey Jr 1951). In contrast, $N'^{0.5}d$ for Weibull PDFs is greater than 2.40, which exceeds the fitting rejection criteria, 1.63, for level of significance = 0.01 (Massey Jr 1951). The Kolmogorov-Smirnov test results show that the length distribution has a very high likelihood of following the log-normal distribution with the PDF given by

$$p(L_t) = \frac{1}{L_t\sqrt{2\pi}\sigma} e^{-\frac{[\ln(L_t)-\mu]}{2\sigma^2}} \qquad 5.2$$

where $p(L_t)$ is the distribution of probability of occurrence , L_t is tube length, μ and σ are the mean and standard deviation of the natural logarithm, respectively, e is the natural constant.

Parameters μ and σ, mean, mode, and standard deviation of the log-normal PDFs are listed in Table 5.1 for different UEs. It can be seen that the peak (mode in Table 5.1) of the distribution shifts from 265 to 216 nm as the UE increases from 75 J/ml to 400 J/ml and the standard deviation is also reduced by 57 % from 605 to 273 nm.

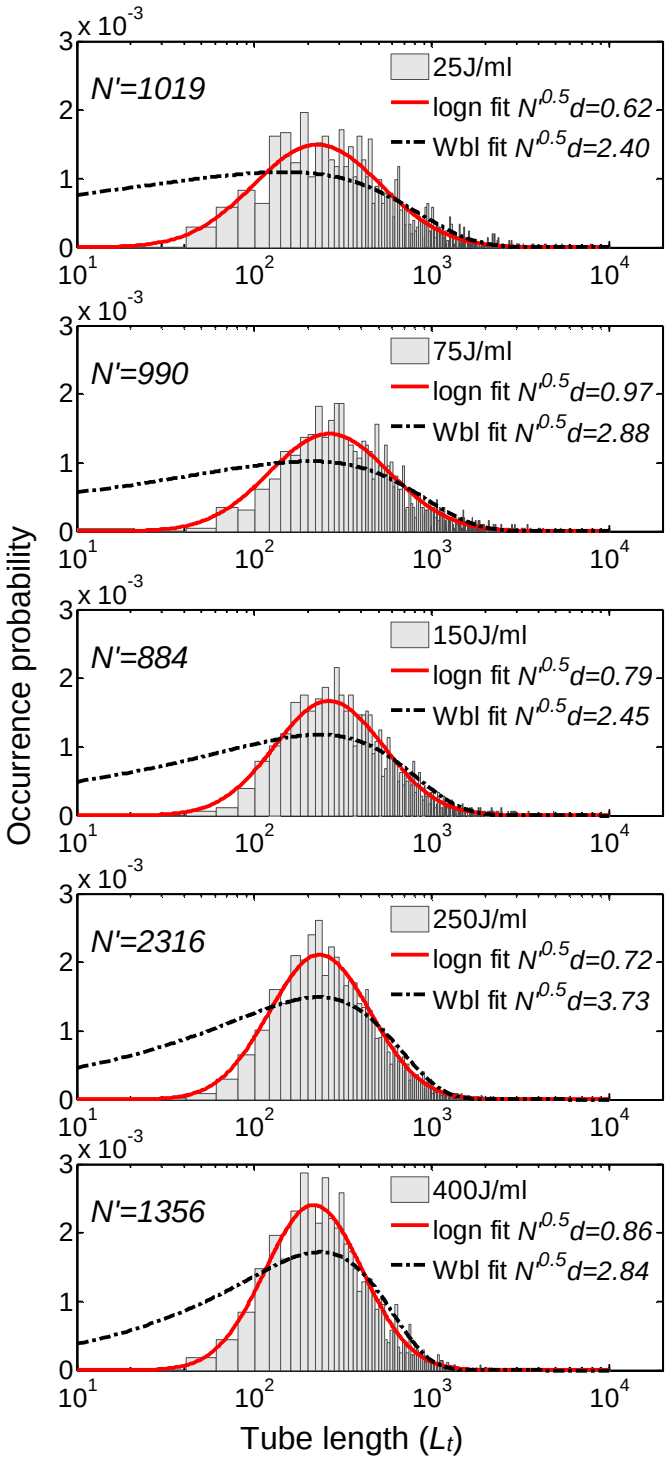

Figure 5.2. Distribution of probability of occurrence of measured CNT lengths for different UEs and the fitted log-normal (logn) and Weibull (Wbl) PDFs using maximum likelihood method. The goodness of fit is indicated by the Kolmogorov-Smirnov statistic (d) times the square root of the sample size (N').

Table 5.1. Parameters for the length-occurrence probability distribution function of different UEs.

UE (J/ml)	Parameter μ	Parameter σ	Mean (nm) $e^{\mu+\sigma^2/2}$	Mode (nm) $e^{\mu-\sigma^2}$	Standard deviation (nm) $\sqrt{(e^{\sigma^2}-1)e^{2\mu+\sigma^2}}$
25	6.12	0.83	640	228	640
75	6.19	0.78	661	265	605
150	6.07	0.71	558	261	450
250	5.88	0.65	444	235	324
400	5.77	0.63	392	216	273

To access the reinforcing effect, the probability distribution needs to be converted to volume distribution of CNT length within composite matrix. Assuming that the CNT diameter is constant and the dispersed CNTs are evenly spread in matrices, the volume of a CNT is then proportional to its length. The volume distribution of CNTs can be given by

$$v(L_t)=\frac{p(L_t)L_t}{\int_{x=0}^{+\infty}p(L_t)L_t dL_t} \qquad 5.3$$

where $v(L_t)$ is the proportion of CNT volume with a specific length L_t within the total volume of dispersed CNTs.

The volume distributions for different UEs are plotted in Figure 5.3. It can be seen that the volume distribution is almost unchanged from 25 to 75 J/ml, whereas the dispersed CNT concentration increases sharply (Figure 5.4 (b)), which implies that below 75J/ml, the UE mainly contributes to exfoliation (Grossiord, Regev et al. 2005, Frømyr, Hansen et al. 2012) of CNTs from large agglomerates while the breakage

(Badaire, Poulin et al. 2004, Lucas, Zakri et al. 2009) and shortening of tubes are less significant (Hilding, Grulke et al. 2003).

Further increase of the UE from 150 to 400 J/ml rapidly reduces the number of long tubes whereas the concentration of dispersed CNTs remains almost unchanged (Figure 5.4 (b)). These results indicate that the UE contributes more to the breakage of tubes after a high dispersion level is achieved and the shortening effect can still be significant at relatively high energy input levels (i.e. 250 to 400J/ml).

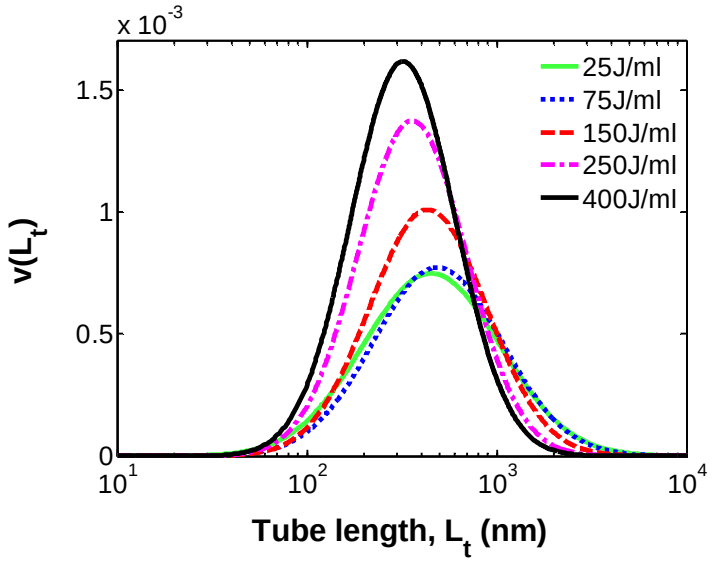

Figure 5.3. Volume distribution curves of CNTs with different UE

5.3.2. Effect of UE on concentration of dispersed CNTs

There are usually two types of particle in CNT suspensions and consequently in matrices: CNT agglomerates and dispersed CNTs (Krause, Mende et al. 2010). The reinforcing effect of agglomerated CNTs can be ignored since their aspect ratio (close to 1 (Krause, Mende et al. 2010)) is much smaller than that of dispersed CNTs (up to 500 in this study). Therefore, the total CNT to matrix volume ratio (V_t) used in the reinforcing effect calculation should be the volume of dispersed CNTs only.

V_t is proportional to its concentration in suspensions, which are often characterized by their UV-vis ABS. The UV-vis spectra for the CNT suspensions subjected to 25J/ml and 400J/ml ultrasonication treatment are presented in Figure 5.4 (a). The curves show a bimodal shape for both samples. The first peak (about 260 nm) can be attributed to dispersed CNTs (Zhang, Su et al. 2006, Goyanes, Rubiolo et al. 2007) whereas the peak at about 970 nm is attributed to the surfactant (ADVA 210), which has nonzero ABS in the wavelength range of 750-1100 nm.

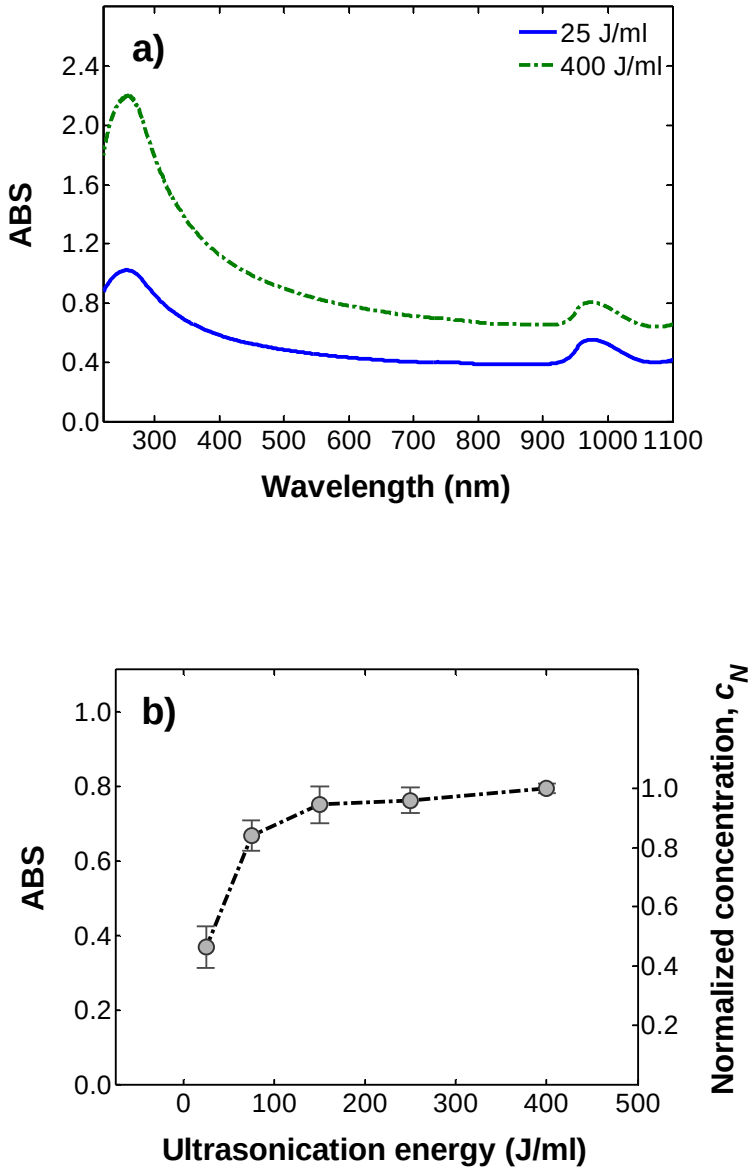

Figure 5.4. (a) Typical UV-vis spectrum of CNT suspensions and (b) ABS and normalized concentration of CNT suspension at 600 nm for different UE. The circles are the mean of three measurments and the error bar indicates 1 standard deviation.

Since CNTs absorb UV-vis light over a wide range of wavelengths, the dispersed CNTs is often quantified using a specific wavelength (Yu, Grossiord et al. 2007, Blanch, Lenehan et al. 2011). The average ABS at 600 nm (Liu, Yu et al. 2010, Vichchulada, Cauble et al. 2010) from three measurements is plotted against the UE in

Figure 5.4 (b). Based on the Beer–Lambert law (Crouch 1988), the concentration of dispersed CNTs is proportional to their ABS. The ABS (Figure 5.4 (b)) is then converted to a relative concentration (C_N in Figure 5.4 b) of dispersed CNTs by normalizing the maximum ABS at 400J/ml to 1. C_N is proportional to V_t when CNT and matrix have constant densities.

As shown in Figure 5.4 (b), ABS increases with the UE. During the process of ultrasonication, both tube exfoliation (Grossiord, Regev et al. 2005, Frømyr, Hansen et al. 2012) from the large agglomeration and tube breakage (Badaire, Poulin et al. 2004, Lucas, Zakri et al. 2009) occur. Since tube exfoliation is more related to the increase in the amount of dispersed CNTs, the sharp increase of ABS/C_N (from 0.72 to 1.54) between 25 to 150 J/ml can be associated with a high exfoliation rate. When ultrasonication exceeds 150 J/ml a plateau is reached, and only a minor increment of ABS is observed. Similar plateaus in the relation between dispersed CNT concentration and UE have been reported in the literature (Krause, Mende et al. 2010, Blanch, Lenehan et al. 2011).

5.4. Microfibre model considering the length distribution of CNTs

In Li's model, the crack bridging stress (σ_B)-crack opening (δ) relationship included two stages: pre-peak (Eq. 5.4) and post-peak (Eq.5.5), which described respectively the σ_B-δ relationship before and after all the fibres at different locations and with different orientations were fully debonded (Li 1992). The formulation of this σ_B-δ relationship was given by

$$\text{Pre-peak: } \tilde{\sigma}_B = g\left[2\left(\frac{\tilde{\delta}}{\tilde{\delta}^*}\right)^{\frac{1}{2}} - \frac{\tilde{\delta}}{\tilde{\delta}^*}\right] \text{ for } 0 \le \tilde{\delta} \le \tilde{\delta}^* \qquad 5.4$$

$$\text{Post-peak: } \tilde{\sigma}_B = g\left(1-\tilde{\delta}\right)^2 \text{ for } 1 \ge \tilde{\delta} \ge \tilde{\delta}^* \qquad 5.5$$

where

$$\tilde{\delta} \equiv \delta\left(\frac{2}{L_f}\right),\ \tilde{\delta}^* \equiv \left(\frac{\tau}{E_f}\right)\left(\frac{L_f}{d_f}\right) \text{ and } \tilde{\sigma}_B \equiv \sigma_B / \frac{V_f \tau}{2}\left(\frac{L_f}{d_f}\right) \qquad 5.6$$

and g is a constant factor describing the snubbing effect due to inclined fibres, varying from 1 to 2.42 (Li 1992). In the present work, a typical g value of 1.4 is adopted for demonstration. Since g is a constant scaling factor, its value will not affect the comparison between different UEs.

To extend Li's model to UE-affected CNT composites, V_f and L_f, which are constant in Li's model, need to be expressed based on the length distribution of CNTs and the concentration of dispersed CNTs. In the CNT composites there are CNTs with different lengths which follow a log-normal distribution, as shown in Figure 5.2. For CNTs of a particular length L_t, the volume fraction in the matrix $V_f(L_t)$ is proportional to the volume distribution $v(L_t)$ as

$$V_f(L_t) = \frac{W_f \rho_m}{W_m \rho_f} v(L_t) = V_t\ v(L_t) \qquad 5.7$$

where W_f/W_m is the weight percentage of the fibres (dispersed CNT in this study) in the matrix, ρ_m and ρ_f are the density of the matrix material and the fibres, respectively. One can assume that ρ_m and ρ_f are constants, and thus the total volume of dispersed CNT (V_t) is proportional to C_N as

$$V_t = C_N V_{t\max} \tag{5.8}$$

where $V_{t\max}$ is the maximum volume of dispersed CNTs obtained after the dispersion plateau is reached.

The pre-peak bridging stress provided by fibres of a particular length L_t can be formulated by substituting Eqs. 5.6 and 5.7 and $L_f = L_t$ into Eq. 5.4, to obtain

$$\sigma_{B,pre-peak}(\delta, L_t) = gV_t\left[\left(\frac{2E_f\tau\delta}{d_f}\right)^{\frac{1}{2}} v(L_t) - \left(\frac{E_f\delta}{\overline{L_t}}\right)p(L_t)\right] \tag{5.9}$$

where $\overline{L_t}$ is the expectation of CNT length and given by $\overline{L_t} = \int_0^{+\infty} p(L_t)L_t dL_t$. To consider the contribution of tubes of different lengths, the total bridging stress from fibres in their pre-peak state is

$$\sigma_{B,pre-peak}(\delta) = gV_t\left[\left(\frac{2E_f\tau\delta}{d_f}\right)^{\frac{1}{2}} \int_a^b v(L_t)dL_t - \left(\frac{E_f\delta}{\overline{L_t}}\right)\int_a^b p(L_t)dL_t\right] \tag{5.10}$$

where the integration boundaries a and b can be determined from $0 \le \tilde{\delta} \le \tilde{\delta}^*$ in Eq. 5.5 as $a = \sqrt{\frac{2E_f d_f \delta}{\tau}}$; $b = +\infty$. In Eq. 5.10, two integrals, $\int p(L_t)dL_t$ and $\int v(L_t)dL_t$,

need to be found. The integral of $p(L_t)$ is the cumulative probability function of the log-normal distribution $\Phi_p(L_t)$ which is in the form of

$$\Phi_p(L_t) = \int p(L_t)dL_t = \left(\frac{1}{2} + \frac{1}{2}erf\left(\frac{\ln(L_t) - \mu}{\sqrt{2}\sigma}\right)\right) \quad 5.11$$

where *erf* is the error function, μ and σ are the parameters in $p(L_t)$. The integral of $\int v(L_t)dL_t$ can be found by changing the integration variable from L_t to $\frac{\ln(L_t) - \mu}{\sigma}$. This integral is denoted as $\Phi_v(L_t)$ and given by

$$\Phi_v(L_t) = \int v(L_t)dL_t = \frac{1}{\overline{L_t}}\exp(\mu + \frac{\sigma^2}{2})\left(\frac{1}{2} + \frac{1}{2}erf\left(\frac{\ln(L_t) - \mu - \sigma^2}{\sqrt{2}\sigma}\right)\right) \quad 5.12$$

By substituting the integration boundaries $a = \sqrt{\frac{2E_f d_f \delta}{\tau}}$ and $b = +\infty$. $\sigma_{B,pre-peak}$ as a function of the crack opening, δ is obtained as

$$\sigma_{B,pre-peak}(\delta) = gV_t\left[\begin{array}{l}\left(\frac{2E_f\tau\delta}{d_f}\right)^{\frac{1}{2}}\left(1 - \Phi_v(\sqrt{\frac{2E_f d_f \delta}{\tau}})\right) \\ -\left(\frac{E_f\delta}{\overline{L_t}}\right)\left(1 - \Phi_p(\sqrt{\frac{2E_f d_f \delta}{\tau}})\right)\end{array}\right] \quad 5.13$$

The contribution to bridging stress from CNTs of different lengths under post-peak condition can be derived in similar manner by substituting Eqs. 5.6 and 5.7 and $L_f = L_t$ into Eq. 5.5 and then integrating about L_t. $\sigma_{B,post-peak}(\delta)$ is given as

$$\sigma_{B,post-peak}(\delta)=\frac{g\tau}{2d_f}V_t\left(\int_{a'}^{b'}v(L_t)L_t dL_t-4\delta\int_{a'}^{b'}v(L_t)dL_t+4\delta^2\int_{a'}^{b'}\frac{p(L_t)}{\bar{L}_t}dL_t\right) \quad 5.14$$

where the integration boundaries a' and b' can be determined from $1\geq\tilde{\delta}\geq\tilde{\delta}^*$ as $a'=2\delta$ and $b'=a$. Therefore the contribution from the post-peak fibres can be written as

$$\sigma_{B,post-peak}(\delta)=\frac{g\tau}{2d_f}V_t\left[\begin{array}{l}\Phi_{vx}(\sqrt{\frac{2E_f d_f\delta}{\tau}})-\Phi_{vx}(2\delta)-\\ 4\left(\Phi_v(\sqrt{\frac{2E_f d_f\delta}{\tau}})-\Phi_v(2\delta)\right)+\\ \frac{4\delta^2}{\bar{L}_t}\left(\Phi_p(\sqrt{\frac{2E_f d_f\delta}{\tau}})-\Phi_p(2\delta)\right)\end{array}\right] \quad 5.15$$

where $\Phi_{vx}(L_t)$ is the integral of $\int v(L_t)L_t dL_t$, which can also be found by changing the integration variable from L_t to $\frac{\ln(x)-\mu}{\sigma}$. $\Phi_{vx}(L_t)$ is given as

$$\Phi_{vx}(L_t)=\int m(L_t)L_t dL_t=\frac{1}{\bar{L}_t}\exp(2\mu+2\sigma^2)(\frac{1}{2}+\frac{1}{2}erf\left(\frac{\ln(L_t)-\mu-2\sigma^2}{\sqrt{2}\sigma}\right) \quad 5.16$$

Finally, the total bridging stress is the sum of the pre-peak and post-peak portions given by

$$\sigma_B(\delta)=\sigma_{B,pre-peak}(\delta)+\sigma_{B,post-peak}(\delta) \quad 5.17$$

Fibre rupture is not considered in this model, as a model with fibre rupture (Victor C. Li and Obla 1994) is too lengthy to be presented here. Moreover, it is reckoned that

the effect of fibre rupture on σ_B is only significant for exceptionally long CNTs with very strong bonding with the matrix. For example, estimation using Eq. 5.17 and the fibre rupture criteria (Victor C. Li and Obla 1994) has indicated that maximum σ_B is not affected by fibre rupture with mean CNT aspect ratio and τ up to 150 and 130 MPa respectively. Li's model and the present formulae are based on the assumptions of stiff and continuum matrix. However, due to the small size of the CNTs, there could be a scaling effect on some of the parameters, such as τ, if the matrix contains pores that are similar in size to the CNTs. Moreover, for a very ductile matrix that sustains large strain without cracking, the model may need to be modified since the CNTs may debond before the crack plane is formed. Therefore, future investigations are needed to determine whether this framework gives reasonable estimation for such porous or ductile matrixes.

5.5. Reinforcing behaviour of CNTs in relation to their length distribution

The derived bridging stress (σ_B) is a function of the crack opening (δ) with μ, σ and the total fibre (CNTs) to matrix volume ratio V_t as UE-related parameters. Eq. 5.17 can also be presented in the form

$$\sigma_B = f(\delta \mid \mu, \sigma, V_t) \qquad 5.18$$

μ and σ represent the length distribution of CNTs, and V_t is determined by the dispersed CNT concentrations. In this section, the effect of different μ and σ is investigated, first without considering the variation in V_t (assuming C_N = 1 and V_t = $V_{t\max}$ in Eq. 5.8). In the next section, various V_t are then taken into account to find the optimal UE.

To demonstrate the calculation of σ_B using Eq. 5.17, the following parameter values are adopted. The typical Young's modulus of CNTs and the interfacial shear strength with the matrix are adopted, being 1 TPa (Yu, Files et al. 2000, Yu, Lourie et al. 2000) and 10 MPa (Coleman, Khan et al. 2006), respectively. A constant diameter, 10 nm, is assumed based on AFM observations in this study. A typical $V_{t\max}$ of 1 % is chosen. Values of the length distribution parameter μ and σ are adopted from Table 5.1 for different UEs.

It should be noted that intense ultrasonication may damage the sidewalls of CNTs and create surface defects and/or peel off graphene layers (Vichchulada, Cauble et al. 2010, Blanch, Lenehan et al. 2011). Defects on the sidewalls can influence the interfacial bonding between CNTs and the matrix (Park, Kim et al. 2011) while peeling off the graphene layer may reduce CNT diameter (i.e. interfacial shear strength τ and tube diameter d_f vary as a function of UE). For reinforcing purposes, it is suggested that intense ultrasonication condition (Blanch, Lenehan et al. 2011) should be avoid in order to preserve the length of CNTs. Most published studies that have implemented mild ultrasonication have indicated minimal sidewall damage to CNTs (Grossiord, Regev et al. 2005, Giordani, Bergin et al. 2006, Liu, Gao et al. 2007, Bergin, Nicolosi et al. 2008) compared with the shortening effect (Blanch, Lenehan et al. 2011). Consistently, microscopic measurements in this study and in that of (Inam, Vo et al. 2012) showed no noticeable change in the average diameter of the CNTs for different UE. Therefore, constant τ and d_f are adopted in the present study for CNTs dispersed under mild ultrasonication conditions.

Figure 5.5 (a) presents the σ_B-δ relationship under a UE of 25 J/ml. The blue solid line is computed based on log-normal distribution (Eq. 5.17); the dotted red line

assumes a contant fibre length (Eqs. 5.4 and 5.5) which equals the average length of the log-normal distribution (640 nm for 25 J/ml). Obviously, a log-normal distribution will drastically increase both the peak and spread of the bridging stress. The peak σ_B and the associated energy absorption (the area under the curve) for log-normally distributed tube length are 2.1 and 8 times those for a constant length. These discrepancies can be attributed to the considerable amount of long CNT tubes in the log-normal distribution as σ_B in Eqs. 5.2 and 5.3 increases with length. The comparison here shows that the log-normal distribution is recommended for evaluating the reinforcing effect of CNTs. Now the effects of different log-normal distributions due to various UEs are examined. The σ_B - δ relationship per unit V_t for different UEs are plotted in Figure 5.5 (b), which indicates that the peak σ_B is reduced with increasing UE due to the change in μ and δ. The drop in σ_B is, however, not significant between 25 J/ml and 75 J/ml due to their similar *v(x)*. From 75 to 400 J/ml, the peak bridging stress decreases sharply by about 50 %.

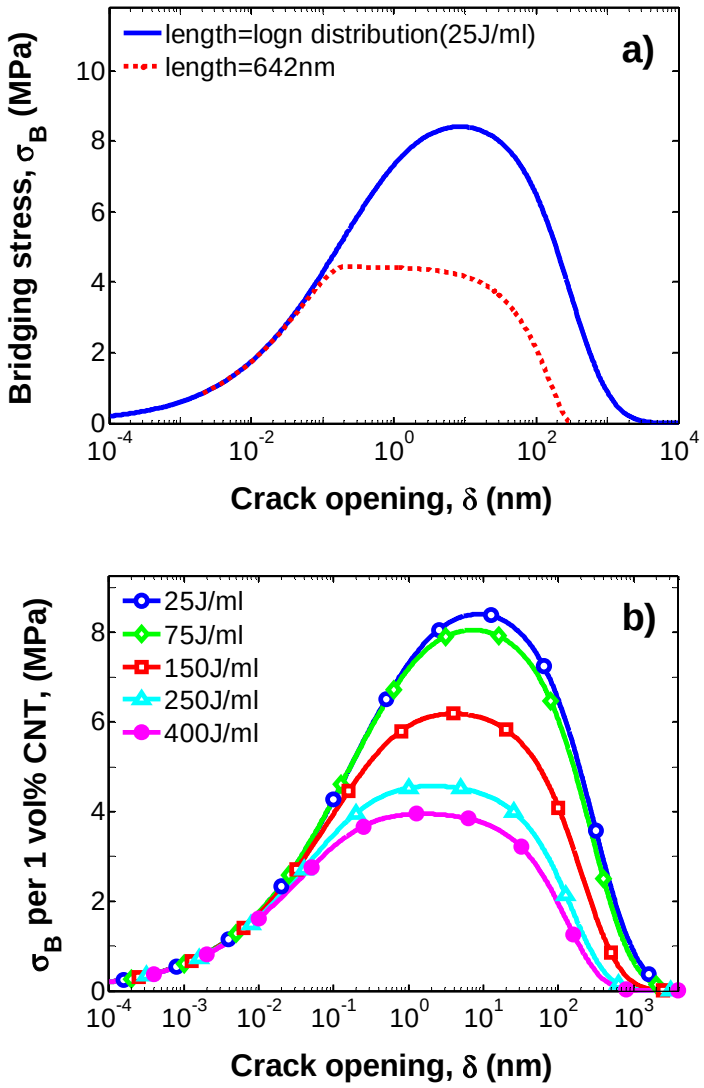

Figure 5.5. (a) Comparison of the σ_B - δ curve between a constant fibre length and a log-normal distributed fibre length. (b) σ_B - δ curves (with V_t = 1%) for different CNT length distributions generated at different UEs.

5.6. **Conclusions**

Observations of CNT length show that it follows a log-normal distribution whose mean and standard deviation decrease with increasing UE. The total volume of the dispersed CNTs is qualified using UV-vis ABS and it increases with UE before reaching a plateau at around 250 J/ml.

The log-normal probability distribution (*p(x)*) is converted to volume distribution (*v(x)*) and the dispersed CNT concentration is converted to the total volume of

dispersed CNT (V_t). $v(x)$ and V_t are then used to calculate the CNT crack bridging stress-crack opening relationship using the formulae developed (Eqs. 5.8 and 5.17) in this study.

It is found that a much higher bridging stress is produced by the same volume of CNTs with log-normally distributed length compared to that with constant length. In addition, for unit volume of dispersed CNTs, the peak bridging stress and the energy absorption during crack bridging decreases monotonically with increased ultrasonication.

In the next chapter (Chapter 6), the proposed crack bridging model is used to predict the optimal UE. Accordingly, experiments are performed to verify the prediction and the reinforcing effect. Furthermore, the calculated bridging stress-crack opening relationship (Eq. 5.18) is used to estimate CNT–matrix interfacial properties and explain experimental results.

CHAPTER 6. OPTIMUM ULTRASONICATION ENERGY FOR CNT-OPC PASTE FABRICATION

6.1. Introduction

In the current practice of CNT composite fabrication, the primary methods of identifying optimal UE have been based on trial-and-error or on the dispersion of CNTs. In the trial-and-error method, multiple batches of specimens with different UE are fabricated, tested and compared (Inam, Vo et al. 2012, Metaxa, Konsta-Gdoutos et al. 2013) to determine the optimal energy. For example, (Inam, Vo et al. 2012), made five batches of CNT-reinforced epoxy specimens from CNTs subjected to 0, 5, 8, 11 and 14 mins of ultrasonication, respectively. The optimal ultrasonication time was found to be 5 mins, since it gave the highest tensile strength among the five batches. In the dispersion based method, the UE is chosen based on adequate dispersion of CNTs (Qian, Dickey et al. 2000, Velasco-Santos, Martinez-Hernandez et al. 2003), which can be assessed by UV-vis spectrum (Krause, Mende et al. 2010, Blanch, Lenehan et al. 2011), liquid laminar flow deposition (Vichchulada, Cauble et al. 2010), etc.

The length distribution and concentration of dispersed CNTs, which vary with UE, are two key factors that affect the reinforcing efficiency of CNTs. Longer tubes improve the anchorage of CNTs (Li 1992) and better dispersion means fewer CNT agglomerates which are ineffective in terms of reinforcing due to their small aspect ratio (Krause, Mende et al. 2010). However, more highly dispersed CNTs usually entail shorter CNT length due to the simultaneously exerted separating and scissoring forces during ultrasonication (Strano, Moore et al. 2003, Lucas, Zakri et al. 2009).

Therefore, the importance of choosing an optimal UE that balances the dispersion and shortening effects has recently been more widely recognized in the fabrication of CNT-reinforced composites (Inam, Vo et al. 2012, Metaxa, Konsta-Gdoutos et al. 2013).

In this chapter, the crack bridging model in Chapter 5 is used to predict the optimal UE that produces the best reinforcing effect of CNTs in CNT composites. To verify the prediction and validate the crack bridging model, the effects of UE on the CNT dispersion and the Young's modulus E, flexural strength σ_f, and fracture energy G_F of the CNT-OPC paste are investigated via experiments.

Moreover, studies have shown that UE changes the degree of dispersion of CNTs (Chen, Zou et al. 2014), consequently altering the contact surface area between CNTs and cement matrix (Collins, Lambert et al. 2012), which can lead to changes in the amount of surfactant absorbed by CNTs and hence affect the workability of OPC paste. Therefore, the effect of UE on the workability of the CNT-OPC pastes is also investigated.

The influence of UE on the dispersion of CNTs was analysed via UV-vis and optical microscope observations. The workability and mechanical properties of CNT-OPC pastes were assessed by the mini-slump and notched beam tests, respectively. In addition, a CNT dosage-independent optimum UE is determined for practical applications.

6.2. Optimal UE predicted by crack bridging model

Figure 5.5 (b) indicates that σ_B per unit V_t decreases monotonically with increasing UE. Conversely, V_t increases monotonically with UE since the concentration of the

dispersed CNTs (C_N) increases with UE, as shown in Figure 5.4 (b). This trade-off results in an optimal UE that produces the best reinforcing effect.

To consider both the shortening effect and the increased dispersion at different UEs, one can multiply the σ_B curves in Figure 5.5 (b) by their corresponding C_N in Figure 5.4 (b) (or substitute various C_N into Eq. 5.8) to obtain the weighted σ_B in Eq. 5.17 . This weighted σ_B is a relative measure which can be used to find the optimal reinforcing effect and the corresponding UE.

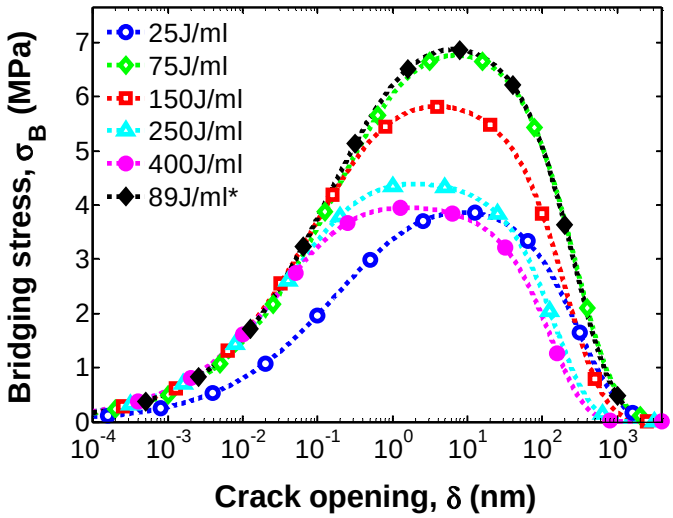

Figure 6.1. Weighted bridging stress which considers the volume ratio of dispersed CNTs ($V_t = C_N \times 1\%$) under different UEs (25-400J/ml). For 25, 75, 150, 250, and 400J/ml, the corresponding V_t are 0.46, 0.84, 0.94, 0.96, and 1 %, repectively. The asterisk indicates the optimal UE that gives the highest peak σ_B, which is predicted by interpolating μ, σ, and V_t.

As shown in Figure 6.1, 75 J/ml appears to give the highest weighted bridging stress of the five measurements as it balances the shortening effect and the dispersion of CNTs. The values of μ, σ, and V_t at any UE between 25 to 400 J/ml can be found by interpolation based on curves (i.e. spline) fitted using the five sets of measured μ,

σ and V_t. By calculating σ_B based on interpolated μ, σ, and V_t, the optimal UE is predicted to be 89 J/ml, which produces a slightly higher peak weighted bridging stress than 75 J/ml. In contrast, the composite can achieve only about half of the optimal peak bridging stress (at 89 J/ml) with inadequate (25 J/ml) or excessive (400 J/ml) ultrasonication.

The results here suggest that the optimal UE should be found before the dispersion plateau (250 J/ml as in Figure 5.4 (b)). In the current prediction, the optimal UE is associated with about 80 % of the maximum dispersed CNT concentration. Further, all curves in Figure 6.1 show that the peak σ_B is reached at a very small crack opening (less than 10 nm) and diminishes within 1 µm. As a result, the bridging stress occurs at the very beginning of crack opening and resists further opening of the crack. These predicted σ_B curves agree with the early crack resisting nature of CNTs as suggested by (Li, Wang et al. 2007, Ganß, Satapathy et al. 2008)

6.3. Experimental program

6.3.1. MATERIALS

Type GP OPC, conforming to the requirements of Australian Standard AS 3972 (AS 3972 2010), was used as the binder material. Multi-walled CNTs functionalized with COOH groups were purchased from Nanocyl S.A. in Belgium. The –COOH functionalised CNTs were used here instead of the non-functionalised CNTs used in Chapter 3 and 4 which are aimed to study the thermodynamics of CNT dispersion. The theoretical model in Chapter 4 suggests that the CNTs may agglomerate gradually in alkaline environment. –COOH functionalised CNTs were used here to improve dispersion of CNTs in such environment. The physical properties of the nanotubes are shown in Table 6.1. A commercially available polycarboxylate-based

cement superplasticizer (PC), named as ADVA 210 (supplied by Grace Australia Pty. Ltd.), was used. The PC contains both active non-polar groups for adsorption on the surface of CNTs and polar groups to attach on OPC particles/water in aqueous solution, thereby assisting in the dispersion of both OPC and CNTs. (Uchikawa, Sawaki et al. 1995, Yamada, Takahashi et al. 2000, Yazdanbakhsh, Grasley et al. 2009, Collins, Lambert et al. 2012).

Table 6.1 Properties of functionalized CNTs.

Aspect ratio	Average diameter (nm)	Average length (μm)	Carbon purity (%)	-COOH functionalization (%)	Specific surface area (m^2/g)
150	9.5	1.5	>95	<4	250-300

6.3.2. MIX DESIGN FOR CNT SUSPENSIONS AND CNT-OPC PASTES

A total of 12 OPC paste mixes containing four components, namely distilled water (*w*), PC (*p*), CNTs (*C*), and dry OPC powder (*c*), were prepared. The amounts of CNTs and PC in CNT suspensions are defined as CNTs to suspensions weight percentage *C/s* and PC to suspensions weight percentage *p/s*, respectively. The amounts of CNTs and PC in CNT-OPC pastes are defined as CNTs to OPC weight percentage *C/c* and PC to OPC weight percentage *p/c*, respectively. 800 grams of OPC power was adopted for all the mixes. The suspensions (*s*, including *w* and *p*) were fixed at 320 grams, giving the fixed suspensions to OPC weight ratio (*s*/*c* or water to cement ratio) of 0.4. The adopted mount of solid and liquid is within the standard operation volume of the high-shear mixer. As shown in Table 6.2, two mixes of reference plain OPC pastes with *p/c* of 0.55 wt % and 0.70 wt % were designed, denoted R1 and R2, respectively. Two series of CNT-OPC paste mixes with two different *C/c* and five various UEs were designed and denoted CNT-1 series and CNT-2 series. The amount of CNTs and PC adopted here is within the range suggested in the literature (Chen,

Collins et al. 2011). Two patch of control samples with different amount of PC were made to show the effect of PC and workability.

Table 6.2 Mix design of plain OPC paste and CNT-OPC pastes

Mix	*C/s* (wt %)	*p/s* (wt %)	*C/c* (wt %)	*p/c* (wt %)	UE (J/mL)
R1	-	1.375	-	0.55	-
R2	-	1.750	-	0.70	-
CNT-1	0.094	2.125	0.038	0.85	25, 75, 150, 250, and 400
CNT-2	0.188	2.875	0.075	1.15	25, 75, 150, 250, and 400

Note: *C/s* and *p/s* represent CNTs and PC to suspensions weight percentages. *C/c* and *p/c* represent CNTs and PC to OPC weight percentages.

6.3.3. PREPARATION AND CHARACTERIZATION OF CNT SUSPENSIONS

CNT suspensions were prepared by mixing CNT powder with PC in aqueous solutions under ultrasonication using a horn sonicator (VCX 500W) with a cylindrical tip (19 mm end cap diameter). The input power of the sonicator was fixed at 150 watts. In order to prevent the temperature rising, the suspensions were placed in a water-ice bath during ultrasonication.

The dispersion effectiveness of CNTs was characterized using UV-vis spectroscopy with a Shimadzu UV 4800 spectrophotometer with a wavelength range of 190 to 1100 nm (± 1 nm). The measured ABS at a specific wavelength range reflects the degree of exfoliation and dispersion (Grossiord, Regev et al. 2005, Yu, Grossiord et al. 2007) because only dispersed nanotubes can effectively absorb light in the UV-vis region. CNT suspensions were diluted by a factor of 50 for UV-vis measurements. In addition, optical microscope images with 200× magnification were taken for dried CNT suspensions on silicon wafers to assist in investigation of the quality of CNT dispersion.

6.3.4. PREPARATION AND TESTS OF CNT-OPC PASTE SPECIMENS

For each mix in Table 6.2, OPC dry powder was mixed with the CNT suspension using a high-shear mixer according to the procedure as specified in the ASTM standard C1738 (ASTM C1738 - 11a).

Mini-slump tests were conducted to measure the workability of fresh pastes (Collins, Lambert et al. 2012). The geometry and set-up of the mini-cone for the mini-slump are shown in Figure 6.2. The mould was first placed on a flat cellulose acetate sheet, then filled with fresh pastes and compacted with a spatula. When the mould was filled, excess paste was removed from the top surface. The mould was removed vertically to ensure minimal lateral disturbance. The slumped sample was left to harden over 24 hours. The diameter of the hardened spread was measured using a digital vernier caliper at five locations around the outline and the average reading was used.

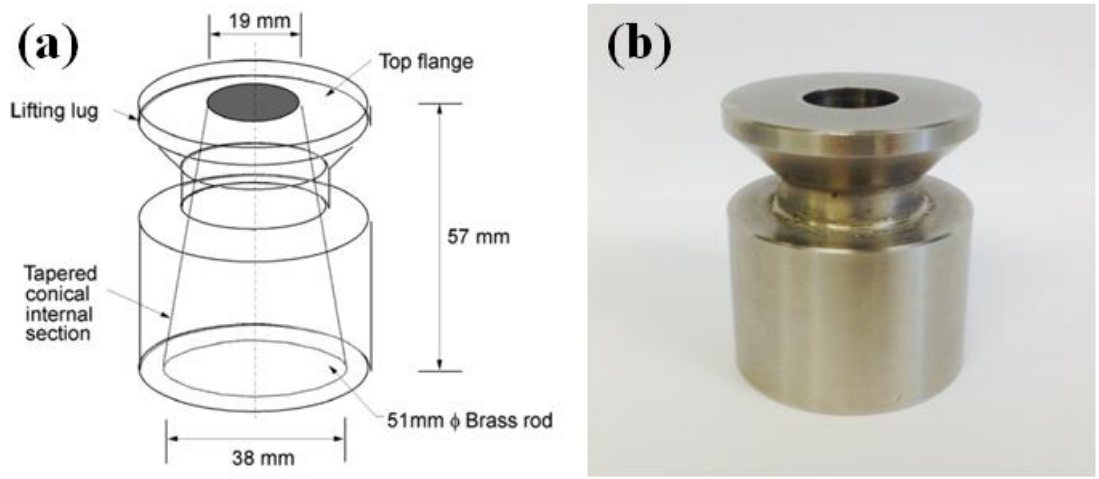

Figure 6.2 (a) dimensions and (b) mini-cone for mini-slump test (Collins, Lambert et al. 2012).

The fresh pastes were poured into moulds and vibrated to release any residual air bubbles. The specimens were then covered under polyethylene sheets for 24 hours in the laboratory environment before demoulding. After demoulding, specimens were cured for 28 days in a tank of saturated limewater at 23 ± 2°C as the moist-curing

regime to satisfy ASTM C192 requirements (ASTM C192 / C192M - 13a). Subsequently, the specimens were stored in a controlled environment kept at relative humidity 50 ± 3 % and temperature 23 ± 2 °C. This environment met the International Organization Standardization (ISO) requirements as a standard atmosphere for conditioning and testing of materials known to be sensitive to variations in temperature or relative humidity.

Following hardening, mechanical properties of the hardened pastes were evaluated by testing notched beam specimens under three-point loading. Figure 6.3 presents the detailed configuration for the test. A 2 kN load cell was installed on an Instron 4204 50 kN loading frame. An extensometer with a 10 mm gauge length and ±1 mm measurement range was attached to the notched beam by rubber bands. All the specimens were loaded to failure at a constant loading rate of 0.01 mm/minutes to maintain stable crack growth. Both the load line deflection and the crack mouth opening displacement (CMOD) were measured. Three specimens were prepared and tested for each mix.

Three different mechanical properties were derived from the load-deflection and load-CMOD curves. These properties were the fracture energy G_F, Young's modulus E and flexural strength σ_f. Based on the work-of-fracture method (Hillerborg 1985, Method 1985), the fracture energy G_F (that measures the work done to fracture a notched beam specimen) was calculated from the area under the load-deflection curve based on the RILEM recommendations (Method 1985), that is, using the equation

$$G_F = \frac{A_o + mg\,\delta_0}{(d - a_0)b} \tag{1}$$

where A_o is the total area under the load-deflection curve, mg is the beam self-weight, δ_0 is the deflection at final failure of the beam, d' is beam depth, b is beam width, and a_0 is notch depth. The Young's modulus E was calculated based on the initial linear

elastic segment of the load-CMOD curves (Shah 1990). Flexural strength σ_f was calculated from the peak load results (Konsta-Gdoutos, Metaxa et al. 2010).

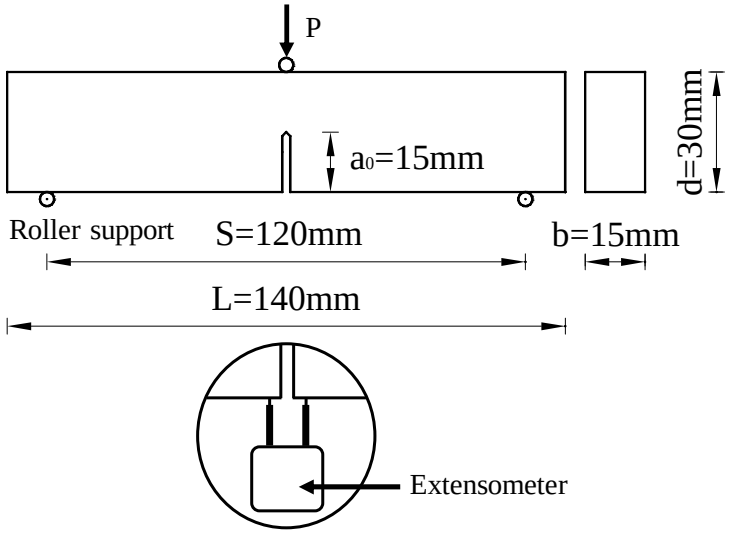

Figure 6.3 Configuration of three-point bending beam test.

The fractured CNT-OPC paste specimens were cut into small pieces to examine the fracture surface of the composite under SEM. In order to demonstrate the crack-bridging effect of the CNTs in the composite, a mix with higher CNT dosage of *C/c* = 0.1 wt % was made and then spread on a silicon wafer. The spread sample was cured for 5 days and then vacuum dried to introduce microcracks for viewing the crack bridging effect of the CNTs. All samples were coated with a thin layer (around 2 nm) of conductive metal (platinum or Iridium) for SEM observation.

6.4. Results and discussion

6.4.1. Effect of UE on the dispersion of CNTs in aqueous solution

The effect of UE on CNT dispersion in aqueous solutions was assessed by UV-vis spectroscopy. The ABS of the CNT suspensions with *C/s* of 0.094 wt % (CNT-1 series) and 0.188 wt % (CNT-2 series) is presented in Figure 6.4. The ABS was measured at a specific wavelength of 600 nm. It is evident that the ABS for the CNT

suspensions gradually increases with respect to the UE. When the UE exceeds 150 J/mL, a plateau is achieved for CNT suspensions with *C/s* of 0.094 wt %. Similarly, the ABS continues to increase and then flattens after 250 J/mL for the suspensions with *C/s* of 0.188 wt %. It is observed that in the range of the plateau the ABS for *C/s* = 0.188 wt % is approximately twice that of *C/s* = 0.094 wt %. On the basis of Beer's law (Yu, Grossiord et al. 2007) the ABS is proportional to the dispersed CNTs. Therefore, the UV-vis results indicate that the amount of dispersed CNTs in an aqueous solution increases concurrently with the UE until a dispersion plateau is achieved. Moreover, a higher UE is required to reach the maximum degree of CNT dispersion with increasing CNT concentration *C/s*.

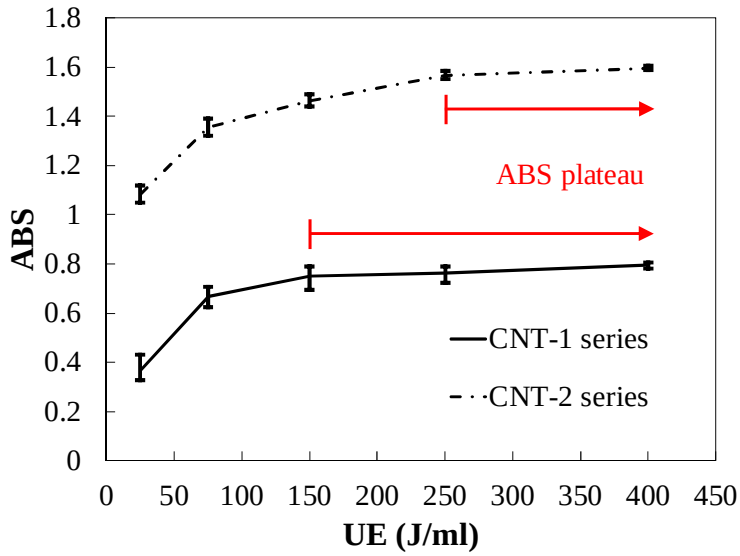

Figure 6.4 ABS of CNT suspensions with *C/s* of 0.094 wt % and 0.188 wt % at five different UEs. Error bar indicates one standard deviation. (Data processing and presentation of this graph were contributed by Mr Bo Zou)

Typical optical microscope images for dried CNT suspensions with *C/s* of 0.094 wt %, at two very different UEs, 25 J/mL and 400 J/mL, are presented in Figure 6.5. Large agglomerates of CNTs are clearly observed when 25 J/mL UE is applied (Figure 6.5(a)). As the UE is increased to 400 J/mL, most bundled CNTs disappear and only small black stains can be observed in Figure 6.5(b). The microscope results

are in good agreement with the UV-vis spectroscopy results, indicating that the dispersion of CNTs can be improved by increasing the UE.

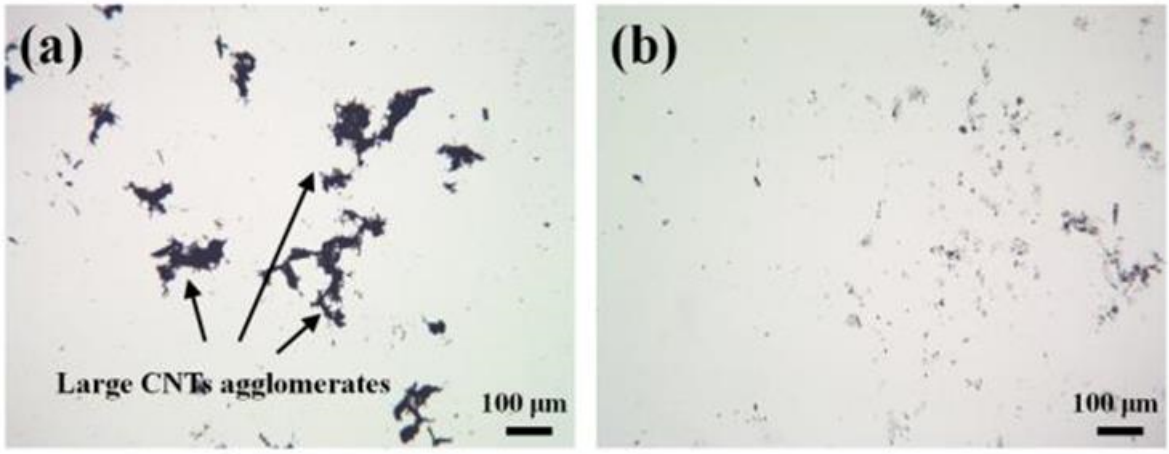

Figure 6.5 Optical microscope images of CNT suspensions at the UE of (a) 25 J/mL and (b) 400 J/mL at 200× magnification.

6.4.2. Effect of UE on the workability of fresh CNT-OPC pastes

The workability of fresh CNT-OPC paste and plain OPC pastes was estimated by mini-slump tests. The mini-slump spreads of the pastes with *C/c* of 0.038 wt % (CNT-1 series) and 0.075 wt % (CNT-2 series) and two control samples (R1 and R2) are presented in Figure 6.6.

The first observation is that the incorporation of PC effectively improves the workability of plain OPC pastes. The mini-slump of plain OPC pastes improves by up to 18 % (from 130 for R1 to 159 mm for R2) with increasing *p/c* from 0.55 wt % to 0.70 wt % (Yamada, Takahashi et al. 2000, Gołaszewski and Szwabowski 2004, Winnefeld, Becker et al. 2007). It should be noted that the workability remains unchanged for R1 or R2 under varied UE, indicating that the amounts of PC used to disperse OPC particles and maintain workability in R1 and R2 are not affected by ultrasonication.

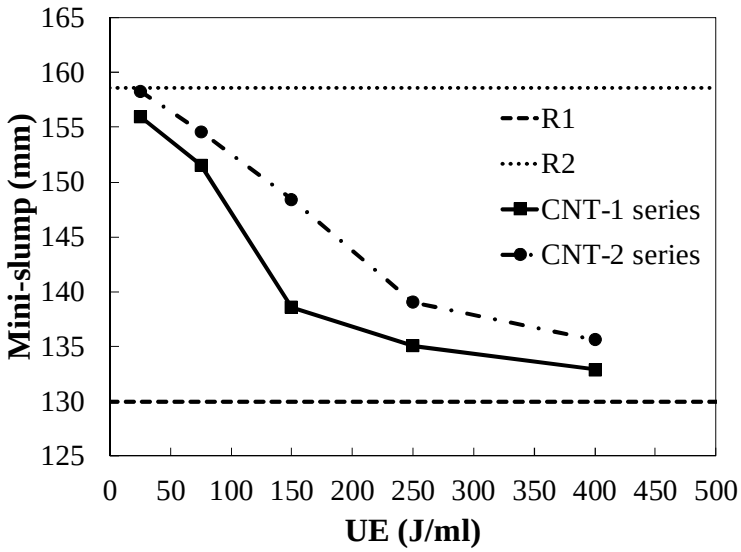

Figure 6.6 Mini-slump spreads of fresh plain OPC pastes with *p/c* of 0.55 wt % (R1) and 0.70 wt % (R2) PC and CNT-OPC pastes with *C/c* of 0.038 wt % (CNT-1 series) and 0.075 wt % (CNT-2 series) at five UEs. (Data processing and presentation of this graph were contributed by Mr Bo Zou)

Interestingly, the workability of the CNT-OPC pastes is related to the UE applied and their slump diameters show a continuous decrease with the increasing UE. For example, the slump diameter, about 156 and 159 mm, for CNT-1 series and CNT-2 series at the UE of 25 J/mL decreases to 133 and 136 mm, respectively, at the UE of 400 J/mL. With a higher UE, increased dispersed CNTs in the pastes adsorb more PC molecules, and the consequent lower amount of PC interacting with the OPC powder results in deterioration in workability. To maintain the workability of CNT-OPC pastes, therefore, an additional amount of PC is required, which can be estimated by the comparison of workability between CNT-OPC paste and plain OPC pastes as shown in the study of (Zou, Chen et al. 2015). At a sufficiently large UE, that is, 400 J/mL, the slump diameters for R1, CNT-1, and CNT-2 series are similar, i.e. 130, 133, and 136 mm respectively. Therefore, it can be estimated that in the CNT-1 and CNT-2 series, 0.30 wt % and 0.60 wt % PC were consumed to disperse the CNTs, respectively, and 0.55 wt % PC was consumed by OPC particles.

On the basis of the assumption that most CNTs are dispersed at a sufficiently high UE, the PC to CNTs mass ratio must be about 8 (= 0.30/0.038 or 0.60/0.075) in order to ensure effective CNT dispersion while at the same time maintaining workability of CNT-OPC pastes. The proposed mass ratio in this study is in agreement with the reported results in the literature. For example, a surfactant to CNT mass ratio of around 4 to 8 has been suggested for common CNT dispersants such as sodium dodecyl sulfate and gemini imidazolium (Yu, Grossiord et al. 2007, Krause, Mende et al. 2010).

6.4.3. Effect of UE on mechanical properties of CNT-OPC pastes

The Young's modulus E, flexural strength σ_f and fracture energy G_F of hardened samples are presented in Table 6.3 with mean values and standard deviations. As shown in Table 6.3, the mechanical performance of R1 and R2 is comparable, with differences within 5 %. These findings are in agreement with studies (Legrand and Wirquin 1994, Puertas, Santos et al. 2005) indicating that the presence of polycarboxylate-based cement superplasticizer does not contribute to ultimate strength when the water content is held constant.

For the CNT-1 series, it is clearly shown that the pastes with a UE of 75 J/mL exhibit the best mechanical performance of all five mixes with UEs from 25 J/mL to 400 J/mL. However, when the *C/c* is doubled to 0.075 wt % in the CNT-2 series, the best mechanical performance is given by the UE of 150 J/mL, indicating that the effective UE shifts from 75 J/mL to 150 J/mL with increased *C/c*. Therefore, the optimum UE that balances the dispersion and shortening effects of CNTs (Chen, Zou

et al. 2014) for achieving mechanically superior CNT-OPC pastes varies with CNT dosage (*C/c*).

Table 6.3 Effect of UE on Young's modulus, flexural strength, and fracture energy of hardened samples at 28 days. (Data processing and presentation of this table were contributed by Mr Bo Zou)

Mix	*C/c* (wt%)	UE (J/mL)	*E* (GPa)			σ_f (MPa)			G_F (N/m)		
			Mean	SD	*I** (%)	Mean	SD	*I* (%)	Mean	SD	*I* (%)
R1	0	0	16.36	0.15	0	4.11	0.06	0	7.28	0.19	0
R2	0	0	16.15	0.16	-	4.20	0.06	-	7.84	0.32	-
CNT-1	0.038	25	17.14	0.21	4.77	4.55	0.26	12.96	8.39	0.41	18.97
CNT-1	0.038	75	18.67	0.07	14.12	5.15	0.06	25.13	9.75	0.25	34.03
CNT-1	0.038	150	18.52	0.11	13.20	5.13	0.18	24.78	9.54	0.10	31.06
CNT-1	0.038	250	18.39	0.09	12.41	4.91	0.16	19.43	9.04	0.17	24.30
CNT-1	0.038	400	18.28	0.19	11.74	4.81	0.22	16.92	8.78	0.21	20.63
CNT-2	0.075	25	17.12	0.34	4.65	4.43	0.24	12.64	8.38	0.15	23.69
CNT-2	0.075	75	19.82	0.18	21.15	5.43	0.04	32.13	10.26	0.18	40.97
CNT-2	0.075	150	21.52	0.38	31.54	6.16	0.20	49.89	11.83	0.66	62.55
CNT-2	0.075	250	21.29	0.19	30.13	6.11	0.14	48.64	11.29	0.22	55.17
CNT-2	0.075	400	20.84	0.21	27.38	5.68	0.09	38.12	10.84	0.10	49.03

Note: *I* represents the mechanical improvement percentage compared with R1.

To determine a CNT dosage-independent optimum UE, the mechanical improvement *I* in Table 6.3 is normalized by CNT dosage *C/c*, defined as the reinforcing index, *RI* . Similarly, the normalized UE is denoted as $\overline{UE}$. The normalization method adopted here is proposed by (Pagani, Green et al. 2012).

The reinforcing indices for flexural strength σ_f (RI_σ) and fracture energy G_F (RI_G) versus $\overline{UE}$ are plotted in Figure 6.7. Interestingly, RI_σ and RI_G for both CNT-1 and CNT-2 series are almost identical and vary with the $\overline{UE}$. Both RI_σ and RI_G reach the maximum at the UE of 20 J/mL per unit *C/c*, prior to the dispersion plateau (from about 40 J/mL per unit *C/c*). It is clear from Figure 6.7 that the optimum UE can be determined as 20 J/mL per unit *C/c*, which also corresponds to 50 J/mL per unit *C/s*.

This UE value is located at approximately 84 % of the maximum ABS for the degree of dispersion, as indicated previously in Figure 6.4.

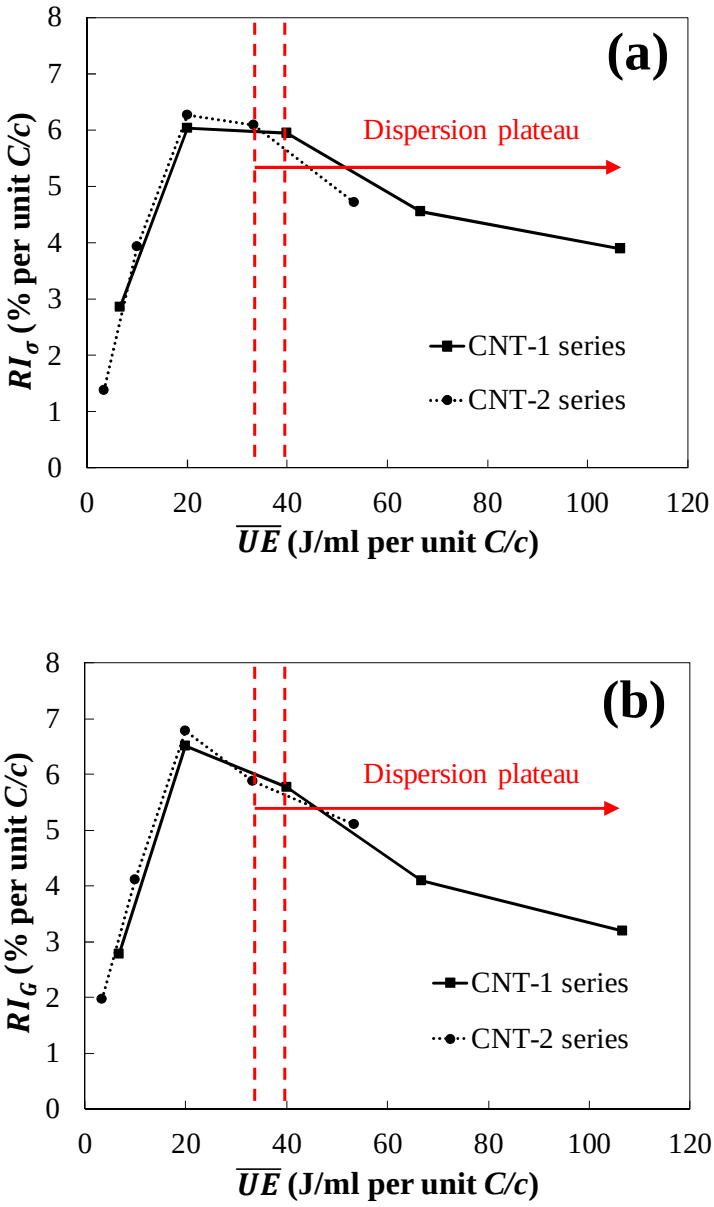

Figure 6.7 Reinforcing indices of (a) flexural strength RI_σ and (b) fracture energy RI_G of CNT-OPC pastes for unit *C/c*. (Data processing and presentation of this graph were contributed by Mr Bo Zou)

The experimentally determined optimal UE value (50 J/mL per unit *C/s*) is in good agreement with the crack bridging model in Chapter 5 (Chen, Zou et al. 2014), which predicts that a UE of 75 J/mL (or 50 J/mL per unit *C/s*) gives the highest

weighted bridging stress. These results verify the effectiveness of the proposed theoretical framework in which the optimum UE, which balances the dispersion and shortening effects of CNTs, is usually obtained before the dispersion plateau is reached. This rule holds because once maximum dispersion is reached, further ultrasonication can only induce a shortening effect and reduce reinforcing efficiency.

6.4.4. REINFORCING ROLES OF CNTS IN OPC PASTE MATRIX

Comparison of CNT-2 (with the UE of 150 J/mL) with R1 in Table 6.3 demonstrates that the incorporation of a very small amount of CNTs (*C/c* of 0.075 wt %) substantially enhances the mechanical properties of plain OPC paste. For example, the Young's modulus is improved by 31.54 %, flexural strength by 49.89 %, and fracture energy by 62.55 %. The improvement percentages of the Young's modulus and flexural strength are comparable with or even greater than the improvements reported in the literature (Li, Wang et al. 2005, Konsta-Gdoutos, Metaxa et al. 2010), confirming the strong reinforcing effect of CNTs on OPC paste.

With recognition of the great influence of pores on the mechanical properties of cementitious materials (Kendall, Howard et al. 1983, Chen, Collins et al. 2011), previous research focusing on the effect of CNTs on the pore structure of plain OPC paste composites has suggested two main reinforcing mechanisms of CNTs in OPC paste matrix, namely the filling of nano-sized gel pores and the bridging of micro-sized capillary pores (Li, Wang et al. 2005, Makar and Chan 2009, Konsta-Gdoutos, Metaxa et al. 2010, Han, Yu et al. 2011, Nochaiya and Chaipanich 2011). CNTs may fill gel pores between C-S-H products, resulting in a reduction in the porosity and an increase in the mean phase stiffness (Li, Wang et al. 2005, Konsta-Gdoutos, Metaxa et al. 2010, Han, Yu et al. 2011). On the other hand, CNTs may bridge capillary pores (i.e. at nano/micrometer level), thus provide higher load bearing capacity of the OPC

paste matrix (Makar, Margeson et al. 2005, Thostenson, Li et al. 2005, Han, Yu et al. 2011). As suggested in Chapter 5 (Chen, Zou et al. 2014), the application of an appropriate level of UE in this study allows sufficient dispersion of CNTs, at the same time preserving nanotube length (Lu, Lago et al. 1996, Mukhopadhyay, Dwivedi et al. 2002), thereby effectively increasing the reinforcing potential of CNTs in OPC paste matrix to achieve enhanced Young's modulus, flexural strength and fracture energy of CNT-OPC pastes (see Table 6.3).

To investigate the crack-bridging and pulling-out behaviour of the CNTs, the fracture surface of the CNT-OPC paste composite was observed under SEM. As shown in Figure 6.8-a, CNT that has been pulled out can be found on the fracture surface with one end embedded in the matrix and the pulled-out end standing free. If this typical pulled-out CNT is viewed at a larger magnification (Figure 6.8-b), one can clearly see the hydration product remaining on the surface of the pulled-out end. One unique feature of CNT pull-out in OPC paste matrix is that the tube can have two types of debonding occurring simultaneously. As shown in Figure 6.8-a and -b, the smooth surface of the pulled-out corresponds to tube-matrix interface shear failure whereas the CNT surface covered with hydration product corresponds to matrix failure. The matrix failure implies that the tube-matrix interfacial bonding is strong, probably due to the covalent bonds formed between the defects on CNTs and the matrix (Li, Wang et al. 2005). These observations show that further extension of the crack-bridging model developed in Chapter 5 (Chen, Zou et al. 2014) is necessary in order to consider both types of bonding failure mechanism in such brittle and porous matrix.

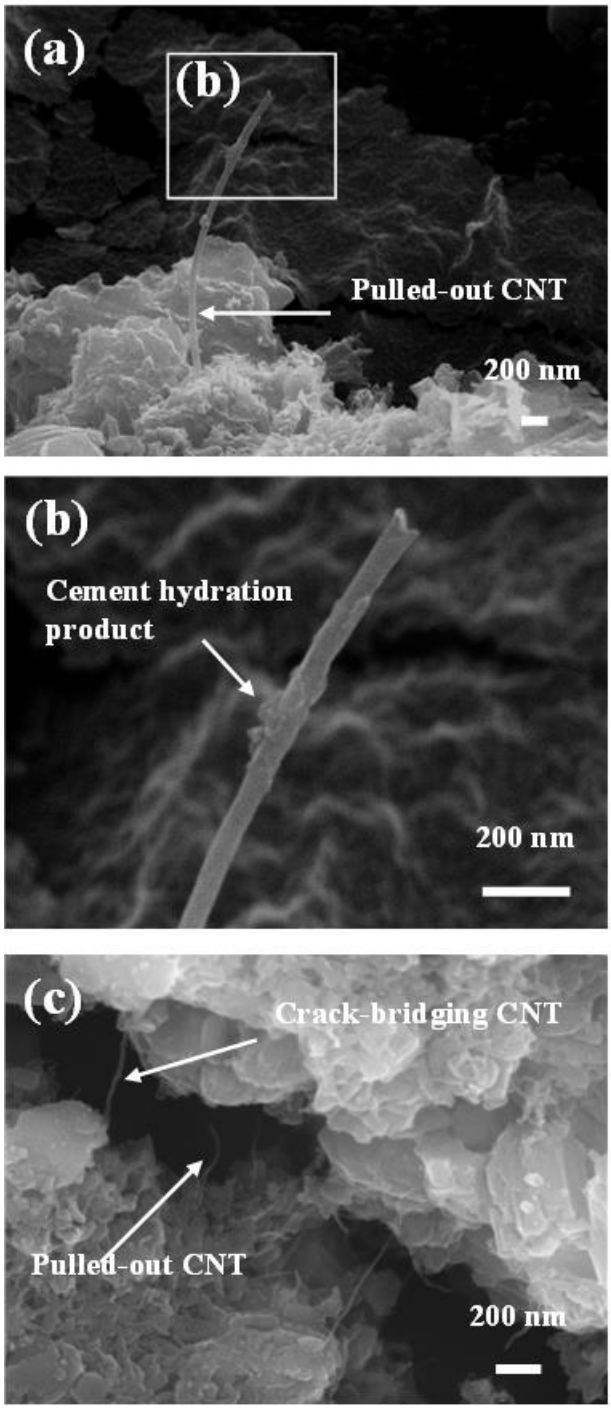

Figure 6.8 SEM images of pulled-out and crack bridging CNTs in OPC paste matrix: (a) A typical pulled-out CNT find on the fracture surface of CNT-OPC paste; (b) The OPC hydration product attached on the outer surface of the CNT; (c) Crack bridging and pulling out of CNTs. These images were taken using a JOEL 7001F SEM operating at 15 kV.

It should also be noted that the reinforcing role of CNTs is rather different from that of conventional microfibres. In the current study, a small amount of CNTs (0.075 wt % of OPC paste) substantially improved the initial slope and the peak load (or the Young's modulus by 31.54 % and flexural strength by 49.89 %, as shown in Table 6.3). However, no significantly extended post-peak softening of the tail is observed in the load–CMOD curves of CNT-2 (Figure 8 in (Zou, Chen et al. 2015)), and the differences in the CMOD at both peak load and failure are visually negligible (Zou, Chen et al. 2015). As discussed previously in Chapter 5 (Chen, Zou et al. 2014), the peak crack bridging stress of CNTs occurs at a crack opening around 10 nm, due to their extraordinarily high Young's modulus and large aspect ratio. As shown in Figure 6.8(c), which is a microcrack on a 5-day old CNT-OPC paste surface with higher CNT concentration, it is evident that the CNTs can indeed bridge cracks from a few hundred nanometres to a few microns. Comparatively, microfibres generally require a few micrometres of crack opening to develop noticeable crack bridging stress. These results show that the bridging effect of CNTs appears as an increase in the strength of the paste composites, which have the unique capability to resist micro-cracks (with crack opening in the range of 10 to 10^3 nm (Chen, Zou et al. 2014)) that cannot be achieved by conventional microfibres. This unique capability of CNTs suggests that the combination of CNTs and microfibre may have the potential to improve both strength and ductility of OPC pastes.

6.5. **Conclusions**

The optimal UE for reinforcing effect can be estimated by substituting the $v(x)$ and V_t obtained at different UEs into the bridging stress calculation (Eqs. 5.8 and 5.17) and comparing the bridging stress. A UE that produces higher bridging stress is expected with superior reinforcing effect.

The effects of UE on the engineering properties of CNT-OPC pastes, including CNT dispersion, workability, Young's modulus E, flexural strength σ_f, and fracture energy G_F, were investigated by varying both UE and CNT dosage. A combination of UE and PC was applied to disperse functionalized CNTs in OPC paste. The main findings are summarized as follows:

(1) More intense UE may effectively improve the amount of dispersed CNTs in aqueous solution before the dispersion plateau is reached, and a higher UE is required to reach the maximum degree of CNT dispersion with increasing CNT concentration;

(2) UE may directly affect the proportion of PC used to disperse CNTs and OPC particles, thereby influencing both CNT dispersion and workability of CNT-OPC pastes. An effective PC to CNTs mass ratio of 8 is recommended for achieving homogeneous dispersion of CNTs in OPC paste and maintaining workability of CNT-OPC pastes under a sufficiently high UE;

(3) To obtain the optimal mechanical performance of CNT-OPC pastes, a CNT dosage-independent optimum UE is found to be 50 J/mL per unit *C/s* (or 20 J/mL per unit *C/c*) and at about 84 % of the maximum degree of dispersion before the dispersion plateau, which are in good agreement with the theoretical prediction and verified the effectiveness of the crack bridging model; and

(4) The significant improvements in the Young's modulus, flexural strength, and fracture energy suggest that CNTs markedly reinforce plain OPC paste by decreasing its porosity and increasing its crack bridging capacity at nanoscale, an outcome that cannot be achieved by conventional microfibres. The combination of CNTs and microfibre may have the potential to improve both strength and ductility of OPC pastes.

The good agreement between the predicted optimal UE and the experimental results validates the proposed crack bridging model. The model also predicts that the higher the concentration or volume content of the dispersed CNTs in OPC paste, the higher the reinforcing effect. In addition, the improvement of mechanical properties is shown to increase with the dosage of CNTs. Therefore, in the next chapter (Chapter 7), the maximum dispersed CNT concentration is explored in order to optimise the dosage of CNTs.

CHAPTER 7. DISPERSION LIMIT AND DISTRIBUTION OF CNTS IN FRESH OPC PASTE

7.1. Introduction

All the property modifications of OPC paste using CNTs are affected by the dispersion and distribution of the CNTs in the OPC paste matrix. However, only limited understanding of the CNT dispersion after mixing with OPC grains is currently available. No published work is known that investigates or quantifies the dispersion status of CNTs in fresh OPC paste matrices. One major difficulty of such investigation is the complexity of the alkaline environment in fresh OPC paste, which contains various types of ions and particles. Moreover, fresh OPC paste is a thick viscous particle suspension that cannot be directly characterized using common techniques such as UV-vis spectrometry.

In this chapter, with innovative approaches to overcome the above-mentioned difficulties, two key questions are addressed in terms of the dispersion status of CNTs in fresh OPC pastes. The answers are essential for better understanding of the reinforcing potential of CNTs. The first question is: What is the maximum amount of CNTs that can be dispersed in OPC pastes? The second question is: How are the CNTs distributed in the OPC matrix?

The first question is important because the amount of CNTs dispersed in the OPC matrix is directly linked to the reinforcing effect of CNTs as suggested by the crack bridging (Chen, Zou et al. 2014). However, an important parameter needs to be identified for the better application of the model, which is the dispersed CNT volume fraction or dispersed CNT concentration (C_d).

To investigate C_d in OPC paste, the dispersion method is critical. For reinforcing purposes, dispersion using surfactants is often desired since it preserves the integrity of the CNT walls. Unfortunately, many of the popular surfactants for dispersing CNTs in water (Zhang, Su et al. 2006, Lee, Huh et al. 2007, Krause, Petzold et al. 2009, Krause, Mende et al. 2010, Bai, Park et al. 2011) have compatibility issues with OPC pastes (Chen, Collins et al. 2011). In the work of (Collins, Lambert et al. 2012), where different OPC paste compatible surfactants (cement additives) were used to disperse CNTs in water, polycarboxylate-based superplasticizer was found to give the best dispersion results. Other researchers (Konsta-Gdoutos, Metaxa et al. 2010, Zou, Chen et al. 2015) have shown that significant improvement in the mechanical properties of the composite can be achieved by using polycarboxylate superplasticizers as dispersant. From these reported results it can be concluded that using polycarboxylate superplasticizers in collaboration with ultrasonication is one of the most efficient methods for dispersing the CNTs for CNT-OPC paste composites.

No study to date has reported the maximum C_d that can be achieved using this dispersion method. Furthermore, the stability of the dispersed CNTs in the alkaline environment in fresh OPC pastes has not been studied. In the present work, therefore, the upper limit of C_d in water is investigated via UV-vis spectrometry and then the stability of the CNT dispersion in an alkaline environment is tested using simulated pore solution. The simulated pore solutions used in this study have been reported as accurately simulating many different ion concentrations in real fresh OPC paste. These investigations will assist in determining the best mass concentration of CNTs to be used in OPC pastes.

The second question arises from the particulate nature of the fresh OPC paste, which is quite distinct from other continuous matrices such as polymers (Tang,

Santare et al. 2003, Song and Youn 2005, Bhattacharyya, Sinturel et al. 2008, Godara, Mezzo et al. 2009, Yang, Gu et al. 2009) and metals (Chen, Tu et al. 2003, Wang, Choi et al. 2009, Bakshi and Agarwal 2011). Fresh OPC paste contains particles ranging from tens of nanometres to hundreds of micrometres, accounting for a volume fraction about 40 % (with water to cement ratio between 0.4 to 0.6) (Taylor 1997). CNTs can only reside in the other 60 % of the volume, that is filled with pore solutions (Taylor 1997). In other words, the distribution of CNTs is not uniform at sub-millimetre scale. This uneven distribution is a significant characteristic of the composite, especially when the microstructural modification effect of CNTs is considered (Li, Wang et al. 2005).

The solid phase (OPC grains) in the particulate matrix entails another factor that can affect the distribution of CNTs in the matrix, which is the adsorption of CNTs on OPC grains due to electrostatic or vdW forces (Israelachvili 2011). This adsorption effect has not been considered in any previous publication: it is, for the first time, investigated and quantified in this study. In this work, a new centrifugation-based technique was developed to separate the adsorbed CNTs and the dispersed CNTs in fresh OPC paste, allowing characterization of the adsorption effect.

After addressing these two key questions, a conceptual model was proposed to describe the dispersion and adsorption of CNTs in fresh OPC pastes. This model can be used to refine earlier cracking bridging models (Li 1992, Chen, Zou et al. 2014) and to develop microstructural and hydration models (Knudsen 1984, Garboczi and Bentz 2001, Bernard, Ulm et al. 2003, Ye 2003, Ye, Lura et al. 2006) for CNT-OPC composites. It should be noted that other particulate matrices such as ceramic and clay (Wang, Ye et al. 2007, White, Best et al. 2007, Chew, Low et al. 2011, Lee, Sang Shin

et al. 2011) may have similar characteristics as to those of OPC pastes, such that this model may be applicable to them.

7.2. Experimental program

7.2.1. Materials and instrumentation

Functionalised multi-walled CNTs (MWCNTs) were purchased from Nanocyl S.A., Sambreville, Belgium. According to the manufacturer's specifications (Nanocyl 2009) the CNTs had an average diameter of 9.5 nm and an average length of 1.5 μm. The product contained less than 5 % metal oxide impurities and less than 4 % of –COOH functional group. A commercial polycarboxylate-based surfactant containing particular types of polycarboxylate chains that could effectively disperse CNTs (Collins, Lambert et al. 2012) was used as the dispersing agent to improve the dispersion of the CNTs in water.

Ultrasonication was applied using a Vibra-cell VCX 500 ultrasonicator from Sonics & Materials Inc. with a net power output of 500 watt at 20 kHz. A Shimadzu UV 4800 UV-vis photospectrometer was used to characterize the degree of CNT dispersion. A 5702 model centrifuge from Eppendorf was used to centrifuge the fresh CNT-OPC pastes.

The dried CNTs suspension on silicon wafers was imaged using an FEI Nova NanoSEM™ 450 SEM with an electron diffraction X-ray (EDX) spectrometer.

7.2.2. Experimental process

One master-batch of CNT suspension was prepared by adding 2.64 wt % of MWCNTs and 10.56 wt % of the surfactant into distilled water. This surfactant-to-CNT ratio was determined by earlier work (Zou, Chen et al. 2015). CNT suspensions with different

total CNT mass concentration (C_t) were obtained by diluting the master-batch with distilled water. Dilution factors of 1:1, 1:5, 1:10, 1:20, 1:50, 1:100 and 1:1000 were used to make the C_t equal to 2.64 wt %, 0.264 wt %, 0.132 wt % 0.0528 wt %, 0.0264 wt % and 0.00264 wt %, respectively. Since the distribution of CNTs is studied in this section using the CNT suspensions, all the wt % presented in this section is of the total weight of the CNT suspension including CNTs, surfactant, and distilled water.

The CNT suspensions with different C_t were then ultrasonicated using the probe sonicator. The intensity and power output of the ultrasonicator were kept at 40 % and 40±3 W respectively. When sufficient UE was applied (Chen, Zou et al. 2014, Zou, Chen et al. 2015) the maximum dispersed CNT concentration (C_d) could be achieved and the CNT suspensions were sampled for UV-vis measurement. Subsequently the ABS at 500 nm was selected to calculate C_d using the Beer Lambert Law given as:

$$C_d = \frac{A}{\varepsilon l} \qquad 7.1$$

where $A = \varepsilon C_d l$ is the ABS at a specific wavelength and ε is the specific extinction coefficient (Baskaran, Mays et al. 2005, Li, Luo et al. 2006, Clark and Krishnamoorti 2009), l = 1 cm is the path length of the light through the CNT suspension. Past studies have shown that ε for MWCNTs lies within a relatively small range between minimum 41.14 and maximum 46.00 with an average of 43.78 ml mg-1cm-1, with no strong dependence on the type of CNTs, surfactant, solvent, or dispersion method (Baskaran, Mays et al. 2005, Li, Luo et al. 2006, Clark and Krishnamoorti 2009). The average, minimum and maximum of the reported extinction coefficients were used to calculate C_d.

To test the stability of the CNT suspensions in alkaline environments, a simulated OPC paste pore solution was prepared with concentrations of the chemicals as shown

in Table 7.1. This composition of the pore solution (Ghods, Isgor et al. 2009) typically represent the concentration of Na+, K+, Ca2+, SO4-, and OH- ions in early age (within about 8 hours) concrete (Rajabipour, Sant et al. 2008). These ions were introduced into the CNT suspensions with different C_t by mixing the suspensions with the simulated pore solution. During mixing the ion concentration was chosen to be above 90 % of the concentration in Table 7.1. The ABSs of these CNT suspensions were then measured every hour until 17 hrs after mixing.

Table 7.1 Concentration of added chemicals in the simulated concrete pore solution

Added compounds	Concentration (g/L)
NaOH	8
KOH	22.44
$CaSO_4\ 2H_2O$	27.55
$Ca(OH)_2$	Sat.

The suspension with C_t = 0.264 wt % was used to investigate the adsorption of CNTs on the surface of OPC grains. 2 ml of the suspension was injected into each Falcon centrifuge tube. Then, 0.1 g, 1 g, 2 g and 4 g of OPC grains were thoroughly mixed with the suspension in four centrifuge tubes for 2 minutes using a spatula. After mixing, the CNT-OPC paste mixtures and the CNT suspension (without added OPC grains) were centrifuged with acceleration of 3000 g (g = 9.8m/s^2) for 7.5 minutes. Upon centrifugation, the OPC particles settled to the bottom of the tubes and the CNT suspension was concentrated to form the supernatant as shown in Figure 7.1. The UV-vis spectrum of the supernatant was measured and C_d was calculated based on Eq. 7.1. When x grams of OPC grains was mixed with the CNT suspension and then centrifuged, the adsorption rate of the OPC grains was calculated by

$$\text{adsorption rate} = (C_d(W_c = 0) - C_d(W_c = x))\frac{V}{x} \qquad 7.2$$

where W_c is the weight of the added OPC grains, C_d (W_c = 0) and C_d (W_c = x) correspond to the C_d in the mixture with 0 gram and x grams of OPC grains, respectively, and V=2ml is the volume of the suspensions.

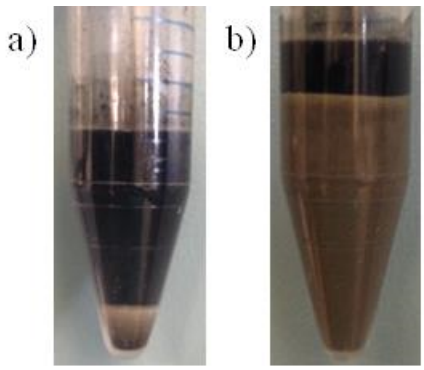

Figure 7.1. CNT-OPC pastes after centrifugation: (a) 0.1 g and (b) 4 g OPC grains. The supernatant is the CNT suspension; the grey settlement at the bottom of the tubes is OPC grains.

To examine the morphology of CNTs attached to the OPC grains, the supernatant in the centrifuge tubes was removed by rinsing with ethanol, and then 10 ml of ethanol was added into the tube and mixed with the OPC settlement using a spatula. Mixing with ethanol was essential to stop the hydration (Taylor 1997) of the OPC grains so that the adsorbed CNTs will not be covered by hydration products and will be easily observed under SEM. The ethanol-rinsed particles were then filtered out using grade 1 filter paper. The residue on the filter paper was spread to dry on silicon wafers in a vacuum chamber. After drying in vacuum for 1 week, the residues were attached to carbon tapes and coated with around 2 nm of gold for SEM imaging and EDX spectroscopy measurement. The SEM operated at 5 kV during the imaging and 15 kV during EDX measurement.

7.3. **Dispersion of CNTs in pore solutions**

7.3.1. DISPERSION LIMIT OF CNTS IN AQUEOUS ENVIRONMENT

Concentration of dispersed CNTs (C_d) is one of the key factors that affect the reinforcing effect of CNTs. As addressed in the crack bridging model (Chen, Zou et al. 2014), the reinforcing efficiency of CNTs is proportional to the amount of dispersed CNTs in the matrix. Therefore a higher C_d is desired for better reinforcing effect. It is well known, however, that CNTs tend to agglomerate in an aqueous environment (Blanch, Lenehan et al. 2010, Blanch, Lenehan et al. 2011), and consequently the C_d is not constantly equal to the dosage of CNTs (C_t), which is the mass ratio between the CNTs and suspension. Figure 7.2-a presents the calculated C_d/C_t ratio using Eq. 7.1 based on UV ABS of CNT-water suspensions. The C_d/C_t ratio gives an indication of the dispersion degree of CNTs in the suspension; a higher C_d/C_t ratio is desirable as it means that more CNTs are in a dispersed state.

First, an appropriate extinction coefficient ε was estimated. As shown in Figure 7.2-a, three values of ε, namely the lower bound (41.14 ml/mg/cm), average (43.78 ml/mg/cm), and upper bound (46.00 ml/mg/cm), were selected from the literature (Baskaran, Mays et al. 2005, Li, Luo et al. 2006, Clark and Krishnamoorti 2009). These values of ε resulted in only a ±10 % variation in the C_d/C_t ratio (or degree of dispersion). Since the C_d/C_t must be less than or equal to 1, ε was found to match the upper bound 46.00 ml/mg/cm, giving the maximum $C_d/C_t \approx 1$. Hence, for all results presented after Figure 7.2-a, ε =46 ml/mg/cm was adopted.

Figure 7.2-a shows that under ideal dispersion condition, C_d/C_t should reach and stay at 1 when C_t is less 0.264 %. $C_t \approx 0.132$ % gives the optimal dispersion and $C_t \approx$ 0.264 % is the maximum dosage that can maintain a high degree of dispersion (>90 %). When C_t is greater than 0.53 % the suspension begins to become saturated with CNTs and the dispersed state of CNTs becomes less energetically feasible

(Israelachvili 2011). Therefore, C_d/C_t was decreased to less than 40 %. When C_t<0.05, the experimentally measured C_d/C_t dropped to 60-65 %. The ideal dispersion, where C_d/C_t remains at 1 when C_t decreases from 0.132 wt %, was not achievable under the current experimental conditions because of the fixed surfactant-to-CNT ratio of 4, resulting in low concentration of the surfactants when C_t<0.05. Consequently, more surfactant dissolved in the solvent as monomers rather than forming an assembly on the CNT surface at low concentration, thereby decreasing the dispersion efficacy of the surfactant (Blanch, Lenehan et al. 2010, Blanch, Lenehan et al. 2011, Israelachvili 2011).

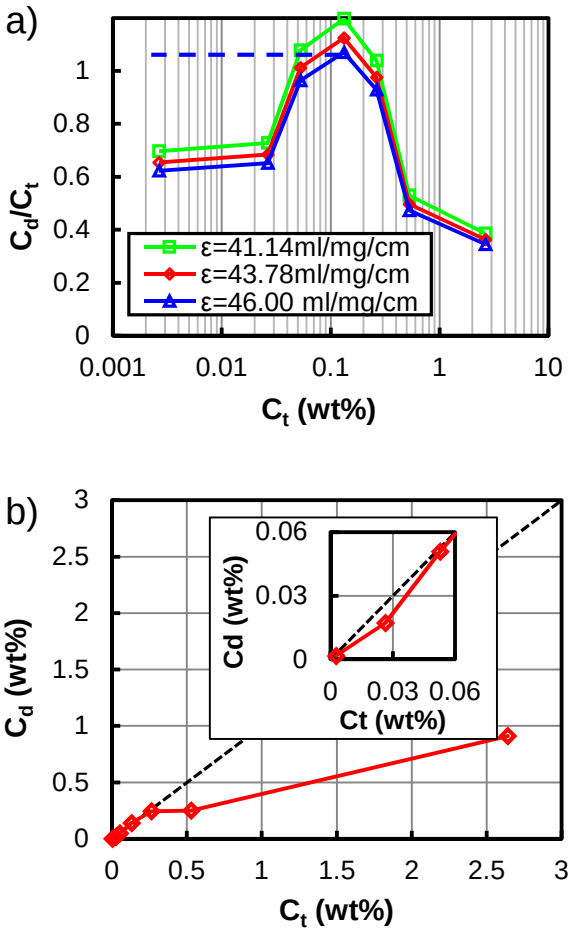

Figure 7.2. Change in degree of dispersion (C_d/C_t, a) and dispersd CNT concentration (C_d, b) with C_t. The dashed line in (b) indicates $C_d = C_t$. The dashed line in (a) shows C_d/C_t under the ideal dispersion condition for ε=46ml/mg/cm. Insert in (b): zoomed-in view of (b) in the range of C_t= 0-0.6.

Apart from the degree of dispersion (C_d/C_t ratio), the upper limit of C_d is another important parameter for the properties of the composite. Figure 7.2-b presents the monotonic change of C_d with C_t. The ideal dispersion case is when $C_d=C_t$ (dashed line in Figure 7.2-b). It can be clearly seen that as C_t increases above 0.264 wt %, C_d gains more bias from the $C_d=C_t$ curve, meaning that more CNT agglomerates. It is notable that at very low concentration, as shown in the insert in Figure 7.2-b, the C_d curve is also slightly biased from the $C_d=C_t$ curve, which may be due to detachment of the surfactants. These results show that C_d could rise to around 0.9 wt % by increasing C_t to 2.64 wt %. The trend of the C_d curve also indicates that C_d may be increased further when C_t exceeds 2.64 wt %. However, using such high concentrations would introduce a fair amount of agglomerated CNTs, with possible detrimental effect on the engineering properties of the composite, for example, causing stress concentration.

7.3.2. STABILITY OF CNTS IN ALKALINE ENVIRONMENT

The dispersion of the CNTs presented in Figure 7.2 was very stable. For example, the C_d/C_t for CNT suspensions decreased less than 5 % after 2 weeks. In contrast, significant changes in C_d/C_t were observed after the simulated pore solution was added into the CNT suspensions. Figure 7.3 shows the change in C_d/C_t for CNT suspensions with different C_t 18 hours after ultrasonication. It can be seen that C_d/C_t has a decreasing trend in general, regardless of C_t. This suggests that the dispersion of CNTs in OPC paste pore solution is not stable in the long term. However, there is a transition point during the change of C_d/C_t as shown in Figure 7.3-a. The transition points can be readily identified by the gradient of the curves.

As demonstrated in Figure 7.3-b, before the transition point, C_d/C_t decreases almost linearly at a low rate (0.7 % per hour for C_t = 0.264 %), whereas after the transition point C_d/C_t decreases sharply in a nonlinear manner. The corresponding

times for the transition points are measured for all the curves in Figure 7.3-a and listed in Table 7.2. Decreasing rates of C_d/C_t before the transition point were also obtained by linear regression. Since the rates of decrease of all the suspensions were found to be very low, with the maximum of 1.9 % per hour, the suspension before the transition point could be treated as stable from the practical point of view. The transition points were found to be greater than at least 4 hours in the range of C_t from 0.02645 % to 2.645 %. OPC pastes normally set within approximately 3-4 hours, and therefore short-term stability of the CNT suspension within an alkaline environment (before the transition point) is sufficient to maintain good dispersion of CNTs in hardened OPC pastes and to avoid reagglomeration of the CNTs.

The mechanism behind the transition point is complex. Former studies of flocculation processes in colloid systems containing fibrous particles have also suggested a two-stage flocculation process (Buffle and Leppard 1995). The existence of the transition point is related to the agglomeration process of CNTs in the pore environment of OPC pastes. Prior to the transition point, CNTs tend to form one-dimensional bundles, each of which contains several parallel CNTs, but after the transition point these bundles further agglomerate into three-dimensional mesh or cage-like large agglomerates. A detailed explanation with the assistance of MD simulations can be found elsewhere (Chen, Zou et al. unpublished).

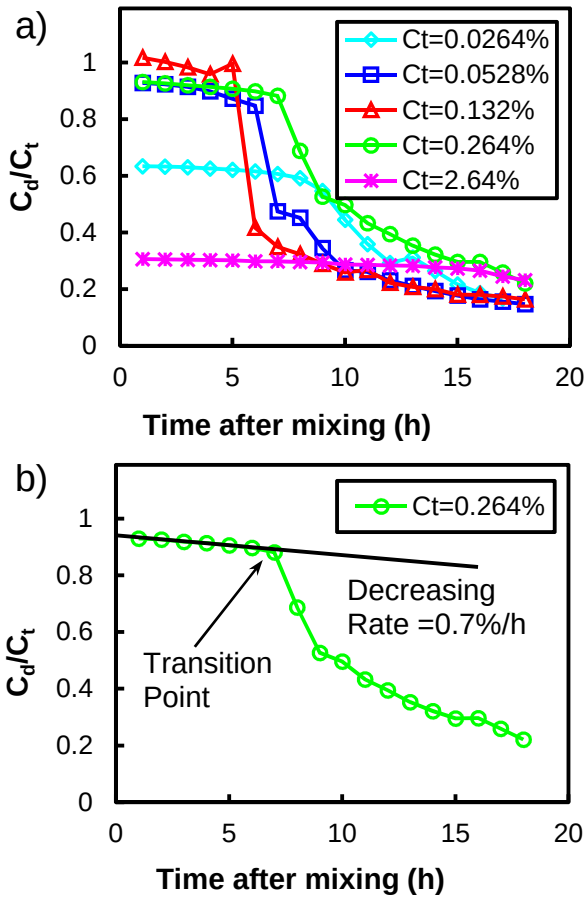

Figure 7.3. (a) Stability of CNT dispersion in simulated OPC paste pore solution at different durations after mixing. (b) Determining the transition point and decrease rate of C_d/C_t.

Table 7.2. Transition time in dispersion state

Total CNT concentration (C_t, wt%)	Transition point (h)	Rate of decrease of C_d/C_t (%/h)
0.0264	8	0.5
0.0528	6	1.6
0.132	4	1.9
0.264	7	0.7
2.64	16	0.2

7.4. **Adsorption of CNTs on OPC grains**

When mixed within OPC pastes, CNTs adsorb on OPC grains due to vdW or electrostatic forces, as well as dispersing in pore solutions as discussed in section 3.

The amount of CNTs adsorbed by OPC grains was measured and is shown in Figure 7.4.

It can be seen that the CNT adsorption rate, defined as the amount of CNTs adsorbed per gram of OPC grains, decreased with the cement-to-water ratio (c/w). If a relatively small quantity of OPC (W_c=0.1g, c/w=0.05) was added into the CNT suspension with C_t=0.264 wt %, around 2.70 mg of CNTs was adsorbed by 1 g of OPC grains. When c/w rose to 1, the adsorption rate reduced significantly to 0.56 mg/g. Adding more OPC grains into the suspensions when c/w >1 produced no noticeable change in the adsorption rates c/w = 2 (or w/c 0.5, which is commonly used in OPC and concrete composites).

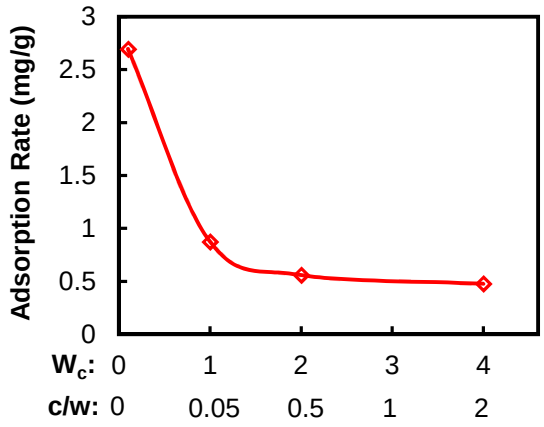

Figure 7.4. Amount of CNTs adsorbed on OPC grains vs the weight of added OPC (W_c) and the cement-to-water ratio (c/w).

SEM images were also taken of OPC pastes with different c/w ratios, as shown in Figure 7.5. The CNTs concentration was fixed at 0.264 wt %. Interestingly, two observations can be made. First, CNT adsorption on OPC grains is selective and preferential to smaller grains (the areas within the yellow dashed lines in Figure 7.5-a and b). Moreover, a thick layer of heavily agglomerated CNTs covers the surface of these small OPC grains (Figure 7.5-a and b) when the amount of added OPC is small

(c/w = 0.005 or w/c=200). As shown in Figure 7.5-c and 5-d, when c/w= 2 (or w/c=0.5), no significantly layer-like agglomeration of CNTs is observed; instead, the CNTs scatter on the OPC grain surfaces. This reduction in the adsorption rate and layer thickness of CNTs was due to the larger surface area of these small OPC grains as well as the more limited space for CNTs to travel during the adsorption process when the cement-to-water ratio increased.

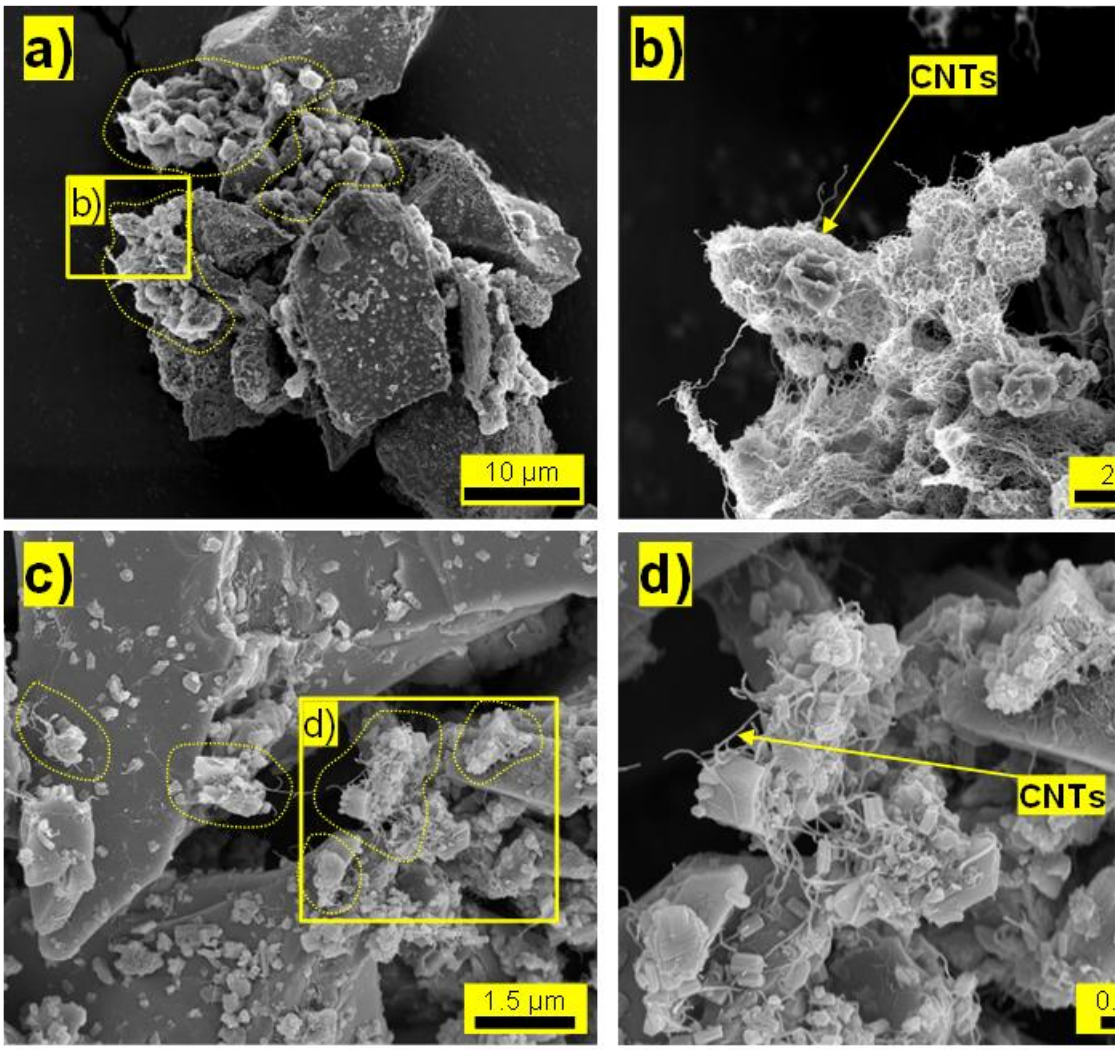

Figure 7.5. SEM images of OPC particles and CNTs adsorbed on OPC particles. (a & b) with 0.1 gram of OPC and (c & d) with 4 grams of OPC concentration 0.264 wt % water to OPC ratio

To understand why CNTs preferred smaller OPC grains, the geometry and chemical composition of these OPC grains were examined. The size of these adsorptive OPC grains was measured based on about 20 SEM images. The particle

size distribution of these OPC grains is plotted in Figure 7.6. The measurement shows that about 98 % of the adsorptive particles are smaller than 4±0.5 µm (the longest dimension). The major components of OPC grains within this size range were most likely to be alite or gypsum (Taylor 1997).

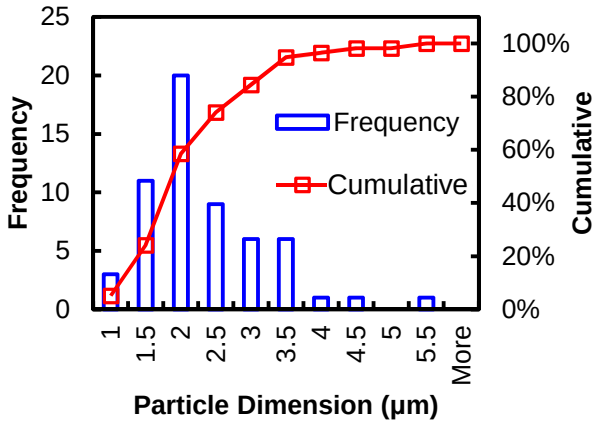

Figure 7.6. Particle size distribution of the adsorptive OPC particles. The particle dimension measured is as the longest dimension of the particle.

Figure 7.7 shows the typical EDX spectra of small (adsorptive) and large (non-adsorptive) OPC grains. Calcium, silica, aluminium and oxygen are detected on both type of grain. Since no sulphur is observed on the spectrum, it is inferred that neither type of grain is likely to be gypsum (Ca_2SO_4), which is a common retarder added into OPC to extend the setting time of OPC pastes (Taylor 1997). Clearly, a very high carbon peak in the adsorptive (or small) grains was caused by the adsorbed CNTs. Another distinction between the two types of grain is that a much more significant peak of calcium is present for the non-adsorptive (or large) grains. This indicates that the non-adsorptive grains are likely to have a higher Ca/Si ratio than the adsorptive ones. Past research has shown that hydration products have a lower Ca/Si ratio (1.57-1.90) (Richardson and Groves 1993) than unhydrated OPC particles that are primarily composed of alite and belite with Ca/Si ratio of 3 and 2, respectively (Gougar, Scheetz

et al. 1996). Furthermore, smaller OPC grains have been found to possess less belite than larger grains (Gougar, Scheetz et al. 1996). Therefore it was inferred that the smaller (or adsorptive) particles contained a higher fraction of hydration products and less belite.

The reasons why CNTs tended to adsorb on smaller OPC grains can be inferred from the results in Figures 7.5-7.7. First of all, the smaller OPC grains (with high fraction of alite) were more active for hydration during the initial hydration reaction (Taylor 1997), leading to more hydration products on them. These hydration products could bond -COOH group onto the CNT surface (Li, Wang et al. 2005). The nucleation effect of the CNTs (Chen, Collins et al. 2011) may also stimulate the growth of hydration products on CNTs near the small OPC grains, causing the CNTs to be precipitated on the OPC grains. Moreover, the geometry of CNTs also contributed to the adsorption on smaller OPC grains. The CNT length was comparable to that of the small adsorptive OPC grains, resulting in a flocculation effect (Buffle and Leppard 1995) where the CNT entrapped small OPC grains in the suspension.

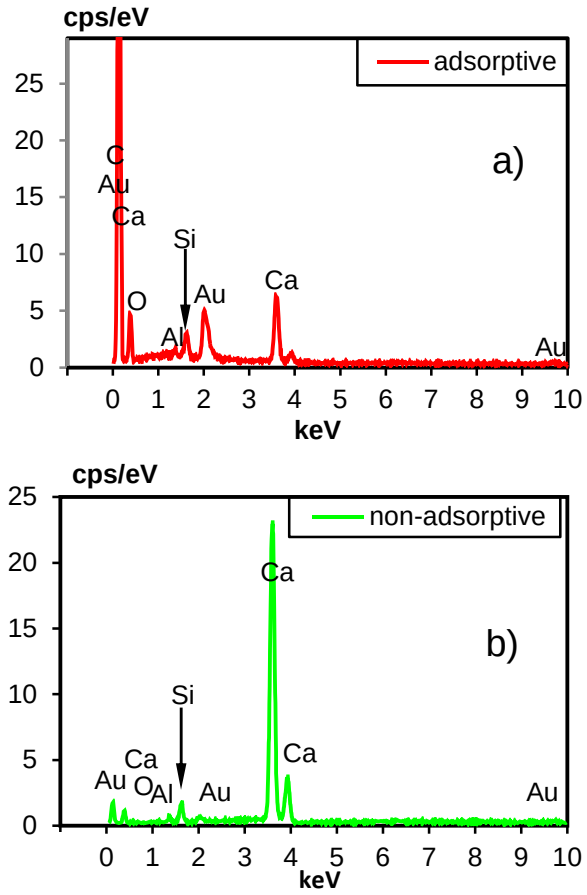

Figure 7.7. Typical EDX spectra for (a) small particles wrapped by CNTs and (b) larger particles without CNTs.

7.5. **Distribution of CNTs in OPC pastes**

As shown in Figure 7.8, at sub-millimetre scale, CNT distribution was not uniform in the fresh OPC pastes. Around 40 % of the space was occupied by OPC grains at common w/c between 0.4 to 0.6 (Taylor 1997), which would result in some CNT-free zones in hardened OPC pastes, that had been occupied by OPC grains in fresh pastes. Realization of this nonuniformity of CNT distribution is critical to the understanding and modelling of hydration, reinforcing effects, and thermal and electrical conductivity of the CNT-OPC composite.

Based on the discussion in sections 3 and 4, CNTs appeared to have three states in fresh OPC pastes, as shown in Figure 7.8, namely the agglomerated state (black), the dispersed state (green), and the adsorbed state (red). Obviously the heavily

agglomerated CNTs had a low aspect ratio and therefore made negligible contribution to the reinforcing effect (Chen, Zou et al. 2014) although they could still act as fillers affecting the hydration and workability of the CNT-OPC paste (Zou, Chen et al. 2015). The amount of agglomerated CNTs can be estimated from Figure 7.2. If C_t is within the range of 0.05 wt % to around 0.25 wt %, the amount of agglomerated CNTs is less than 7 % (calculated from $(C_t\text{-}C_d)/ C_t$) of C_t (Figure 7.2)).

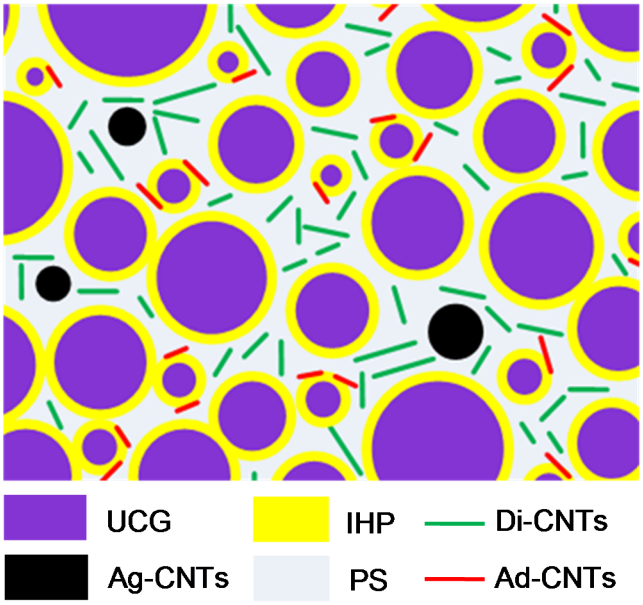

Figure 7.8 A schematic of the distribution of CNTs in fresh OPC matrix. UCG: unhydrated OPC grains; IHP: hydration product formed during initial hydration; Di-CNTs: dispersed CNTs; Ag-CNTs: agglomerated CNTs; PS: OPC paste pore solution; dispersed CNTs; Ad-CNTs: CNTs adsorbed on small OPC particles.

For a common mix of fresh OPC pastes with w/c ratio of 0.5, the amount of adsorbed CNTs was calculated to be 36 % of C_t in the CNTs suspension with C_t= 0.264 wt %. The dispersed CNTs accounted for the remainder (around 60 %) of C_t after mixing with OPC. As shown in Figure 7.5-c and 5-d, with a w/c ratio of 0.5, the adsorbed CNTs do not appear to form dense and thick agglomerations. For further understanding of the effect of the adsorbed CNTs, the surface density of the adsorbed CNTs, which is the number of CNTs attached per unit area of adsorptive OPC grain surface, was estimated using the spherical shape model (Taylor 1997, Sanahuja,

Dormieux et al. 2007). Assuming that all OPC particles were spherical, the typical particle size distribution function of OPC grains is given by

$$R(d'') = \exp\left(-\left(\frac{d''}{23.6}\right)^{0.9}\right) \quad 7.3$$

where R is the mass fraction of the grains with diameter greater than d'' (Osbaeck and Johansen 1989). On the basis of Eq. 7.2 the total surface area for particles smaller than a certain size threshold (ds) can be calculated by (Taylor 1997)

$$S' = 6\times10^{6}\times F\times\frac{\mathrm{d}R}{\mathrm{d}d''}\frac{1}{\rho d''} \quad 7.4$$

where S' is the surface area of particles with diameter equal to d'', F (typically equalling 1.13) is an empirical constant taking into account the shape of the particles, ρ = 3.15 is specific gravity of the OPC grains.

Using Eq. 7.4, the total surface area of the OPC grains with diameter less than 4 µm was calculated as 0.282 m^2/g, where OPC grains smaller than 2 µm were assumed to have an average diameter of 1 µm (Taylor 1997). Excluding the 15 % contribution to the surface area from gypsum, the adsorptive area was 0.24 m^2/g. Assuming that CNTs are cylinders with specific gravity of 2.6 g/cm^3 (Hwang, Ahn et al. 2006), diameter 9.5 nm and length 1-2 µm (Chen, Zou et al. 2014), the mass of a single tube (M_t) is 1.84 $\times10^{-16}$-3.68$\times10^{-16}$g. For the case of c/w = 20 and 2 (with adsorption rates of 2.7 and 0.5 mg/g respectively), the surface density of CNTs was calculated as 31-61 and 6-11 tubes/μm^2, respectively. These calculated surface densities coincided with the SEM observation in Figure 7.5, which also proved that the reduction of C_d in paste was mainly due to adsorption rather than agglomeration.

For the common OPC paste mix with c/w=2 (or w/c=0.5), the surface density of 6-11 tubes/ tubes/μm^2 corresponded to a thin layer of scattered CNTs on small OPC

grains (Figure 7.5-c, d). However, this surface density was still far higher than the projected surface density of dispersed CNTs which was obtained by evenly splitting the number of CNTs in a 1 µm cubic space into its 6 facets as 60 % C_d /M_t/6 =0.7-1.7 tubes/ µm^2. It is suggested here that the adsorbed CNTs distributed more densely than the dispersed CNTs but less densely than the CNT agglomerates. The distribution model of CNTs within OPC pastes is meaningful for understanding of the role of CNTs with regard to reinforcement (Chen, Zou et al. 2014, Zou, Chen et al. 2015). Moreover, it is vital for simulating hydration reactions in OPC paste (Knudsen 1984, Garboczi and Bentz 2001, Bernard, Ulm et al. 2003, Ye 2003, Ye, Lura et al. 2006) as it allows establishment of the initial particle packing model for fresh paste.

7.6. **Conclusions**

To resolve the question regarding the maximum amount of CNTs that can be dispersed in fresh pastes, a two-step investigation was conducted. The first step determined the maximum C_d in CNT-water suspension before mixing with OPC. It was found that C_d kept increasing with C_t to 0.9 wt % when C_t = 2.64 wt %. However, the degree of dispersion C_d/C_t dropped sharply to less than 50 % when C_t increased above 0.264 wt %, resulting in a significant amount of CNT agglomeration. Therefore, it is suggested that the upper limit for economical and effective use of CNTs is C_t = 0.264 wt % with a C_d/C_t around 90 %. The second step was to examine the stability of the CNT dispersions with different C_t in a simulated pore solution that represented the concentration of most ions in fresh OPC pastes. The results showed that the decrease in C_d/C_t for different C_t was less than 2 % per hour for at least 4 hours, indicating that the suspensions were stable within the common setting time of OPC pastes. After 4–16 hours, however, the suspensions transited into an unstable state and C_d/C_t began to decrease dramatically.

With regard to the question of CNT distribution in OPC paste, this study presents two major findings. Firstly, the existence of CNT-free zones in the CNT-OPC paste composite was addressed here in the CNT distribution models, where the CNT-free zones were caused by the hydrated grains in the fresh OPC paste. Secondly, the adsorption effect of the OPC grains was proposed and quantified based on an innovative centrifuge-based technique. It was observed that for common w/c ratios, about 0.5 mg of CNT was adsorbed by 1 g of OPC. This observation was quantified by SEM imaging demonstrating that only non-gypsum OPC grains with dimension < 4 um could adsorb the CNTs, due to the formation of hydration reaction products around these small OPC grains.

Combining these findings, a conceptual distribution model for CNTs in OPC paste is proposed. The model provides a quantification of the amount of dispersed, agglomerated and adsorbed CNTs in the matrix. The surface density of the adsorbed CNTs is also calculated as 6-11 CNTs per square micrometre. This model can serve as a starting point for establishing or refining models depicting the effect of CNTs on reinforcement and hydration in CNT-OPC paste composites.

CHAPTER 8. CONCLUSIONS AND RECOMMENDATIONS

Although OPC paste is widely used in the construction industry, its weak tensile strength to some extent limits its application. CNTs, on the other hand, have outstanding mechanical properties with a tensile strength of 63 GPa and Young's modulus of 1 TPa, making it a candidate as nanoscale reinforcement in OPC paste. Past research studies have reported improved mechanical and electrical properties of CNT–OPC paste composites, which show future promise for practical civil engineering applications.

In this study, recent research studies in developing CNT–OPC paste composites were comprehensively reviewed. Highlighted were the considerable efforts that have been made in study of the fabrication, hydration, porosity and transport properties of CNT–OPC paste composites. As a further development, the studies presented in this thesis were conducted to provide better understanding in the areas of uniform dispersion of CNTs within the OPC paste, durability, impact, fatigue properties and the theoretical modelling of CNT–OPC paste interaction.

8.1. Key research findings

(1) The interaction energy between ionic surfactants and SWCNTs was calculated using MM simulation to investigate the effects of molecular characteristics of the surfactants on CNT dispersion. Six types of surfactant were studied in the simulation, namely SDS, SDBS, SOBS, SBBS and SC. Interaction energy was utilized to discover how the energy preference for morphologies changed as the surface density increased. The results indicates that the preferred

aggregation morphology for surfactants with high linearity, such as SDS, shifted from parallel to hemi-cylindrical and then to cylindrical when the number of surfactants in the aggregation increased. In contrast, this preference for less linear surfactants such as SC and SBBS only transited between two aggregation morphologies. The saturation surface densities for the SDS, SDBS-2 and SC were found to be around 9.3, 11.3 and 6.3 molecules/nm^2 respectively, and the interaction energy at saturation decreased in the order SC, SDBS-2, SDS. Also, the results suggested that for surfactants with linear alkyl chains, the longer the chains and the closer the hydrophilic group to the ends of the chain, the higher generally was the interaction energy. The simulation results matched well with some experimental observations using TEM and UV spectrometer.

(2) Three OPC additives were used as surfactants to non-covalently disperse MWCNTs in saturated $Ca(OH)_2$ solution. The dispersion efficacy of the surfactants was characterized using visual observation, UV-vis spectrum and TEM imaging. Also, MD simulation was conducted to study the interaction energy between the surfactants and the MWCNTs. The calculated interaction energy was used with a CNT agglomerating model to study the agglomeration process of MWCNTs in suspension. UV-vis spectrometry and zeta potential measurements indicated that the dispersion of CNTs using MA was instable whereas the dispersions using SL and NC were semi-stable. Hydrodynamic size analysis and TEM observation indicated that SL could suspend smaller CNTs bundles than NC. The bundle size of both SL and NC was found to be smaller than 7. A theoretical CNT agglomerating model was developed to simulate the agglomeration process. Using the interaction energy obtained in

the MD simulation, the agglomerating model predicted CNT bundle sizes that matched experimental observations. The model also suggested that CNTs tended to form small parallel bundles (containing fewer than 6 tubes) before large 3D lump-like agglomerates.

(3) There has been very limited research directed towards simulating and understanding the reinforcing effect of CNTs. In this study, a theoretical framework with supporting experiments was developed to address this issue. The distribution of CNT lengths and the concentration of dispersed CNTs were characterized using scanning electron microscopy images and UV–vis spectra. After ultrasonication, the length of CNTs was found to follow log-normal distributions that showed a shortening effect. The concentration of dispersed CNT increased with UE but reached a plateau after about 250 J/ml. The distribution of CNT lengths and the concentration of dispersed CNTs were incorporated into a micromechanics-based model to simulate the crack bridging behaviour of CNTs. The results showed that the distribution of CNT lengths lad to better estimation of reinforcing effects than did the average length. Furthermore, for unit volume of dispersed CNTs, the reinforcing efficiency decreased monotonically with increased ultrasonication. From the proposed model, the predicted optimal UE (89 J/ml) for reinforcing was found before the dispersion plateau was reached

(4) The engineering properties of CNT–OPC pastes were investigated with varied UE and CNT concentration. It was found that UE could effectively improve the aqueous dispersion of surface functionalized CNTs with the aid of a PC. A PC to CNT mass ratio of 8 was recommended to ensure effective dispersion of CNTs and to maintain the workability of CNT–OPC pastes under sufficient

ultrasonication. Furthermore, the mechanical property results of the hardened pastes obtained from pre-notched beam tests revealed the existence of an optimal UE for achieving mechanically superior CNT–OPC pastes, which was found to be 50 J/mL per unit CNT to suspension weight ratio. The Young's modulus E, flexural strength σf, and fracture energy GF of CNT–OPC pastes were significantly improved compared to plain OPC pastes. These results clearly demonstrated the reinforcing effect of CNTs on OPC pastes because they decreased the porosity and increased the crack bridging capacity of OPC pastes at nanoscale level, an effect that would be complementary to conventional microfibres in reinforcing OPC pastes.

(5) CNTs were dispersed using combined polycarboxylate superplasticizers and an ultrasonication technique to investigate the dispersion and distribution of CNTs in fresh OPC paste. The maximum dispersed CNT concentration and its stability in fresh OPC paste were investigated via UV-vis spectrometry and simulated OPC paste pore solution. The results suggested an upper limit of 0.264 wt % for CNT addition into water before mixing with OPC grains, and the dispersion was found to be stable for at least 4 hours. The adsorption of CNTs on OPC grains was proposed as a critical phenomenon that affected the distribution of CNTs in fresh OPC pastes and it was investigated using a new centrifuge-based method. It was observed that about 0.5 mg of CNTs per gram of OPC grains was adsorbed in typical fresh OPC pastes. On the basis of these results, a conceptual model was proposed for the dispersion and distribution of CNTs in fresh OPC paste.

8.2. **Recommended fabrication parameter for optimal reinforcing effects**

As the ultimate outcome in accordance with the goal of this PhD, the research suggests the following parameters for the fabrication CNT-OPC paste:

Type of surfactant

polycarboxylate-based superplasticizers

Surfactant to CNT mass ratio

8, excluding the surfactants added to improve workability

Type of CNT

MWCNTs with a small amount of –COOH groups attached

Aspect ratio of CNTs

Initial aspect ratio of 100-500.

CNT concentration

0.528 wt % to 0.264 wt % of the water

Ultrasonication energy

60 KJ/g of CNTs or when C_d/C_t =75-80 %

Mixing method

High shear mixing (ASTM standard C1738)

Setting time

Less than 4 hours

8.3. **Recommended techniques for characterization of CNT-OPC pastes composite**

Since no standard characterization method has been developed for many of the important parameters during the fabrication and investigation of CNT-OPC pastes, some of the validated techniques in this study are recommended and listed below.

Concentration of dispersed CNT in the aqueous suspension before mixing with OPC:

UV-vis spectrometry is suggested. An extinction coefficient between 41.14 ml/mg/cm and 46.00 ml/mg/cm can be used for approximate estimation.

Dispersed CNT concentration after mixing with OPC

After mixing, centrifuge the mixture with 3000g for 5 mins to squeeze out the pore solution. Use UV-vis spectrometry to measure the dispersed CNT concentration in that pore solution.

Length distribution of CNTs

Press a small drop of CNT suspension between two silicon wafers and then evaporate the water. Separate the two piece of silicon wafer and then observe under SEM for clear measurement of the length of CNTs.

Stability of CNT dispersion in fresh OPC paste

An artificial mixture is suggested to simulate the concentration of ions in pore solution of fresh OPC paste. The recipe for this mixture can be found in Table 7.1.

REFERENCES

Arnold, M. S., J. Suntivich, S. I. Stupp and M. C. Hersam (2008). "Hydrodynamic Characterization of Surfactant Encapsulated Carbon Nanotubes Using an Analytical Ultracentrifuge." Acs Nano **2**(11): 2291-2300.

AS 3972 (2010). "General purpose and blended cements."

ASTM C192 / C192M - 13a "Standard Practice for Making and Curing Concrete Test Specimens in the Laboratory.".

ASTM C1738 - 11a "Standard Practice for High-Shear Mixing of Hydraulic Cement Paste.".

Atesok, G., P. Somasundaran and L. Morgan (1988). "Adsorption properties of Ca 2+ on Na-kaolinite and its effect on flocculation using polyacrylamides." Colloids and surfaces **32**: 127-138.

Atkin, R., V. S. J. Craig, E. J. Wanless and S. Biggs (2003). "The influence of chain length and electrolyte on the adsorption kinetics of cationic surfactants at the silica-aqueous solution interface." Journal of Colloid and Interface Science **266**(2): 236-244.

Atkin, R., V. S. J. Craig, E. J. Wanless and S. Biggs (2003). "Mechanism of cationic surfactant adsorption at the solid-aqueous interface." Advances in Colloid and Interface Science **103**(3): 219-304.

Backes, C., J. M. Englert, N. Bernhard, F. Hauke and A. Hirsch (2010). "Optical Visualization of Carbon Nanotubes-a Unifying Linkage Between Microscopic and Spectroscopic Characterization Techniques." Small **6**(18): 1968-1973.

Badaire, S., P. Poulin, M. Maugey and C. Zakri (2004). "In situ measurements of nanotube dimensions in suspensions by depolarized dynamic light scattering." Langmuir **20**(24): 10367-10370.

Bai, J. B. and A. Allaoui (2003). "Effect of the length and the aggregate size of MWNTs on the improvement efficiency of the mechanical and electrical properties of nanocomposites--experimental investigation." Composites Part A: Applied Science and Manufacturing **34**(8): 689-694.

Bai, Y., I. S. Park, S. J. Lee, T. S. Bae, F. Watari, M. Uo and M. H. Lee (2011). "Aqueous dispersion of surfactant-modified multiwalled carbon nanotubes and their application as an antibacterial agent." Carbon **49**(11): 3663-3671.

Bakshi, S. R. and A. Agarwal (2011). "An analysis of the factors affecting strengthening in carbon nanotube reinforced aluminum composites." Carbon **49**(2): 533-544.

Bandyopadhyaya, R., E. Nativ-Roth, O. Regev and R. Yerushalmi-Rozen (2002). "Stabilization of individual carbon nanotubes in aqueous solutions." Nano Letters **2**(1): 25-28.

Baoguo, H., Y. Xun and K. Eil (2009). "A self-sensing carbon nanotube/cement composite for traffic monitoring." Nanotechnology **20**(44): 445501.

Baskaran, D., J. W. Mays and M. S. Bratcher (2005). "Noncovalent and nonspecific molecular interactions of polymers with multiwalled carbon nanotubes." Chemistry of Materials **17**(13): 3389-3397.

Bergin, S. D., V. Nicolosi, H. Cathcart, M. Lotya, D. Rickard, Z. Sun, W. J. Blau and J. N. Coleman (2008). "Large populations of individual nanotubes in surfactant-based dispersions without the need for ultracentrifugation." The Journal of Physical Chemistry C **112**(4): 972-977.

Bernard, O., F.-J. Ulm and E. Lemarchand (2003). "A multiscale micromechanics-hydration model for the early-age elastic properties of cement-based materials." Cement and Concrete Research **33**(9): 1293-1309.
Bhattacharyya, S., C. Sinturel, O. Bahloul, M.-L. Saboungi, S. Thomas and J.-P. Salvetat (2008). "Improving reinforcement of natural rubber by networking of activated carbon nanotubes." Carbon **46**(7): 1037-1045.
Blanch, A. J., C. E. Lenehan and J. S. Quinton (2010). "Optimizing surfactant concentrations for dispersion of single-walled carbon nanotubes in aqueous solution." The Journal of Physical Chemistry B **114**(30): 9805-9811.
Blanch, A. J., C. E. Lenehan and J. S. Quinton (2010). "Optimizing Surfactant Concentrations for Dispersion of Single-Walled Carbon Nanotubes in Aqueous Solution." Journal of Physical Chemistry B **114**(30): 9805-9811.
Blanch, A. J., C. E. Lenehan and J. S. Quinton (2011). "Parametric analysis of sonication and centrifugation variables for dispersion of single walled carbon nanotubes in aqueous solutions of sodium dodecylbenzene sulfonate." Carbon **49**(15): 5213-5228.
Buffle, J. and G. Leppard (1995). "Characterization of aquatic colloids and macromolecules. 1. Structure and behavior of colloidal material." Environmental science & technology **29**(9): 2169-2175.
Calvaresi, M., M. Dallavalle and F. Zerbetto (2009). "Wrapping Nanotubles with Micelles, Hemimicelles, and Cylindrical Micelles." Small **5**(19): 2191-2198.
Campillo, I., J. S. Dolado and A. Porro (2003). High-performance nanostructured materials for construction. 1st International Symposium on Nanotechnology in Construction, Paisley, Scotland, Cambridge England : Royal Society of Chemistry
Cardenas, J. F. and M. Glerup (2006). "The influence of surfactants on the distribution of the radial breathing modes of single walled carbon nanotubes." Nanotechnology **17**(20): 5212-5215.
Chaipanich, A., T. Nochaiya, W. Wongkeo and P. Torkittikul (2010). "Compressive strength and microstructure of carbon nanotubes-fly ash cement composites." Materials Science and Engineering: A **527**(4-5): 1063-1067.
ChemicalTradingGuide (2012). Naphthalenesulfonic acid,polymer with formaldehyde,calcium salt (CAS No. 37293-74-6).
Chemwatch (2008). Rheobuild 716LR Chemwatch Material Safety Data Sheet.
Chemwatch (2009). BASF Micro Air 905 Chemwatch Material Safety Data Sheet.
Chen, S., F. Collins, A. Macleod, Z. Pan, W. Duan and C. Wang (2011). "Carbon nanotube–cement composites: A retrospect." The IES Journal Part A: Civil & Structural Engineering **4**(4): 254-265.
Chen, S. J., B. Zou, F. Collins, X. L. Zhao, M. Majumber and W. H. Duan (2014). "Predicting the influence of ultrasonication energy on the reinforcing efficiency of carbon nanotubes." Carbon **77**(0): 1-10.
Chen, S. J., B. Zou, F. Collins, X. L. Zhao, M. Majumber and W. H. Duan (2014). "Predicting the influence of ultrasonication energy on the reinforcing efficiency of carbon nanotubes." Carbon **77**: 1-10.
Chen, S. J., B. Zou, F. Collins, X. L. Zhao, M. Majumber, C. M. Wang and W. H. Duan (unpublished). "Stability and bundling of surfactant-dispersed multi-walled carbon nanotubes in alkaline environment: Experimental and a Molecular Dynamics simulations based bundle growth model ".
Chen, W., J. Tu, L. Wang, H. Gan, Z. Xu and X. Zhang (2003). "Tribological application of carbon nanotubes in a metal-based composite coating and composites." Carbon **41**(2): 215-222.

Chen, X. L. and Y. J. Liu (2004). "Square representative volume elements for evaluating the effective material properties of carbon nanotube-based composites." Computational Materials Science **29**(1): 1-11.
Chew, K.-K., K.-L. Low, S. H. Sharif Zein, D. S. McPhail, L.-C. Gerhardt, J. A. Roether and A. R. Boccaccini (2011). "Reinforcement of calcium phosphate cement with multi-walled carbon nanotubes and bovine serum albumin for injectable bone substitute applications." Journal of the mechanical behavior of biomedical materials **4**(3): 331-339.
Churakov, S. V. (2008). "Hydrogen bond connectivity in jennite from ab initio simulations." Cement and Concrete Research **38**(12): 1359-1364.
Churakov, S. V. (2009). "Structural position of H2O molecules and hydrogen bonding in anomalous 11 angstrom tobermorite." American Mineralogist **94**(1): 156-165.
Clark, M. D. and R. Krishnamoorti (2009). "Dispersion of functionalized multiwalled carbon nanotubes." The Journal of Physical Chemistry C **113**(49): 20861-20868.
Coleman, J. N., U. Khan, W. J. Blau and Y. K. Gun'ko (2006). "Small but strong: A review of the mechanical properties of carbon nanotube-polymer composites." Carbon **44**(9): 1624-1652.
Coleman, J. N., U. Khan, W. J. Blau and Y. K. Gun'ko (2006). "Small but strong: a review of the mechanical properties of carbon nanotube–polymer composites." Carbon **44**(9): 1624-1652.
Collins, F., J. Lambert and W. H. Duan (2012). "The influences of admixtures on the dispersion, workability, and strength of carbon nanotube-OPC paste mixtures." Cement & Concrete Composites **34**(2): 201-207.
Collins, F., J. Lambert and W. H. Duan (2012). "The influences of admixtures on the dispersion, workability, and strength of carbon nanotube–OPC paste mixtures." Cement and Concrete Composites **34**(2): 201-207.
Conboy, J. C., M. C. Messmer and G. L. Richmond (1997). "Dependence of alkyl chain conformation of simple ionic surfactants on head group functionality as studied by vibrational sum-frequency spectroscopy." Journal of Physical Chemistry B **101**(34): 6724-6733.
Connor, P. and R. H. Ottewill (1971). "ADSORPTION OF CATIONIC SURFACE ACTIVE AGENTS ON POLYSTYRENE SURFACES." Journal of Colloid and Interface Science **37**(3): 642-&.
Cosgrove, T. (2010). Colloid science: principles, methods and applications, John Wiley & Sons.
Crouch, J. D. I. a. S. R. (1988). Spectrochemical analysis, Prentice Hall.
Cwirzen, A., K. Habermehl-Cwirzen, A. G. Nasibulin, E. I. Kaupinen, P. R. Mudimela and V. Penttala (2009). "SEM/AFM studies of cementitious binder modified by MWCNT and nano-sized Fe needles." Materials Characterization **60**(7): 735-740.
Cwirzen, A., K. Habermehl-Cwirzen, A. G. Nasibulin, E. I. Kaupinen, P. R. Mudimela and V. Penttala (2009). "SEW/AFM studies of cementitious binder modified by MWCNT and nano-sized Fe needles." Materials Characterization **60**(7): 735-740.
Cwirzen, A., K. Habermehl-Cwirzen and V. Penttala (2008). "Surface decoration of carbon nanotubes and mechanical properties of cement/carbon nanotube composites." Advances in cement research **20**(2): 65-73.
Cwirzen, A., K. Habermehl-Cwirzen, D. Shandakov, L. I. Nasibulina, A. G. Nasibulin, P. R. Mudimela, E. I. Kauppinen and V. Penttala (2009). "Properties of high yield synthesised carbon nano fibres/Portland cement composite." Advances in Cement Research **21**(4): 141-146.

Donaldson, K., R. Aitken, L. Tran, V. Stone, R. Duffin, G. Forrest and A. Alexander (2006). "Carbon nanotubes: A review of their properties in relation to pulmonary toxicology and workplace safety." Toxicological Sciences **92**(1): 5-22.
Duan, W. H., Q. Wang and F. Collins (2011). "Dispersion of carbon nanotubes with SDS surfactants: a study from a binding energy perspective." Chemical Science **2**(7): 1407-1413.
Duan, W. H., Q. Wang, K. M. Liew and X. Q. He (2007). "Molecular mechanics modeling of carbon nanotube fracture." Carbon **45**(9): 1769-1776.
Duque, J. G., C. G. Densmore and S. K. Doorn (2010). "Saturation of Surfactant Structure at the Single-Walled Carbon Nanotube Surface." Journal of the American Chemical Society **132**(45): 16165-16175.
Dyke, C. A. and J. M. Tour (2004). "Overcoming the Insolubility of Carbon Nanotubes Through High Degrees of Sidewall Functionalization." Chemistry - A European Journal **10**(4): 812-817.
Eda, G., G. Fanchini, A. Kanwal and M. Chhowalla (2008). "Bundling dynamics of single walled carbon nanotubes in aqueous suspensions." Journal of Applied Physics **103**(9).
Fan, A. X., P. Somasundaran and N. J. Turro (1997). "Adsorption of alkyltrimethylammonium bromides on negatively charged alumina." Langmuir **13**(3): 506-510.
Faucon, P., J. M. Delaye, J. Virlet, J. F. Jacquinot and F. Adenot (1997). "Study of the structural properties of the C-S-H(I) by molecular dynamics simulation." Cement and Concrete Research **27**(10): 1581-1590.
Feuston, B. P. and S. H. Garofalini (1989). "TOPOLOGICAL AND BONDING DEFECTS IN VITREOUS SILICA SURFACES." Journal of Chemical Physics **91**(1): 564-570.
Frømyr, T. R., F. K. Hansen and T. Olsen (2012). "The Optimum Dispersion of Carbon Nanotubes for Epoxy Nanocomposites: Evolution of the Particle Size Distribution by Ultrasonic Treatment." Journal of Nanotechnology **2012**: 545930.
Ganß, M., B. K. Satapathy, M. Thunga, R. Weidisch, P. Pötschke and D. Jehnichen (2008). "Structural interpretations of deformation and fracture behavior of polypropylene/multi-walled carbon nanotube composites." Acta Materialia **56**(10): 2247-2261.
Gao, Y.-C., Y.-W. Mai and B. Cotterell (1988). "Fracture of fiber-reinforced materials." Zeitschrift für angewandte Mathematik und Physik ZAMP **39**(4): 550-572.
Garboczi, E. and D. Bentz (2001). "The effect of statistical fluctuation, finite size error, and digital resolution on the phase percolation and transport properties of the NIST cement hydration model." Cement and Concrete Research **31**(10): 1501-1514.
Gates, T. S., G. M. Odegard, S. J. V. Frankland and T. C. Clancy (2005). "Computational materials: Multi-scale modeling and simulation of nanostructured materials." Composites Science and Technology **65**(15-16): 2416-2434.
Ghods, P., O. Isgor, G. McRae and T. Miller (2009). "The effect of concrete pore solution composition on the quality of passive oxide films on black steel reinforcement." Cement and Concrete Composites **31**(1): 2-11.
Ghosh, S., S. M. Bachilo and R. B. Weisman (2010). "Advanced sorting of single-walled carbon nanotubes by nonlinear density-gradient ultracentrifugation." Nature Nanotechnology **5**(6): 443-450.
Giordani, S., S. D. Bergin, V. Nicolosi, S. Lebedkin, M. M. Kappes, W. J. Blau and J. N. Coleman (2006). "Debundling of single-walled nanotubes by dilution: observation of large populations of individual nanotubes in amide solvent dispersions." The Journal of Physical Chemistry B **110**(32): 15708-15718.

Girifalco, L., M. Hodak and R. S. Lee (2000). "Carbon nanotubes, buckyballs, ropes, and a universal graphitic potential." Physical Review B **62**(19): 13104-13110
Gmira, A., M. Zabat, R. J. M. Pellenq and H. Van Damme (2004). "Microscopic physical basis of the poromechanical behavior of cement-based materials." Materials and Structures **37**(265): 3-14.
Godara, A., L. Mezzo, F. Luizi, A. Warrier, S. V. Lomov, A. Van Vuure, L. Gorbatikh, P. Moldenaers and I. Verpoest (2009). "Influence of carbon nanotube reinforcement on the processing and the mechanical behaviour of carbon fiber/epoxy composites." Carbon **47**(12): 2914-2923.
Gołaszewski, J. and J. Szwabowski (2004). "Influence of superplasticizers on rheological behaviour of fresh cement mortars." Cement and Concrete Research **34**(2): 235-248.
Gougar, M., B. Scheetz and D. Roy (1996). "Ettringite and C-S-H Portland cement phases for waste ion immobilization: A review." Waste Management **16**(4): 295-303.
Goyanes, S., G. R. Rubiolo, A. Salazar, A. Jimeno, M. A. Corcuera and I. Mondragon (2007). "Carboxylation treatment of multiwalled carbon nanotubes monitored by infrared and ultraviolet spectroscopies and scanning probe microscopy." Diamond and Related Materials **16**(2): 412-417.
Grace (2007). WRDA GWA Water-reducing Admixture.
Green, A. A., M. C. Duch and M. C. Hersam (2009). "Isolation of Single-Walled Carbon Nanotube Enantiomers by Density Differentiation." Nano Research **2**(1): 69-77.
Grossiord, N., O. Regev, J. Loos, J. Meuldijk and C. E. Koning (2005). "Time-dependent study of the exfoliation process of carbon nanotubes in aqueous dispersions by using UV-visible spectroscopy." Analytical chemistry **77**(16): 5135-5139.
Grossiord, N., P. van der Schoot, J. Meuldijk and C. E. Koning (2007). "Determination of the surface coverage of exfoliated carbon nanotubes by surfactant molecules in aqueous solution." Langmuir **23**(7): 3646-3653.
Han, B., X. Yu and J. Ou (2011). Multifunctional and smart carbon nanotube reinforced cement-based materials. Nanotechnology in Civil Infrastructure, Springer: 1-47.
Han, B. G., X. Yu and J. P. Ou (2010). "Effect of water content on the piezoresistivity of MWNT/cement composites." Journal of Materials Science **45**(14): 3714-3719.
He, X. B., O. Guvench, A. I. MacKerell and M. L. Klein (2010). "Atomistic Simulation Study of Linear Alkylbenzene Sulfonates at the Water/Air Interface." Journal of Physical Chemistry B **114**(30): 9787-9794.
Hertel, T., A. Hagen, V. Talalaev, K. Arnold, F. Hennrich, M. Kappes, S. Rosenthal, J. McBride, H. Ulbricht and E. Flahaut (2005). "Spectroscopy of Single- and Double-Wall Carbon Nanotubes in Different Environments." Nano Letters **5**(3): 511-514.
Hilding, J., E. A. Grulke, Z. George Zhang and F. Lockwood (2003). "Dispersion of carbon nanotubes in liquids." Journal of Dispersion Science and Technology **24**(1): 1-41.
Hilding, J., E. A. Grulke, Z. G. Zhang and F. Lockwood (2003). "Dispersion of Carbon Nanotubes in Liquids." Journal of Dispersion Science and Technology **24**(1): 1 - 41.
Hillerborg, A. (1985). "The theoretical basis of a method to determine the fracture energyG F of concrete." Materials and Structures **18**(4): 291-296.
Hone, J., M. Whitney, C. Piskoti and A. Zettl (1999). "Thermal conductivity of single-walled carbon nanotubes." Physical Review B **59**(4): R2514.
Hunashyal, A., S. Lohitha, S. Quadri and N. Banapurmath (2011). "Experimental investigation of the effect of carbon nanotubes and carbon fibres on the behaviour of

plain cement composite beams." The IES Journal Part A: Civil & Structural Engineering **4**(1): 29-36.
Hwang, Y. J., Y. C. Ahn, H. S. Shin, C. G. Lee, G. T. Kim, H. S. Park and J. K. Lee (2006). "Investigation on characteristics of thermal conductivity enhancement of nanofluids." Current Applied Physics **6**(6): 1068-1071.
Inam, F., T. Vo, J. P. Jones and X. Lee (2012). "Effect of carbon nanotube lengths on the mechanical properties of epoxy resin: An experimental study." Journal of Composite Materials **47**(19): 2321-2330.
Islam, M., E. Rojas, D. Bergey, A. Johnson and A. Yodh (2003). "High weight fraction surfactant solubilization of single-wall carbon nanotubes in water." Nano Letters **3**(2): 269-273.
Islam, M. F., E. Rojas, D. M. Bergey, A. T. Johnson and A. G. Yodh (2003). "High Weight Fraction Surfactant Solubilization of Single-Wall Carbon Nanotubes in Water." Nano Letters **3**(2): 269-273.
Israelachvili, J. N. (2011). Intermolecular and surface forces, Academic Press.
Israelachvili, J. N. (2011). Intermolecular and surface forces. Burlington, MA, Academic Press.
Israelachvili, J. N. (2011). Intermolecular and surface forces: revised third edition, Academic press.
Jiang, J., G. Oberdörster and P. Biswas (2009). "Characterization of size, surface charge, and agglomeration state of nanoparticle dispersions for toxicological studies." Journal of Nanoparticle Research **11**(1): 77-89.
Jiang, X., T. L. Kowald, T. Staedler, R. H. F. Trettin, Y. de Miguel, A. Porro and P. Bartos (2006). Carbon nanotubes as a new reinforcement material for modern cement-based binders. NICOM2 (Proceedings of the Second International Symposium on Nanotechnology and Construction), Bilbao, Spain.
Jurasin, D., I. Habus and N. Filipovic-Vincekovic (2010). "Role of the alkyl chain number and head groups location on surfactants self-assembly in aqueous solutions." Colloids and Surfaces a-Physicochemical and Engineering Aspects **368**(1-3): 119-128.
Kahn, M. G. C., S. Banerjee and S. S. Wong (2002). "Solubilization of oxidized single-walled carbon nanotubes in organic and aqueous solvents through organic derivatization." Nano Letters **2**(11): 1215-1218.
Kalinichev, A. G. and R. J. Kirkpatrick (2002). "Molecular dynamics modeling of chloride binding to the surfaces of calcium hydroxide, hydrated calcium aluminate, and calcium silicate phases." Chemistry of Materials **14**(8): 3539-3549.
Kalinichev, A. G., J. W. Wang and R. J. Kirkpatrick (2007). "Molecular dynamics modeling of the structure, dynamics and energetics of mineral-water interfaces: Application to cement materials." Cement and Concrete Research **37**(3): 337-347.
Kendall, K., A. Howard, J. Birchall, P. Pratt, B. Proctor and S. Jefferis (1983). "The relation between porosity, microstructure and strength, and the approach to advanced cement-based materials [and discussion]." Philosophical Transactions of the Royal Society of London. Series A, Mathematical and Physical Sciences **310**(1511): 139-153.
Knudsen, T. (1984). "The dispersion model for hydration of Portland cement I. General concepts." Cement and Concrete Research **14**(5): 622-630.
Ko, F., Y. Gogotsi, A. Ali, N. Naguib, H. Ye, G. L. Yang, C. Li and P. Willis (2003). "Electrospinning of Continuous Carbon Nanotube-Filled Nanofiber Yarns." Advanced Materials **15**(14): 1161-1165.
Konsta-Gdoutos, M. S., Z. S. Metaxa and S. P. Shah (2010). "Highly dispersed carbon nanotube reinforced cement based materials." Cement and Concrete Research **40**(7): 1052-1059.

Konsta-Gdoutos, M. S., Z. S. Metaxa and S. P. Shah (2010). "Multi-scale mechanical and fracture characteristics and early-age strain capacity of high performance carbon nanotube/cement nanocomposites." Cement and Concrete Composites **32**(2): 110-115.
Kowald, T. and R. Trettin (2004). Influence of Surface-Modified Carbon Nanotubes on Ultra-High Performance Concrete. . Proceedings of International Symposium on Ultra High Performance Concrete. Z. Bittnar, P. J. M. Bartos, J. Němeček, V. Šmilauer and J. Zeman. Kassel, Germany, Kassel university press Gmbh: 195-202.
Kowald, T. and R. Trettin (2009). Improvement of Cementitious Binders by Multi-Walled Carbon Nanotubes. Nanotechnology in Construction 3. Z. Bittnar, P. J. M. Bartos, J. Němeček, V. Šmilauer and J. Zeman, Springer Berlin Heidelberg: 261-266.
Krause, B., M. Mende, P. Potschke and G. Petzold (2010). "Dispersability and particle size distribution of CNTs in an aqueous surfactant dispersion as a function of ultrasonic treatment time." Carbon **48**(10): 2746-2754.
Krause, B., M. Mende, P. Pötschke and G. Petzold (2010). "Dispersability and particle size distribution of CNTs in an aqueous surfactant dispersion as a function of ultrasonic treatment time." Carbon **48**(10): 2746-2754.
Krause, B., G. Petzold, S. Pegel and P. Pötschke (2009). "Correlation of carbon nanotube dispersability in aqueous surfactant solutions and polymers." Carbon **47**(3): 602-612.
Lee, H. H., U. Sang Shin, J. H. Lee and H. W. Kim (2011). "Biomedical nanocomposites of poly (lactic acid) and calcium phosphate hybridized with modified carbon nanotubes for hard tissue implants." Journal of Biomedical Materials Research Part B: Applied Biomaterials **98**(2): 246-254.
Lee, J. U., J. Huh, K. H. Kim, C. Park and W. H. Jo (2007). "Aqueous suspension of carbon nanotubes via non-covalent functionalization with oligothiophene-terminated poly (ethylene glycol)." Carbon **45**(5): 1051-1057.
Legrand, C. and E. Wirquin (1994). "Study of the strength of very young concrete as a function of the amount of hydrates formed—influence of superplasticizer." Materials and Structures **27**(2): 106-109.
Li, B., L. Y. Li, B. B. Wang and C. Y. Li (2009). "Alternating patterns on single-walled carbon nanotubes." Nature Nanotechnology **4**(6): 358-362.
Li, G. Y., P. M. Wang and X. Zhao (2005). "Mechanical behavior and microstructure of cement composites incorporating surface-treated multi-walled carbon nanotubes." Carbon **43**(6): 1239-1245.
Li, G. Y., P. M. Wang and X. Zhao (2007). "Pressure-sensitive properties and microstructure of carbon nanotube reinforced cement composites." Cement and Concrete Composites **29**(5): 377-382.
Li, G. Y., P. M. Wang and X. H. Zhao (2005). "Mechanical behavior and microstructure of cement composites incorporating surface-treated multi-walled carbon nanotubes." Carbon **43**(6): 1239-1245.
Li, K. and S. Saigal (2007). "Micromechanical modeling of stress transfer in carbon nanotube reinforced polymer composites." Materials Science and Engineering a-Structural Materials Properties Microstructure and Processing **457**(1-2): 44-57.
Li, L. and A. A. Sagues (2001). "Chloride corrosion threshold of reinforcing steel in alkaline solutions - Open-circuit immersion tests." Corrosion **57**(1): 19-28.
Li, V. C. (1992). "Postcrack scaling relations for fiber reinforced cementitious composites." Journal of Materials in Civil Engineering **4**(1): 41-57.
Li, Y. J., J. Reeve, Y. L. Wang, R. K. Thomas, J. B. Wang and H. K. Yan (2005). "Microcalorimetric study on micellization of nonionic surfactants with a benzene ring

or adamantane in their hydrophobic chains." Journal of Physical Chemistry B **109**(33): 16070-16074.
Li, Z., G. Luo, W. Zhou, F. Wei, R. Xiang and Y. Liu (2006). "The quantitative characterization of the concentration and dispersion of multi-walled carbon nanotubes in suspension by spectrophotometry." Nanotechnology **17**(15): 3692.
Lin, S. C. and D. Blankschtein (2010). "Role of the Bile Salt Surfactant Sodium Cholate in Enhancing the Aqueous Dispersion Stability of Single-Walled Carbon Nanotubes: A Molecular Dynamics Simulation Study." Journal of Physical Chemistry B **114**(47): 15616-15625.
Liu, J., A. G. Rinzler, H. J. Dai, J. H. Hafner, R. K. Bradley, P. J. Boul, A. Lu, T. Iverson, K. Shelimov, C. B. Huffman, F. Rodriguez-Macias, Y. S. Shon, T. R. Lee, D. T. Colbert and R. E. Smalley (1998). "Fullerene pipes." Science **280**(5367): 1253-1256.
Liu, Y., L. Gao, S. Zheng, Y. Wang, J. Sun, H. Kajiura, Y. Li and K. Noda (2007). "Debundling of single-walled carbon nanotubes by using natural polyelectrolytes." Nanotechnology **18**(36): 365702.
Liu, Y., L. Yu, S. Zhang, J. Yuan, L. Shi and L. Zheng (2010). "Dispersion of multiwalled carbon nanotubes by ionic liquid-type Gemini imidazolium surfactants in aqueous solution." Colloids and Surfaces A: Physicochemical and Engineering Aspects **359**(1–3): 66-70.
Liu, Y. H., L. Yu, S. H. Zhang, J. Yuan, L. J. Shi and L. Q. Zheng (2010). "Dispersion of multiwalled carbon nanotubes by ionic liquid-type Gemini imidazolium surfactants in aqueous solution." Colloids and Surfaces a-Physicochemical and Engineering Aspects **359**(1-3): 66-70.
Liu, Y. J. and X. L. Chen (2003). "Evaluations of the effective material properties of carbon nanotube-based composites using a nanoscale representative volume element." Mechanics of Materials **35**(1-2): 69-81.
Lu, K., R. Lago, Y. Chen, M. Green, P. Harris and S. Tsang (1996). "Mechanical damage of carbon nanotubes by ultrasound." Carbon **34**(6): 814-816.
Lucas, A., C. Zakri, M. Maugey, M. Pasquali, P. v. d. Schoot and P. Poulin (2009). "Kinetics of nanotube and microfiber scission under sonication." The Journal of Physical Chemistry C **113**(48): 20599-20605.
Luo, J., Z. Duan, T. Zhao and Q. Li (2011). "Effect of Multi-Wall Carbon Nanotube on Fracture Mechanical Property of Cement-Based Composite." Advanced Materials Research **146**: 581-584.
Luo, J., Z. Duan, T. Zhao and Q. Li (2011). "Hybrid Effect of Carbon Fiber on Piezoresistivity of Carbon Nanotube Cement-Based Composite." Advanced Materials Research **143**: 639-643.
Luo, J. L., Z. D. Duan and H. Li (2009). "The influence of surfactants on the processing of multi-walled carbon nanotubes in reinforced cement matrix composites." Physica Status Solidi a-Applications and Materials Science **206**(12): 2783-2790.
Ma, J. G., B. J. Boyd and C. J. Drummond (2006). "Positional isomers of linear sodium dodecyl benzene sulfonate: Solubility, self-assembly, and air/water interfacial activity." Langmuir **22**(21): 8646-8654.
Mackiewicz, N., G. Surendran, H. Remita, B. Keita, G. Zhang, L. Nadjo, A. Hagege, E. Doris and C. Mioskowski (2008). "Supramolecular self-assembly of amphiphiles on carbon nanotubes: A versatile strategy for the construction of CNT/metal nanohybrids, application to electrocatalysis." Journal of the American Chemical Society **130**(26): 8110-+.
Makar, J. (2011). The Effect of SWCNT and Other Nanomaterials on Cement Hydration and Reinforcement, Berlin; Heidelberg:Springer: 103-130.

Makar, J. (2011). The Effect of SWCNT and Other Nanomaterials on Cement Hydration and Reinforcement. Nanotechnology in Civil Infrastructure, Berlin; Heidelberg:Springer 103-130.
Makar, J. and J. Beaudoin (2004). Carbon nanotubes and their application in the construction industry. , Nanotechnology in Construction (Proceedings of the First International Symposium on Nanotechnology and Construction), Paisley, Scotland.
Makar, J., J. Margeson and J. Luh (2005). "Carbon nanotube/cement composites-early results and potential applications."
Makar, J. M. and G. W. Chan (2009). "Growth of Cement Hydration Products on Single-Walled Carbon Nanotubes." Journal of the American Ceramic Society **92**(6): 1303-1310.
Makar, J. M. and G. W. Chan (2009). "Growth of Cement Hydration Products on Single-Walled Carbon Nanotubes." Journal of the American ceramic society **92**(6): 1303-1310.
Makar, J. M., J. C. Margeson and J. Luh (2005). Carbon nanotube/cement composites - early results and potential applications. 3rd International Conference on Construction Materials: Performance, Innovations and Structural Implications. Vancouver, B.C.: 1-10.
Manzur, T. and N. Yazdani (2010). "Strength Enhancement of Cement Mortar with Carbon Nanotubes." Transportation Research Record: Journal of the Transportation Research Board **2142**(-1): 102-108.
Marx, D. and J. Hutter "Ab initio molecular dynamics: theory and implementation."
Massey Jr, F. J. (1951). "The Kolmogorov-Smirnov test for goodness of fit." Journal of the American statistical Association **46**(253): 68-78.
Matarredona, O., H. Rhoads, Z. R. Li, J. H. Harwell, L. Balzano and D. E. Resasco (2003). "Dispersion of single-walled carbon nanotubes in aqueous solutions of the anionic surfactant NaDDBS." Journal of Physical Chemistry B **107**(48): 13357-13367.
Merlino, S., E. Bonaccorsi and T. Armbruster (1999). "Tobermorites: Their real structure and order-disorder (OD) character." American Mineralogist **84**(10): 1613-1621.
Metaxa, Z., M. Konsta-Gdoutos and S. Shah (2010). "Mechanical properties and nanostructure of cement-based materials reinforced with carbon nanofibers and polyvinyl alcohol (PVA) microfibers." ACI Special Publication **270**.
Metaxa, Z. S., M. S. Konsta-Gdoutos and S. P. Shah (2013). "Carbon nanofiber cementitious composites: Effect of debulking procedure on dispersion and reinforcing efficiency." Cement and Concrete Composites **36**(0): 25-32.
Method, R. C. o. F. M. o. C.-T. (1985). "Determination of the fracture energy of mortar and concrete by means of three-point bend tests on notched beams." Materials and Structures **18**(4): 287-290.
Mohamed, S. (2009). "Wireless and embedded carbon nanotube networks for damage detection in concrete structures." Nanotechnology **20**(39): 395502.
Moore, V. C., M. S. Strano, E. H. Haroz, R. H. Hauge, R. E. Smalley, J. Schmidt and Y. Talmon (2003). "Individually suspended single-walled carbon nanotubes in various surfactants." Nano Letters **3**(10): 1379-1382.
Moreno, M., W. Morris, M. G. Alvarez and G. S. Duffó (2004). "Corrosion of reinforcing steel in simulated concrete pore solutions: Effect of carbonation and chloride content." Corrosion Science **46**(11): 2681-2699.
Morsy, M., S. Alsayed and M. Aqel (2010). "Hybrid effect of carbon nanotube and nano-clay on physico-mechanical properties of cement mortar." Construction and Building Materials **25**(1): 145-149.

Mukhopadhyay, K., C. D. Dwivedi and G. N. Mathur (2002). "Conversion of carbon nanotubes to carbon nanofibers by sonication." Carbon **40**(8): 1373-1376.
Musso, S., J.-M. Tulliani, G. Ferro and A. Tagliaferro (2009). "Influence of carbon nanotubes structure on the mechanical behavior of cement composites." Composites Science and Technology **69**(11-12): 1985-1990.
Nanocyl (2009) "NANOCYLTM NC3100 series - Product Datasheet – Thin Multi-Wall Carbon Nanotubes."
Nasibulin, A. G., S. D. Shandakov, L. I. Nasibulina, A. Cwirzen, P. R. Mudimela, K. Habermehl-Cwirzen, D. A. Grishin, Y. V. Gavrilov, J. E. M. Malm, U. Tapper, Y. Tian, V. Penttala, M. J. Karppinen and E. I. Kauppinen (2009). "A novel cement-based hybrid material." New Journal of Physics **11**: 023013.
Nochaiya, T. and A. Chaipanich (2011). "Behavior of multi-walled carbon nanotubes on the porosity and microstructure of cement-based materials." Applied Surface Science **257**(6): 1941-1945.
O'Connell, M. J., S. M. Bachilo, C. B. Huffman, V. C. Moore, M. S. Strano, E. H. Haroz, K. L. Rialon, P. J. Boul, W. H. Noon, C. Kittrell, J. Ma, R. H. Hauge, R. B. Weisman and R. E. Smalley (2002). "Band Gap Fluorescence from Individual Single-Walled Carbon Nanotubes." Science **297**(5581): 593-596.
Odegard, G. M., T. S. Gates, K. E. Wise, C. Park and E. J. Siochi (2003). "Constitutive modeling of nanotube-reinforced polymer composites." Composites Science and Technology **63**(11): 1671-1687.
Osbaeck, B. and V. Johansen (1989). "Particle size distribution and rate of strength development of Portland cement." Journal of the American Ceramic Society **72**(2): 197-201.
Pagani, G., M. J. Green, P. Poulin and M. Pasquali (2012). "Competing mechanisms and scaling laws for carbon nanotube scission by ultrasonication." Proceedings of the National Academy of Sciences **109**(29): 11599-11604.
Paria, S. and K. C. Khilar (2004). "A review on experimental studies of surfactant adsorption at the hydrophilic solid-water interface." Advances in Colloid and Interface Science **110**(3): 75-95.
Park, H. J., M. Park, J. Y. Chang and H. Lee (2008). "The effect of pre-treatment methods on morphology and size distribution of multi-walled carbon nanotubes." Nanotechnology **19**(33): 335702.
Park, M., B. H. Kim, S. Kim, D. S. Han, G. Kim and K. R. Lee (2011). "Improved binding between copper and carbon nanotubes in a composite using oxygen-containing functional groups." Carbon **49**(3): 811-818.
Patel, N. and S. A. Egorov (2005). "Dispersing nanotubes with surfactants: A microscopic statistical mechanical analysis." Journal of the American Chemical Society **127**(41): 14124-14125.
Peigney, A., C. Laurent, E. Flahaut, R. Bacsa and A. Rousset (2001). "Specific surface area of carbon nanotubes and bundles of carbon nanotubes." Carbon **39**(4): 507-514.
Peigney, A., C. Laurent, E. Flahaut, R. R. Bacsa and A. Rousset (2001). "Specific surface area of carbon nanotubes and bundles of carbon nanotubes." Carbon **39**(4): 507-514.
Pellenq, R. J. M., N. Lequeux and H. van Damme (2008). "Engineering the bonding scheme in C-S-H: The iono-covalent framework." Cement and Concrete Research **38**(2): 159-174.
Pellenq, R. J. M. and H. Van Damme (2004). "Why does concrete set?: The nature of cohesion forces in hardened cement-based materials." Mrs Bulletin **29**(5): 319-323.
Pompeo, F. and D. E. Resasco (2002). "Water solubilization of single-walled carbon nanotubes by functionalization with glucosamine." Nano Letters **2**(4): 369-373.

Puertas, F., H. Santos, M. Palacios and S. Martínez-Ramírez (2005). Polycarboxylate superplasticiser admixtures: effect on hydration, microstructure and rheological behaviour in cement pastes, Institution of Civil Engineers (ICE).
Qian, D., E. C. Dickey, R. Andrews and T. Rantell (2000). "Load transfer and deformation mechanisms in carbon nanotube-polystyrene composites." Applied Physics Letters **76**(20): 2868-2870.
Qiao, R. and P. C. Ke (2006). "Lipid-carbon nanotube self-assembly in aqueous solution." Journal of the American Chemical Society **128**(42): 13656-13657.
Rajabipour, F., G. Sant and J. Weiss (2008). "Interactions between shrinkage reducing admixtures (SRA) and cement paste's pore solution." Cement and Concrete Research **38**(5): 606-615.
Ramachandran, V. S. (1995). Concrete admixtures handbook : properties, science, and technology. Park Ridge, N.J., U.S.A., Noyes Publications.
Richard, C., F. Balavoine, P. Schultz, T. W. Ebbesen and C. Mioskowski (2003). "Supramolecular self-assembly of lipid derivatives on carbon nanotubes." Science **300**(5620): 775-778.
Richardson, I. and G. Groves (1993). "Microstructure and microanalysis of hardened ordinary Portland cement pastes." Journal of Materials Science **28**(1): 265-277.
Rigby, D., H. Sun and B. E. Eichinger (1997). "Computer simulations of poly(ethylene oxide): Force field, PVT diagram and cyclization behaviour." Polymer International **44**(3): 311-330.
Sáez de Ibarra, Y., J. Gaitero, E. Erkizia and I. Campillo (2006). "Atomic force microscopy and nanoindentation of cement pastes with nanotube dispersions." physica status solidi (a) **203**(6): 1076-1081.
Sanahuja, J., L. Dormieux and G. Chanvillard (2007). "Modelling elasticity of a hydrating cement paste." Cement and Concrete Research **37**(10): 1427-1439.
Sanchez, F. and L. Zhang (2008). "Molecular dynamics modeling of the interface between surface functionalized graphitic structures and calcium-silicate-hydrate: Interaction energies, structure, and dynamics." Journal of Colloid and Interface Science **323**(2): 349-358.
Shah, S. (1990). "Determination of fracture parameters (K Ic s and CTOD c) of plain concrete using three-point bend tests." Materials and Structures **23**(6): 457-460.
Shah, S. P., M. S. Konsta-Gdoutos, Z. S. Metaxa and P. Mondal (2009). Nanoscale Modification of Cementitious Materials. Nanotechnology in Construction 3. Z. Bittnar, P. J. M. Bartos, J. Nemecek, V. Smilauer and J. Zeman, Springer Berlin Heidelberg: 125-130.
Shin, J. Y., T. Premkumar and K. E. Geckeler (2008). "Dispersion of single-walled carbon nanotubes by using surfactants: Are the type and concentration important?" Chemistry-a European Journal **14**(20): 6044-6048.
Shuba, M., A. Paddubskaya, P. Kuzhir, S. Maksimenko, V. Ksenevich, G. Niaura, D. Seliuta, I. Kasalynas and G. Valusis (2012). "Soft cutting of single-wall carbon nanotubes by low temperature ultrasonication in a mixture of sulfuric and nitric acids." Nanotechnology **23**(49): 495714.
Sigma-Aldrich (2014). "Safety data sheet: Sodium dodecylbenzenesulfonate, sodium dodecyl sulfate, sodium octyl-benzene sulfonate, sodium butylbenzene sulfonate and sodium cholate (hydrates) ".
Singh, I. V., M. Tanaka, J. Zhang and M. Endo (2007). "Evaluation of effective thermal conductivity of CNT-based nano-composites by element free Galerkin method." International Journal of Numerical Methods for Heat & Fluid Flow **17**(7-8): 757-769.

Somasundaran, P., D. W. Fuerstenau and T. W. Healy (1964). "SURFACTANT ADSORPTION AT SOLID-LIQUID INTERFACE-DEPENDENCE OF MECHANISM ON CHAIN LENGTH." Journal of Physical Chemistry **68**(12): 3562-&.
Song, Y. S. and J. R. Youn (2005). "Influence of dispersion states of carbon nanotubes on physical properties of epoxy nanocomposites." Carbon **43**(7): 1378-1385.
Soules, T. F. (1979). "MOLECULAR DYNAMIC CALCULATION OF THE STRUCTURE OF SODIUM-SILICATE GLASSES." Journal of Chemical Physics **71**(11): 4570-4578.
Stigter, D. (1974). "MICELLE FORMATION BY IONIC SURFACTANTS .2. SPECIFICITY OF HEAD GROUPS, MICELLE STRUCTURE." Journal of Physical Chemistry **78**(24): 2480-2485.
Stillinger, F. H. and A. Rahman (1978). "REVISED CENTRAL FORCE POTENTIALS FOR WATER." Journal of Chemical Physics **68**(2): 666-670.
Strano, M. S., V. C. Moore, M. K. Miller, M. J. Allen, E. H. Haroz, C. Kittrell, R. H. Hauge and R. Smalley (2003). "The role of surfactant adsorption during ultrasonication in the dispersion of single-walled carbon nanotubes." Journal of nanoscience and nanotechnology **3**(1-2): 1-2.
Streit, J. K., S. M. Bachilo, A. V. Naumov, C. Khripin, M. Zheng and R. B. Weisman (2012). "Measuring Single-Walled Carbon Nanotube Length Distributions from Diffusional Trajectories." Acs Nano **6**(9): 8424-8431.
Sun, J., L. Gao and W. Li (2002). "Colloidal processing of carbon nanotube/alumina composites." Chemistry of Materials **14**(12): 5169-5172.
Sun, Z., V. Nicolosi, D. Rickard, S. D. Bergin, D. Aherne and J. N. Coleman (2008). "Quantitative Evaluation of Surfactant-stabilized Single-walled Carbon Nanotubes: Dispersion Quality and Its Correlation with Zeta Potential." The Journal of Physical Chemistry C **112**(29): 10692-10699.
Tan, Y. and D. E. Resasco (2005). "Dispersion of Single-Walled Carbon Nanotubes of Narrow Diameter Distribution." The Journal of Physical Chemistry B **109**(30): 14454-14460.
Tan, Y. Q. and D. E. Resasco (2005). "Dispersion of single-walled carbon nanotubes of narrow diameter distribution." Journal of Physical Chemistry B **109**(30): 14454-14460.
Tang, W., M. H. Santare and S. G. Advani (2003). "Melt processing and mechanical property characterization of multi-walled carbon nanotube/high density polyethylene (MWNT/HDPE) composite films." Carbon **41**(14): 2779-2785.
Tang, Y. M., Y. F. Miao, Y. Zuo, G. D. Zhang and C. L. Wang (2012). "Corrosion behavior of steel in simulated concrete pore solutions treated with calcium silicate hydrates." Construction and Building Materials **30**: 252-256.
Taylor, H. F. (1997). Cement chemistry, Thomas Telford.
Tenent, R. C., T. M. Barnes, J. D. Bergeson, A. J. Ferguson, B. To, L. M. Gedvilas, M. J. Heben and J. L. Blackburn (2009). "Ultrasmooth, Large-Area, High-Uniformity, Conductive Transparent Single-Walled-Carbon-Nanotube Films for Photovoltaics Produced by Ultrasonic Spraying." Advanced materials **21**(31): 3210-3216.
Terzis, A., S. Filippakis, H. J. Kuzel and H. Burzlaff (1987). "THE CRYSTAL-STRUCTURE OF CA2AL(OH)6CL.2H2O." Zeitschrift Fur Kristallographie **181**(1-4): 29-34.
Thauvin, C., S. Rickling, P. Schultz, H. Celia, S. Meunier and C. Mioskowski (2008). "Carbon nanotubes as templates for polymerized lipid assemblies." Nature Nanotechnology **3**(12): 743-748.
Thostenson, E. T., C. Li and T.-W. Chou (2005). "Nanocomposites in context." Composites Science and Technology **65**(3-4): 491-516.

Tiwari, M. D., G. H. Sagar and J. R. Bellare (2012). "Flow Cytometry-Based Evaluation and Enrichment of Multiwalled Carbon Nanotube Dispersions." Langmuir **28**(11): 4939-4947.
Tserpes, K. I., P. Papanikos, G. Labeas and S. G. Pantelakis (2008). "Multi-scale modeling of tensile behavior of carbon nanotube-reinforced composites." Theoretical and Applied Fracture Mechanics **49**(1): 51-60.
Tummala, N. R., B. H. Morrow, D. E. Resasco and A. Striolo (2010). "Stabilization of Aqueous Carbon Nanotube Dispersions Using Surfactants: Insights from Molecular Dynamics Simulations." Acs Nano **4**(12): 7193-7204.
Tummala, N. R. and A. Striolo (2009). "Curvature effects on the adsorption of aqueous sodium-dodecyl-sulfate surfactants on carbonaceous substrates: Structural features and counterion dynamics." Physical Review E **80**(2).
Tummala, N. R. and A. Striolo (2009). "SDS Surfactants on Carbon Nanotubes: Aggregate Morphology." Acs Nano **3**(3): 595-602.
Uchikawa, H., D. Sawaki and S. Hanehara (1995). "Influence of kind and added timing of organic admixture on the composition, structure and property of fresh cement paste." Cement and Concrete Research **25**(2): 353-364.
Uddin, N. M., F. M. Capaldi and B. Farouk (2011). "Molecular dynamics simulations of the interactions and dispersion of carbon nanotubes in polyethylene oxide/water systems." Polymer **52**(2): 288-296.
Vaisman, L., H. D. Wagner and G. Marom (2006). "The role of surfactants in dispersion of carbon nanotubes." Advances in Colloid and Interface Science **128-130**: 37-46.
Vaisman, L., H. D. Wagner and G. Marom (2006). "The role of surfactants in dispersion of carbon nanotubes." Advances in Colloid and Interface Science **128**: 37-46.
Velasco-Santos, C., A. Martinez-Hernandez, F. Fisher, R. Ruoff and V. Castano (2003). "Dynamical–mechanical and thermal analysis of carbon nanotube–methyl-ethyl methacrylate nanocomposites." Journal of Physics D: Applied Physics **36**(12): 1423-1428.
Vichchulada, P., M. A. Cauble, E. A. Abdi, E. I. Obi, Q. Zhang and M. D. Lay (2010). "Sonication power for length control of single-walled carbon nanotubes in aqueous suspensions used for 2-dimensional network formation." The Journal of Physical Chemistry C **114**(29): 12490-12495.
Victor C. Li and K. H. Obla (1994). "Effect of fiber length variation on tensile properties of carbon-fiber cement composites." Composites Engineering **4**(9): 947-964.
Wallace, E. J. and M. S. P. Sansom (2007). "Carbon nanotube/detergent interactions via coarse-grained molecular dynamics." Nano Letters **7**(7): 1923-1928.
Wang, H. (2009). "Dispersing carbon nanotubes using surfactants." Current Opinion in Colloid & Interface Science **14**(5): 364-371.
Wang, J. B., B. X. Han, M. Dai, H. K. Yan, Z. X. Li and R. K. Thomas (1999). "Effects of chain length and structure of cationic surfactants on the adsorption onto Na-Kaolinite." Journal of Colloid and Interface Science **213**(2): 596-601.
Wang, L., H. Choi, J.-M. Myoung and W. Lee (2009). "Mechanical alloying of multi-walled carbon nanotubes and aluminium powders for the preparation of carbon/metal composites." Carbon **47**(15): 3427-3433.
Wang, Q., W. H. Duan, K. M. Liew and X. Q. He (2007). "Inelastic buckling of carbon nanotubes." Applied Physics Letters **90**(3): 033110.

Wang, X., J. Ye, Y. Wang and L. Chen (2007). "Reinforcement of Calcium Phosphate Cement by Bio-Mineralized Carbon Nanotube." Journal of the American Ceramic Society **90**(3): 962-964.
Wansom, S., N. Kidner, L. Woo and T. Mason (2006). "AC-impedance response of multi-walled carbon nanotube/cement composites." Cement and Concrete Composites **28**(6): 509-519.
White, A. A., S. M. Best and I. A. Kinloch (2007). "Hydroxyapatite–carbon nanotube composites for biomedical applications: a review." International Journal of Applied Ceramic Technology **4**(1): 1-13.
White, B., S. Banerjee, S. O'Brien, N. J. Turro and I. P. Herman (2007). "Zeta-potential measurements of surfactant-wrapped individual single-walled carbon nanotubes." The Journal of Physical Chemistry C **111**(37): 13684-13690.
Wille, K. and K. Loh (2010). "Nanoengineering Ultra-High-Performance Concrete with Multiwalled Carbon Nanotubes." Transportation Research Record: Journal of the Transportation Research Board **2142**(-1): 119-126.
Winnefeld, F., S. Becker, J. Pakusch and T. Götz (2007). "Effects of the molecular architecture of comb-shaped superplasticizers on their performance in cementitious systems." Cement and Concrete Composites **29**(4): 251-262.
Wu, S. H. and P. Pendleton (2001). "Adsorption of anionic surfactant by activated carbon: Effect of surface chemistry, ionic strength, and hydrophobicity." Journal of Colloid and Interface Science **243**(2): 306-315.
Wu, Y., J. S. Hudson, Q. Lu, J. M. Moore, A. S. Mount, A. M. Rao, E. Alexov and P. C. Ke (2006). "Coating single-walled carbon nanotubes with phospholipids." Journal of Physical Chemistry B **110**(6): 2475-2478.
Xu, Z. G., P. F. Li, W. H. Qiao, Z. S. Li and L. B. Cheng (2006). "Effect of aromatic ring in the alkyl chain on surface properties of arylalkyl surfactant solutions." Journal of Surfactants and Detergents **9**(3): 245-248.
Xu, Z. J., X. N. Yang and Z. Yang (2010). "A Molecular Simulation Probing of Structure and Interaction for Supramolecular Sodium Dodecyl Sulfate/Single-Wall Carbon Nanotube Assemblies." Nano Letters **10**(3): 985-991.
Xun, Y. and K. Eil (2009). "A carbon nanotube/cement composite with piezoresistive properties." Smart Materials and Structures **18**(5): 055010.
Yamada, K., T. Takahashi, S. Hanehara and M. Matsuhisa (2000). "Effects of the chemical structure on the properties of polycarboxylate-type superplasticizer." Cement and Concrete Research **30**(2): 197-207.
Yang, K., M. Gu, Y. Guo, X. Pan and G. Mu (2009). "Effects of carbon nanotube functionalization on the mechanical and thermal properties of epoxy composites." Carbon **47**(7): 1723-1737.
Yazdanbakhsh, A., Z. Grasley, B. Tyson and R. A. Al-Rub (2009). "Carbon nano filaments in cementitious materials: some issues on dispersion and interfacial bond." ACI Special Publication **267**.
Ye, G. (2003). Experimental study and numerical simulation of the development of the microstructure and permeability of cementitious materials, TU Delft, Delft University of Technology.
Ye, G., P. Lura and v. K. van Breugel (2006). "Modelling of water permeability in cementitious materials." Materials and Structures **39**(9): 877-885.
Yu, J., N. Grossiord, C. E. Koning and J. Loos (2007). "Controlling the dispersion of multi-wall carbon nanotubes in aqueous surfactant solution." Carbon **45**(3): 618-623.
Yu, J. R., N. Grossiord, C. E. Koning and J. Loos (2007). "Controlling the dispersion of multi-wall carbon nanotubes in aqueous surfactant solution." Carbon **45**(3): 618-623.

Yu, M.-F., B. S. Files, S. Arepalli and R. S. Ruoff (2000). "Tensile loading of ropes of single wall carbon nanotubes and their mechanical properties." Physical review letters **84**(24): 5552–5555.
Yu, M.-F., O. Lourie, M. J. Dyer, K. Moloni, T. F. Kelly and R. S. Ruoff (2000). "Strength and breaking mechanism of multiwalled carbon nanotubes under tensile load." Science **287**(5453): 637-640.
Yurekli, K., C. A. Mitchell and R. Krishnamoorti (2004). "Small-Angle Neutron Scattering from Surfactant-Assisted Aqueous Dispersions of Carbon Nanotubes." Journal of the American Chemical Society **126**(32): 9902-9903.
Zhang, J. and C. He (2008). "A three-phase cylindrical shear-lag model for carbon nanotube composites." Acta Mechanica **196**(1-2): 33-54.
Zhang, J. M. and M. Tanaka (2007). "Systematic study of thermal properties of CNT composites by the fast multipole hybrid boundary node method." Engineering Analysis with Boundary Elements **31**(5): 388-401.
Zhang, M., L. Su and L. Mao (2006). "Surfactant functionalization of carbon nanotubes (CNTs) for layer-by-layer assembling of CNT multi-layer films and fabrication of gold nanoparticle/CNT nanohybrid." Carbon **44**(2): 276-283.
Zou, B., S. J. Chen, A. H. Korayem, F. Collins, C. Wang and W. H. Duan (2015). "Effect of ultrasonication energy on engineering properties of carbon nanotube reinforced cement pastes." Carbon.
Zou, B., S. J. Chen, A. H. Korayem, F. Collins, C. Wang and W. H. Duan (2015). "Effect of ultrasonication energy on engineering properties of carbon nanotube reinforced cement pastes." Carbon **85**: 212-220.